2010

Efficient methods for solving boundary integral equation in diffusive scalar problem and eddy current nondestructive evaluation

Ming Yang
Iowa State University

Efficient methods for solving boundary integral equation in diffusive scalar problem and eddy current nondestructive evaluation

by

Ming Yang

A dissertation submitted to the graduate faculty

in partial fulfillment of the requirements for the degree of

DOCTOR OF PHILOSOPHY

Major: Electrical Engineering

Program of Study Committee:
Jiming Song, Major Professor
Norio Nakagawa
William Q. Meeker
John R. Bowler
Mani Mina
Ronald A. Roberts

Iowa State University

Ames, Iowa

2010

To my parents and my wife

TABLE OF CONTENTS

LIST OF FIGURES

LIST OF TABLES

ABSTRACT

Eddy current nondestructive evaluation (NDE) of airframe structures involves the detection of electromagnetic field irregularities due to non-conducting inhomogeneities in an electrically conducting material. Usually, the eddy current NDE problem can be formulated by the boundary integral equations (BIE) and discretized into matrix equations by the method of moments (MoM) or the boundary element method (BEM). The fast multipole method (FMM) is a well-established and effective method for accelerating numerical solutions of the matrix equations. Accelerated by the FMM, the BIE method can now solve large-scale electromagnetic wave propagation and diffusion problems. The traditional BIE method requires O(N^2) operations to compute the system of equations and another O(N^3) operations to solve the system using direct solvers, with N being the number of unknowns; in contrast, the BIE method accelerated by the two-level FMM can potentially reduce the operations and memory requirement to O($N^{3/2}$). Moreover, several approaches have been proposed for the field calculation in the presence of flaws in three dimensional NDE; however, seldom work has been done in applying efficient methods to seek rapid solution in eddy current NDE simulation.

As elaborated in the dissertation, we introduce a fast multipole BIE method for two-dimensional diffusive scalar problem and an efficient BIE method for three-dimensional eddy current NDE. Firstly, we work with the two-dimensional Helmholtz equation with a complex wave number for non-trivial boundary geometry. We describe the FMM acceleration procedure of the BIE method and its features briefly, explaining that the FMM is not only efficient in meshing complicated geometries, accurate for solving singular fields or

fields in finite domains, but also practical and often superior to other methods in solving large-scale problems. Subsequently, computational tests of the numerical FMM solutions against the conventional BIE results and their complexity are presented. Secondly, for the eddy current NDE, a BIE method in three dimensions has been demonstrated. The eddy current problem is formulated by the BIE and discretized into matrix equations by the method of moments (MoM) or the boundary element method (BEM). In our implementation of the Stratton-Chu formulation for the conductive medium, the equivalent electric and magnetic surface currents are expanded in terms of Rao-Wilton-Glisson (RWG) vector basis function while the normal component of magnetic field is expanded in terms of the pulse basis function. Also, a low frequency approximation is applied in the external medium, that is, free space in our case. Computational tests are presented to demonstrate the accuracy and capability of the three-dimensional BIE method with a complex wave number for arbitrarily shaped objects described by a number of triangular patches. The results of this research set the stage for the efficient BIE method to be applied in more practical eddy current NDE simulation and be embedded with the FMM in the future.

CHAPTER 1. INTRODUCTION

Eddy current nondestructive evaluation (NDE) involves the detection of electromagnetic field irregularities due to non-conducting inhomogeneities in an electrically conducting material [1], which often needs to treat with complicated geometrical features. Typically, the primary eddy current field is produced by sinusoidal excitation of a small induction coil near the surface of the component to be inspected. When scanning the coil over the surface, the flaw detection is achieved by searching for coil impedance changes that imply flaw-induced perturbation of the eddy current density [2], as shown in Figure 1.1. Accordingly, computer simulation of the flaw detection process includes calculation of the electromagnetic field distribution around the flaw and the response of the detection system to this perturbed distribution. There exists a reciprocity theorem originally proposed by Rumsey [3], which allows us to express the flaw response function for the exciter coil-sensor system. Through this theorem, the complicated problem of calculating the receiver response is reduced to the calculation of fields produced by an induction coil in an unflawed material and evaluation of the flaw response surface integral. Fortunately, for a half-space and certain simple geometries, these fields can be calculated by means of existing analytical expressions [4, 5]. Also, several approaches have been proposed for the field calculation in the presence of flaws, which include the simple point flaw model [6], finite element model [7] and boundary element model [8, 9]; however, seldom work has been done in applying efficient methods to seek rapid solution in eddy current NDE simulation, although applications of fast algorithms have become a hot topic in computational electromagnetic society for more than twenty years.

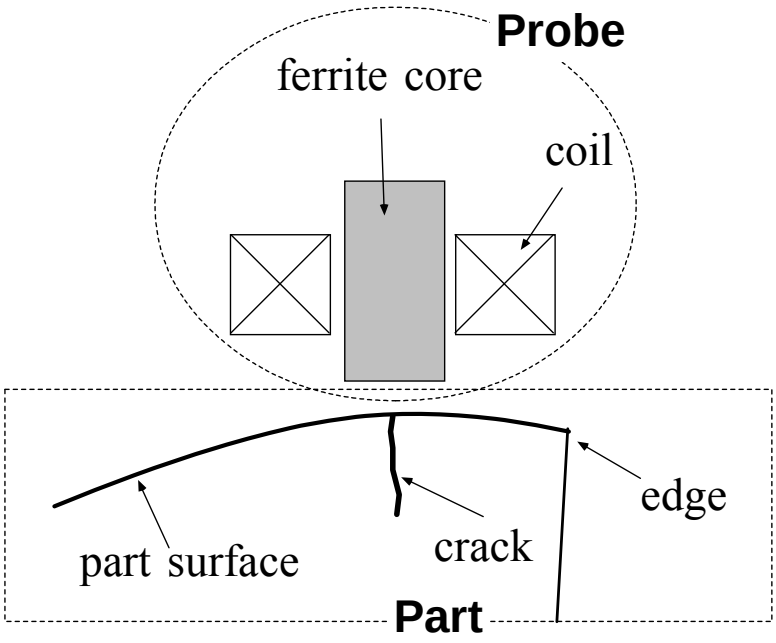

Figure 1.1. A diagram of conceptual eddy current inspection system.

The boundary integral equations (BIE) method is a numerical computational method of solving linear partial differential equations which have been formulated as integral equations. It can be applied in many areas of engineering and science including fluid mechanics, acoustics, electromagnetics, and fracture mechanics. In electromagnetics, the more traditional term "method of moments" is often, though not always, synonymous with BIE method. The fast multipole method (FMM) [10-13] was originally proposed by Rokhlin and Greengard to evaluate particle simulations and to solve static integral equation rapidly. In 1990s, the FMM was extended by Rokhlin to solve acoustic wave scattering problems [14] and then to solve electromagnetic scattering problems by many researchers in both two dimensions [15-19] and three dimensions [20, 21]. Till now, the FMM has been developed into a well-established and effective scheme for accelerating numerical solutions of boundary integral equations, due to

which we propose to extend the FMM into eddy current NDE field. The conventional BIE method generates a dense asymmetric matrix; therefore, it requires $O(N^2)$ operations to compute the system of equations and another $O(N^3)$ operations to solve the system using direct solvers, with N being the number of unknowns. In contrast, the BIE method accelerated by the two-level FMM can potentially reduce the operations and memory requirement to $O(N^{3/2})$ [22]. With a multilevel fast multipole algorithm, it is further reduced to $O(N\log N)$ [23, 24]. Accelerated by the FMM, the BIE method can now solve large-scale electromagnetic wave propagation and diffusion problems with up to a million unknowns on a personal computer [25, 26]. Certain eddy-current modeling problems such as NDE of airframe structures may involve complicated geometrical features including cracks, fasteners, sharp corners/edges, multi-layered structures, complex ferrite-cored probes, etc. The FMM accelerated BIE method has a significant potential to solve such large-scale problems efficiently.

In this dissertation, we introduce a fast multipole BIE method for two-dimensional diffusive scalar problem and an efficient BIE method for three-dimensional eddy current NDE. Firstly, we work with the two-dimensional Helmholtz equation with a complex wave number for non-trivial boundary geometry. We describe the FMM acceleration procedure of the BIE method and its features briefly, explaining that the FMM is not only efficient in meshing complicated geometries, accurate for solving singular fields or fields in finite domains, but also practical and often superior to other methods in solving large-scale problems. Subsequently, computational tests of the numerical FMM solutions against the conventional BIE results and their complexity are presented. Secondly, for the eddy current NDE, a BIE method in three dimensions has been demonstrated. The eddy current problem is formulated by the BIE and discretized into matrix equations by the method of moments (MoM) [27] or the boundary

element method (BEM). In our implementation of the Stratton-Chu formulation [28] for the conductive medium, the equivalent electric and magnetic surface currents are expanded in terms of Rao-Wilton-Glisson (RWG) vector basis function [29] while the normal component of magnetic field is expanded in terms of the pulse basis function. Also, a low frequency approximation is applied in the external medium, that is, free space in our case. Computational tests are presented to demonstrate the accuracy and capability of the three-dimensional BIE method with a complex wave number for arbitrarily shaped objects described by a number of triangular patches. The results of this research set the stage for the efficient BIE method to be applied in more practical eddy current NDE simulation and be embedded with the FMM in the future.

As for this dissertation, in Chapter 2, integral equations and the method of moments are briefly introduced. This chapter also includes Rao-Wilson-Glisson (RWG) basis function and its projection error analysis. In Chapter 3, the procedure of the FMM accelerated BIE method in two dimensions is demonstrated in detail. This method is not only efficient in meshing complicated geometries, accurate for solving singular fields or fields in finite domains, but also practical and often superior to other methods in solving large-scale problems. Computational tests of the numerical FMM solutions against the conventional BIE results are presented for the two-dimensional Helmholtz equation with a complex wave number. In Chapter 4, the implementation of Stratton-Chu formulation in three dimensions for the conductive medium is introduced, in which the induced electric and magnetic surface currents are expanded in terms of the RWG vector basis function and the normal component of magnetic field is expanded in terms of pulse basis function. In Chapter 5, computational tests are presented to demonstrate the accuracy and capability of the BIE method with a complex wave number for

three-dimensional objects described by a number of triangular patches. The agreement between numerical results and those from theory and/or experiment is reasonably good in both cases of near field distribution and impedance variation, which also give us confidence that our numerical codes can successfully simulate eddy current NDE for arbitrary shape conductive objects interacted with coils in NDE application.

CHAPTER 2. INTEGRAL EQUATION AND THE METHOD OF MOMENTS

The method of moments (MoM), widely used in computational electromagnetics due to the pioneer work of Roger Harrington in 1968 [27], was originally popular for structural analysis in many areas of engineering and science and has since become common in computational electromagnetic analysis. The MoM is a numerical computational method of solving linear partial differential equations which have been formulated as integral equations (i.e. in boundary integral form). In the computation process, the MoM reduces an integral equation into a system of linear equations, which are solved to determine parameters of interest. After the integral equation has been derived, there are four steps in the implementation of the MoM, which are as follows: 1) expansion of the unknown function using basis or expansion functions, 2) evaluation of the integral equation using weighting or testing functions, 3) evaluation of the moment matrix elements, 4) and solving the matrix equation and obtaining the parameters of interest. The integral equation and each of the necessary steps is now discussed in detail.

2.1 Integral Equation

Usually, the most difficult aspect of implementing the MoM is to derive the associated integral equation. The integral equation is given as

$$Lu(x) = \int_a^b K(x,x')u(x')dx' = f(x) \tag{2.1}$$

where L is an operator, f is the known excitation, u is the response, and K is called the kernel. In general, the operator L may be differential, integral, or integro-differential. Most integral

equations do not have a closed form solution. However, they can often be discretized and solved on a digital computer. Proof of the existence of the solution to an integral equation by discretization was first presented by Fredholm [30] in 1903. The purpose of the numerical solution is to determine numerical approximation of the unknown function, u. For the formulations presented here, the operator is a surface or volume integral. If the limits on the integration domain are fixed, such as in equation (2.1) then the integral equation is said to be a Fredholm Equation. Generally, there are three different kinds of Fredholm equations:

Fredholm first kind

$$Lu(x) = f(x) \tag{2.2}$$

Fredholm second kind

$$Lu(x) + u(x) = f(x) \tag{2.3}$$

Fredholm third kind

$$Lu(x) + a(x)u(x) = f(x) \tag{2.4}$$

As is done in the MoM, Fredholm equations are often solved by replacing the integral equation with a linear system and solving the system. The accuracy of numerically evaluating the integral depends on the numerical method employed and the number of quadrature points used. For electromagnetic applications, we can have both scalar and vector integral equations.

2.2 Method of Moments

The integral equation may be regarded as an exact solution of the governing partial differential equation. The MoM attempts to use the given boundary conditions to fit boundary values into the integral equation, rather than values throughout the space defined by a

partial differential equation. Once this is done, in the post-processing stage, the integral equation can then be used again to calculate numerically the solution directly at any desired point in the interior of the solution domain.

To be specific, when the MoM is applied to the integral equation (2.1), the first step is to expand the unknown function $u(x)$, using basis (or expansion) functions $b_n(x)$

$$u(x) \approx \sum_{n=1}^{N} u_n b_n(x) \tag{2.5}$$

where u_n are unknown coefficients to be solved. The integral equation is now expressed as a summation of integral equations for basis functions

$$Lu(x) \approx \sum_{n=1}^{N} u_n Lb_n(x) = f(x) \tag{2.6}$$

The second step is to discretize the integral equation using weighting or testing functions $t_m(x)$.

$$\int dx t_m(x) Lu(x) = \int dx t_m(x) \sum_{n=1}^{N} u_n Lb_n(x) = \int dx t_m(x) f(x) \quad m = 1, 2, \ldots, N \tag{2.7}$$

The result is a matrix equation, which can be expressed as

$$Au = f \quad u = [u_1, u_2, \ldots, u_N]^T \quad f = [f_1, f_2, \ldots, f_N]^T \tag{2.8}$$

Once the problem has been transformed to a matrix equation, the third step in implementing the method of moments is to evaluate the moment matrix elements.

$$f_m = \int dx t_m(x) f(x) \tag{2.9}$$

$$A_{mn} = \int dx t_m(x) Lb_n(x) \tag{2.10}$$

The fourth and final step in the MoM is to solve the matrix equation for the unknown function and determine the remaining parameters of interest. The matrix equation is solved using Gaussian elimination, the lower-upper decomposition (LUD), or an iterative solver such as conjugate gradient (CG) method, the bi-conjugate gradient (BICG) method, or generalized minimal residual method (GMRES).

The Galerkin's method sets the testing functions the same as the basis functions. Resulting in

$$f_m = \int dx b_m(x) f(x) \tag{2.11}$$

$$A_{mn} = \int dx b_m(x) L b_n(x) \tag{2.12}$$

The method of moments is often more efficient than other methods, including finite elements, in terms of computational resources for problems where there is a small surface-to-volume ratio. Conceptually, it works by constructing a "mesh" over the modeled surface. However, for many problems MoM is significantly less efficient than volume-discretisation methods (finite element method, finite difference method, finite volume method). MoM formulations typically give rise to fully populated matrices. This means that the storage requirements and computational time will tend to grow according to the square of the problem size. By contrast, finite element matrices are typically banded (elements are only locally connected) and the storage requirements for the system matrices typically grow quite linearly with the problem size. Compression techniques (e.g. multi-pole expansions or adaptive cross approximation/hierarchical matrices) can be used to ameliorate these problems,

though at the cost of added complexity and with a success-rate that depends heavily on the nature of the problem being solved and the geometry involved.

2.3 Surface Integral Equation for Scattering from Homogeneous Objects

Much attention has been given to the development of integral formulations to solve interactions of electromagnetic waves with homogeneous bodies [31-37]. Harrington [32] introduced a general formulation allowing for combination constants. Of the various formulations this allows, the Müller [31] and PMCHWT [36] formulations are most commonly used. The Müller formulation has been recognized for its use in evaluating scattering from low contrast media. The PMCHWT formulation was first referred to as such by Mautz and Harrington in [36] from the initials of Poggio and Müller [33], Chang and Harrington [34], and Wu and Tsai [35]. These two formulations have been compared by Harrington. However, a complete comparison has yet to be presented for other combinations. In this section, the surface integral equation is given and two new formulations are presented and compared to the well-known Müller and PMCHWT formulations [38]. The integral formulations can be discretized to matrix equations using the method of moments.

Given a homogeneous dielectric object, which is bounded by S, using either the equivalence principle or the vector Green's theorem, one can formulate a set of four integral equations to calculate the electric and magnetic fields **E** and **H** in terms of equivalent electric and magnetic currents **J** and **M** on the surface of the object [32, 37], as shown in Figure 2.1, where one is for the material outside the object (medium 1) and the other is for the material inside the object (medium 2) [32].

$$\begin{aligned} \hat{n}\times\mathbf{E}_1^-(\mathbf{J},\mathbf{M}) &= -\hat{n}\times\mathbf{E}^{inc} \quad \hat{n}\times\mathbf{E}_2^+(\mathbf{J},\mathbf{M}) = 0 \\ \hat{n}\times\mathbf{H}_1^-(\mathbf{J},\mathbf{M}) &= -\hat{n}\times\mathbf{H}^{inc} \quad \hat{n}\times\mathbf{H}_2^+(\mathbf{J},\mathbf{M}) = 0 \end{aligned} \tag{2.13}$$

where $(\mathbf{E}^{inc},\mathbf{H}^{inc})$ denote the incident fields when medium 2 is the same as medium 1, the subscript 1 or 2 refers to medium 1 or medium 2, and the superscripts + and - denote the tangential components evaluated on S_+ or S_-, respectively.

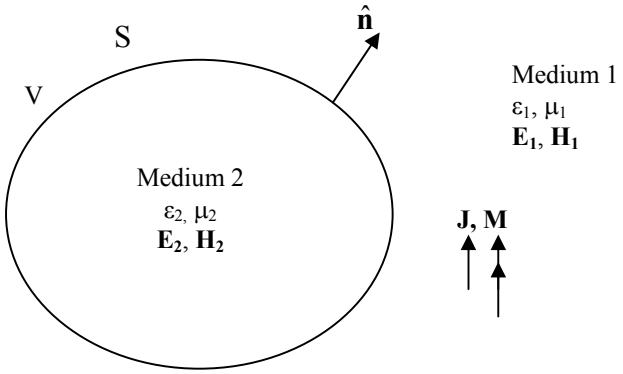

Figure 2.1. A scattering body in the presence of an impressed field produced by equivalent electric and magnetic currents **J** and **M.**

The electromagnetic fields are related to the equivalent currents by

$$\begin{aligned} \mathbf{E}_j^{\pm}(\mathbf{J},\mathbf{M}) &= \eta_j\mathbf{L}_j(\mathbf{J}) + \mathbf{K}_j(\mathbf{M}) \pm \frac{1}{2}\hat{n}\times\mathbf{M} \\ \mathbf{H}_j^{\pm}(\mathbf{J},\mathbf{M}) &= \frac{1}{\eta_j}\mathbf{L}_j(\mathbf{M}) - \mathbf{K}_j(\mathbf{J}) \mp \frac{1}{2}\hat{n}\times\mathbf{J} \end{aligned} \tag{2.14}$$

where $\eta_j = \sqrt{\mu_j/\varepsilon_j}$ and $j = 1,2$. These two equations also can be confirmed using the duality,

$$\mathbf{J}\to\mathbf{M}, \quad \mathbf{M}\to-\mathbf{J}, \quad \eta\to 1/\eta, \quad \mathbf{E}\to\mathbf{H}, \quad \mathbf{H}\to-\mathbf{E}$$

The two operators **L** and **K** are defined as [37, 38]

$$\mathbf{L}_j(\mathbf{X}) = ik_j\int_S\left[\mathbf{X}(\mathbf{r}') + \frac{1}{k_j^2}\nabla\nabla'\cdot\mathbf{X}(\mathbf{r}')\right]G_j(\mathbf{r},\mathbf{r}')dS' \tag{2.15}$$

$$\mathbf{K}_j(\mathbf{X}) = P.V.\int_S \mathbf{X}(\mathbf{r}')\times\nabla G_j(\mathbf{r},\mathbf{r}')dS' \tag{2.16}$$

where $k_i = \omega\sqrt{\varepsilon_i\mu_i}$, $j = 1,2$, and $P.V.$ stands for the Cauchy principal value of the finite integral. Also, the Green's function is given as

$$G(\mathbf{r},\mathbf{r}') = \frac{e^{-jk|\mathbf{r}-\mathbf{r}'|}}{4\pi\,|\,\mathbf{r}-\mathbf{r}'\,|} \tag{2.17}$$

Substituting (2.14) to (2.16) into (2.13) yields

$$\begin{aligned}
-\eta_1\mathbf{L}_1^{\times}(\mathbf{J}) - \mathbf{K}_1^{\times}(\mathbf{M}) - \frac{1}{2}\mathbf{M} &= \mathbf{E}^{inc\times} \\
-\eta_2\mathbf{L}_2^{\times}(\mathbf{J}) - \mathbf{K}_2^{\times}(\mathbf{M}) + \frac{1}{2}\mathbf{M} &= 0 \\
\mathbf{K}_1^{\times}(\mathbf{J}) - \frac{1}{\eta_1}\mathbf{L}_1^{\times}(\mathbf{M}) + \frac{1}{2}\mathbf{J} &= \mathbf{H}^{inc\times} \\
\mathbf{K}_2^{\times}(\mathbf{J}) - \frac{1}{\eta_2}\mathbf{L}_2^{\times}(\mathbf{M}) - \frac{1}{2}\mathbf{J} &= 0
\end{aligned} \tag{2.18}$$

where $\mathbf{L}_j^{\times} = \hat{n}\times\mathbf{L}_j$, $\mathbf{K}_j^{\times} = \hat{n}\times\mathbf{K}_j$, $j = 1,2$ and $\mathbf{E}^{inc\times} = \hat{n}\times\mathbf{E}^{inc}$, $\mathbf{H}^{inc\times} = \hat{n}\times\mathbf{H}^{inc}$.

We have four equations in (2.18) with two unknowns **J** and **M**. Certain pairs of these equations can be used to compute **J** and **M**. For example, first two equations are electric field integral equations (EFIE) formulations and last two are magnetic field integral equations (MFIE) formulations. It is well known that both EFIE and MFIE have internal resonance problem. In the other words, both formulations fail at frequencies for which *S*, when covered by a perfect electric conductor and filled with the exterior medium (medium 1), forms a resonant cavity. One solution for the internal resonance problem is to use combine field integral equation (CFIE):

$$\begin{aligned}
&\alpha\hat{n}\times\mathrm{EFIE} + (1-\alpha)\eta_j\mathrm{MFIE} \\
\text{or}\quad &\alpha\mathrm{EFIE} + (1-\alpha)\eta_j\hat{n}\times\mathrm{MFIE}
\end{aligned}$$

CFIE has advantages that one equation is for medium 1 and the other is for medium 2, but it has non-symmetric form for electric and magnetic currents.

There is another way to overcome the well known failure of the EFIE and MFIE. Let us look at the linear combinations of two electric field integral equations and two magnetic field equations.

$$-\eta_1 \mathbf{L}_1^{\times}(\mathbf{J}) - \alpha\eta_2 \mathbf{L}_2^{\times}(\mathbf{J}) - \mathbf{K}_1^{\times}(\mathbf{M}) - \alpha \mathbf{K}_2^{\times}(\mathbf{M}) - \frac{1}{2}(1-\alpha)\mathbf{M} = \mathbf{E}^{inc\times} \tag{2.19}$$

$$\mathbf{K}_1^{\times}(\mathbf{J}) + \beta \mathbf{K}_2^{\times}(\mathbf{J}) - \frac{1}{\eta_1}\mathbf{L}_1^{\times}(\mathbf{M}) - \frac{\beta}{\eta_2}\mathbf{L}_2^{\times}(\mathbf{M}) + \frac{1}{2}(1-\beta)\mathbf{J} = \mathbf{H}^{inc\times} \tag{2.20}$$

where α and β are combination constants. The combined formulation is the first kind of Fredholm integral equation in the form. Furthermore, it has been proved in [36] that any choice α and β for which $\alpha\beta^*$ is real and positive gives a unique solution at all frequencies to the formulation.

After Poggio, Miller, Chang, Harrington, Wu, and Tsai, the combination $\alpha = 1,\ \beta = 1$ gives the PMCHWT formulation, which also can be derived from matching the boundary conditions alternatively:

$$-\eta_1 \mathbf{L}_1^{\times}(\mathbf{J}) - \eta_2 \mathbf{L}_2^{\times}(\mathbf{J}) - \mathbf{K}_1^{\times}(\mathbf{M}) - \mathbf{K}_2^{\times}(\mathbf{M}) = \mathbf{E}^{inc\times} \tag{2.21}$$

$$\mathbf{K}_1^{\times}(\mathbf{J}) + \mathbf{K}_2^{\times}(\mathbf{J}) - \frac{1}{\eta_1}\mathbf{L}_1^{\times}(\mathbf{M}) - \frac{1}{\eta_2}\mathbf{L}_2^{\times}(\mathbf{M}) = \mathbf{H}^{inc\times} \tag{2.22}$$

The PMCHWT formulation is the first kind of Fredholm integral equation. In fact, the equations are evaluated tangential components directly:

$$\hat{t}\bullet\left[-\eta_1 \mathbf{L}_1(\mathbf{J}) - \eta_2 \mathbf{L}_2(\mathbf{J}) - \mathbf{K}_1(\mathbf{M}) - \mathbf{K}_2(\mathbf{M})\right] = \hat{t}\bullet\mathbf{E}^{inc} \tag{2.23}$$

$$\hat{t}\bullet\left[\mathbf{K}_1(\mathbf{J})+\mathbf{K}_2(\mathbf{J})-\frac{1}{\eta_1}\mathbf{L}_1(\mathbf{M})-\frac{1}{\eta_2}\mathbf{L}_2(\mathbf{M})\right]=\hat{t}\bullet\mathbf{H}^{inc} \tag{2.24}$$

Before discussing other formulations, let us rewrite the operator **L** and focus on its low frequency properties as follows,

$$\mathbf{L}_j(\mathbf{X})=ik_j\mathbf{L}_j^s(\mathbf{X})+\frac{i}{k_j}\mathbf{L}_j^c(\mathbf{X}) \tag{2.25}$$

where

$$\begin{aligned}\mathbf{L}_j^s(\mathbf{X})&=\int_S G_j(\mathbf{r},\mathbf{r}')\mathbf{X}(\mathbf{r}')dS'\\ \mathbf{L}_j^c(\mathbf{X})&=\int_S \nabla G_j(\mathbf{r},\mathbf{r}')\nabla'\cdot\mathbf{X}(\mathbf{r}')dS'\end{aligned}\qquad j=1,2 \tag{2.26}$$

The first term of $\mathbf{L}_j^s(\mathbf{X})$ is the contribution from the current directly through the scalar Green's function and the second term of $\mathbf{L}_j^c(\mathbf{X})$ is the field generated by the charge. Then the combined equations (2.19) and (2.20) become

$$\begin{aligned}&-i\omega\left[\mu_1\mathbf{L}_1^{s\times}(\mathbf{J})+\alpha\mu_2\mathbf{L}_2^{s\times}(\mathbf{J})\right]-\frac{i}{\omega\varepsilon_1}\left[\mathbf{L}_1^{c\times}(\mathbf{J})+\alpha\frac{\varepsilon_1}{\varepsilon_2}\mathbf{L}_2^{c\times}(\mathbf{J})\right]\\ &-\mathbf{K}_1^{\times}(\mathbf{M})-\alpha\mathbf{K}_2^{\times}(\mathbf{M})-\frac{1}{2}(1-\alpha)\mathbf{M}=\mathbf{E}^{inc\times}\end{aligned} \tag{2.27}$$

$$\begin{aligned}&\mathbf{K}_1^{\times}(\mathbf{J})+\beta\mathbf{K}_2^{\times}(\mathbf{J})-i\omega\left[\varepsilon_1\mathbf{L}_1^{s\times}(\mathbf{M})+\beta\varepsilon_2\mathbf{L}_2^{s\times}(\mathbf{M})\right]\\ &-\frac{i}{\omega\varepsilon_1}\left[\mathbf{L}_1^{c\times}(\mathbf{M})+\beta\frac{\mu_1}{\mu_2}\mathbf{L}_2^{c\times}(\mathbf{M})\right]+\frac{1}{2}(1-\beta)\mathbf{J}=\mathbf{H}^{inc\times}\end{aligned} \tag{2.28}$$

If $\alpha=-\varepsilon_2/\varepsilon_1$, $\beta=-\mu_2/\mu_1$, then the Müller formulation is obtained. In this formulation, the static electric field due to the electric charge and the static magnetic field due to the magnetic charge are zero. So the kernels of Müller formulation is less singular than the PMCHWT formulation.

The first alternative formulation investigated lets $\alpha = -\mu_1/\mu_2$, $\beta = -\varepsilon_1/\varepsilon_2$, which also makes the kernels of the electric filed due to the electric current and the magnetic field due to the magnetic current less singular than the Müller formulation.

The coefficients used in the second alternative formulation presented $\alpha = -1$, $\beta = -1$.

$$-\eta_1 \mathbf{L}_1^{\times}(\mathbf{J}) + \eta_2 \mathbf{L}_2^{\times}(\mathbf{J}) - \mathbf{K}_1^{\times}(\mathbf{M}) + \mathbf{K}_2^{\times}(\mathbf{M}) - \mathbf{M} = \mathbf{E}^{inc\times} \tag{2.29}$$

$$\mathbf{K}_1^{\times}(\mathbf{J}) + \mathbf{K}_2^{\times}(\mathbf{J}) - \frac{1}{\eta_1}\mathbf{L}_1^{\times}(\mathbf{M}) + \frac{1}{\eta_2}\mathbf{L}_2^{\times}(\mathbf{M}) + \mathbf{J} = \mathbf{H}^{inc\times} \tag{2.30}$$

It makes the kernels of the electric field due to the magnetic current and the magnetic field due to the electric current less singular than the Müller formulation. Furthermore, it also makes the kernels of the scalar parts of the electric field due to the electric current and the static magnetic field due to the magnetic charge less singular if either the background or the scattering body is not magnetic material. In addition, this formulation is attractive because it is of simple form and is easily rewritten as the Neumann series for low contrast homogeneous bodies.

However, the surface integral formulations presented in this section, such as PMCHWT and Müller formulations, have limitations in computation at very low frequency or quasi-static regime, which is called low-frequency breakdown [23]. With the operating frequency decreasing, the condition number of MoM matrix will increase as $1/k^2$ and reach an extremely huge number for quasi-static cases. The low-frequency breakdown problem can be described in terms of the natural Helmholtz decomposition of Maxwell's equations. As the frequency decreases, the electric and magnetic fields are decoupled. The unknown current consists of two components, a curl-free part and a divergence-free part. As for computational EM society, researchers adopted loop-tree and loop-star basis functions to expand the

divergence-free mode and curl-free mode separately [23]. In our research, as elaborated in Chapter 4, we introduce the Stratton-Chu formulation that treats the divergence-free and curl-free terms in different ways and can operate well at static and quasi-static regime.

2.4 Rao-Wilton-Glisson Basis Function

Introduced in 1982 the RWG basis function [29] has proven useful in computational electromagnetics. Its structure is similar to a roof-top basis function and its value comes from the fact that it eliminates line charges at the basis elements, allowing for a smooth and continuous current density across the edge.

To implement the RWG basis function, the surface is divided into triangular patches. The basis function is defined by the interior (non-boundary) edges of the triangular patches. The plus and minus designation of the triangles is determined by the choice of a current reference direction for the *n*th edge. The positive current direction is from the plus triangle, across the basis element (edge) into the negative triangle. The current follows from one node to the node not on the same triangle, and the current has tangential components on non-shared edges. The basis function is defined as:

$$\mathbf{b}_n(\mathbf{r}) = \begin{cases} \dfrac{l_n}{2A_n^+}\boldsymbol{\rho}_n^+ & \mathbf{r} \in T_n^+ \\ \dfrac{l_n}{2A_n^-}\boldsymbol{\rho}_n^- & \mathbf{r} \in T_n^- \\ 0 & \text{otherwise} \end{cases} \tag{2.31}$$

where $\boldsymbol{\rho}_n^+ = \mathbf{r} - \mathbf{r}_n^+$, $\boldsymbol{\rho}_n^- = \mathbf{r}_n^- - \mathbf{r}$. Meanwhile, it is easily to show that

$$\nabla \bullet \boldsymbol{\rho} = \frac{1}{\rho}\frac{\partial}{\partial \rho}\rho^2 = 2$$

$$\nabla \bullet \mathbf{b}_n(\mathbf{r}) = \begin{cases} l_n / A_n^+ & \mathbf{r} \in T_n^+ \\ -l_n / A_n^- & \mathbf{r} \in T_n^- \end{cases} \tag{2.32}$$

which means that each RWG basis has equal but opposite charge on the two triangles and the net charge for each RWG basis is zero.

The RWG basis function has a variety of beneficial characteristics that make it a favorable choice when compared to a wire gird modeling approach. Specifically, it eliminates fictitious loop currents and difficulties relating the modeled wire currents to the actual surface currents. It also produces better conditioned matrices and more accurate current models at frequencies near resonance.

RWG basis function **b**(**r**) is especially well suited to approximately represent surface currents. It eliminates problems associated with line charges along basis elements. The current has no component normal to the boundary (excluding the common edge or basis element) of the surface formed by T_n^+ and T_n^-. As is illustrated in Figure 2.2, the current component normal to the *n*th edge is constant and continuous across the edge. Figure 2.3 shows that the normal component of $\rho_n^{\pm}$ along edge *n* is just the height of the triangle $T_n^{\pm}$ with edge *n* as the base and the height expressed as $(2A_n^{\pm})/l_n$. The latter factor normalizes $\mathbf{b}_n$ in equation (2.31) such that its flux density normal to edge *n* is unity, ensuring continuity of the current normal to the edge. With no component normal to the boundary, the current component normal to the *n*th edge is constant and continuous across the edge, which implies that all edges of T_n^+ and T_n^- are free of line charges. The charge density is constant in each

triangle and the total charge associated with the triangle pair T_n^+ and T_n^- is zero, with the basis functions for the charge in the form of pulse doublets [39].

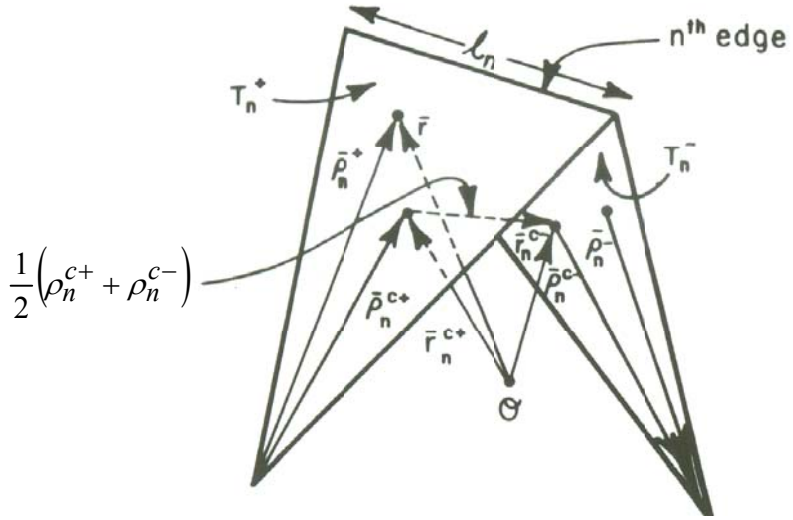

Figure 2.2. Plus and minus triangles used in determining the *n*th basis element. [29]

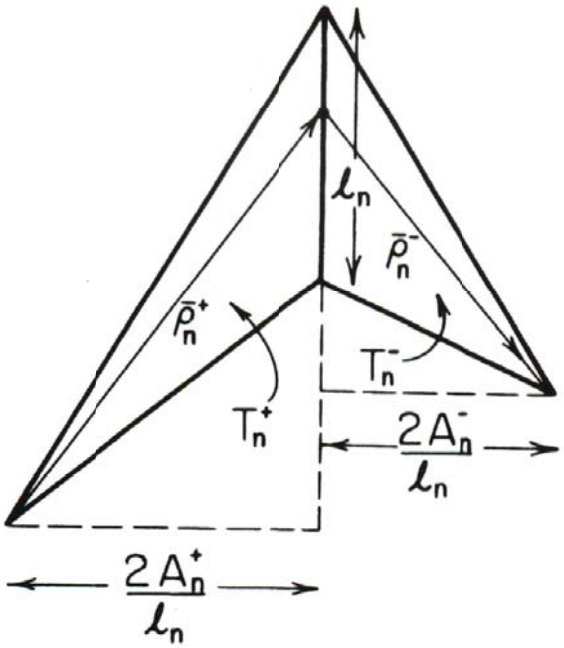

Figure 2.3. Geometry for construction of component of basis function normal to edge. [29]

2.5 Projection Error Using RWG Basis

It is well-known that the MoM is one of the most important methods in CEM because of its powerful ability in solving the integration equation of electromagnetic radiation and scattering. Like the numerical dispersion error analysis in finite element method (FEM) and finite difference in time domain (FDTD), the MoM error analysis is an important topic in CEM. The error analysis of the MoM was performed with the error measure of current, boundary condition, and scattering amplitude. As mentioned by the researchers in [40], the application of expansion and testing functions is one of the most important factors contributing to MoM error. In fact, the various basis functions play important roles in MoM. The application of the proper basis functions can facilitate the accurate and convenient modeling of the complex electromagnetic problems. It is interesting to investigate the error in projection of the equivalent current of plane wave using various basis functions. The projection error is similar to the error of approximation of the current in the MoM. For the former, the operator enforcing on the approximate current can be regarded as the identity, while for the latter, the operator is with a kernel. The projection error can serve as the reference for the MoM error analysis. The study of the projection error of basis can indirectly demonstrate how the basis functions affect the accuracy of MoM.

In this section, we analyze the projection error related to the RWG basis functions. The equivalent vector current by a plane wave in a finite area is expanded by full and half RWG basis functions, and the unknown projection coefficients are solved by the Galerkin's method. The error is calculated for different polarizations, different meshes and mesh densities, and different incident angles [41, 42].

2.5.1 Projection Error

For a plane wave incident from the direction of $(\theta_{inc}, \phi_{inc})$ and polarized in the direction of $\hat{p}$, the magnetic field is given as

$$\mathbf{H}^{inc} = H_0 \hat{p} \times \hat{k}^{inc} e^{-ik\hat{k}^{inc} \bullet \mathbf{r}} \tag{2.33}$$

where $\hat{k}^{inc} = \hat{z}\cos\theta_{inc} + \hat{k}_{inc}^{t}\sin\theta_{inc}$, $\hat{k}_{inc}^{t} = \hat{x}\cos\phi_{inc} + \hat{y}\sin\phi_{inc}$, and $\mathbf{r} = \hat{z}z + \boldsymbol{\rho}, \boldsymbol{\rho} = \hat{x}x + \hat{y}y$. The equivalent electric current on the plane of $z = 0$ is found as

$$\mathbf{J} = \hat{n} \times \mathbf{H}^{inc} = H_0 \hat{z} \times \left(\hat{p} \times \hat{k}^{inc} \right) e^{-ik\sin\theta_{inc}\hat{k}_t^{inc} \bullet \boldsymbol{\rho}} \tag{2.34}$$

For the θ-polarization, $\hat{p} = \hat{\theta}_{inc} = -\hat{z}\sin\theta_{inc} + \hat{k}_t^{inc}\cos\theta_{inc}$,

$$\mathbf{J} = H_0 \hat{k}_t^{inc} e^{-ik\sin\theta_{inc}\hat{k}_t^{inc} \bullet \boldsymbol{\rho}} \tag{2.35}$$

And for the ϕ-polarization, $\hat{p} = \hat{\phi}_{inc} = -\hat{x}\sin\phi_{inc} + \hat{y}\cos\phi_{inc}$,

$$\mathbf{J} = H_0 \cos\theta_{inc} \hat{\phi}_{inc} e^{-ik\sin\theta_{inc}\hat{k}_t^{inc} \bullet \boldsymbol{\rho}} \tag{2.36}$$

Obviously, the equivalent vector current of θ-polarization is curl-free and the current of ϕ-polarization is divergence-free.

The vector currents in equation (2.35) or (2.36) can be expanded by the RWG basis functions. The projected current is denoted as $\tilde{\mathbf{J}}$ and has a form of

$$\tilde{\mathbf{J}} = \sum_{n=1}^{N} a_n \boldsymbol{\Lambda}_n \tag{2.37}$$

where $\boldsymbol{\Lambda}_n$ is a full or half RWG basis function and a_n is the unknown coefficient, which can be solved from a linear equation derived by using the Galerkin's method.

$$\sum_{n=1}^{N} a_n \int_S dS\ \boldsymbol{\Lambda}_m \bullet \boldsymbol{\Lambda}_n = \int_S dS\ \boldsymbol{\Lambda}_m \bullet \mathbf{J}, \quad m = 1, 2, \ldots, N. \tag{2.38}$$

The relative error is defined using the L^2 norm [40] as

$$Err = \frac{\left\| \mathbf{J} - \tilde{\mathbf{J}} \right\|}{\left\| \mathbf{J} \right\|} = \frac{\sqrt{\int_S \left| \mathbf{J} - \tilde{\mathbf{J}} \right|^2 dS}}{\sqrt{\int_S \left| \mathbf{J} \right|^2 dS}} \tag{2.39}$$

The integral is performed over all triangular patches. To remove the border edge effects, S in the integral above is smaller than the S in equation (2.38).

2.5.2 Numerical Results

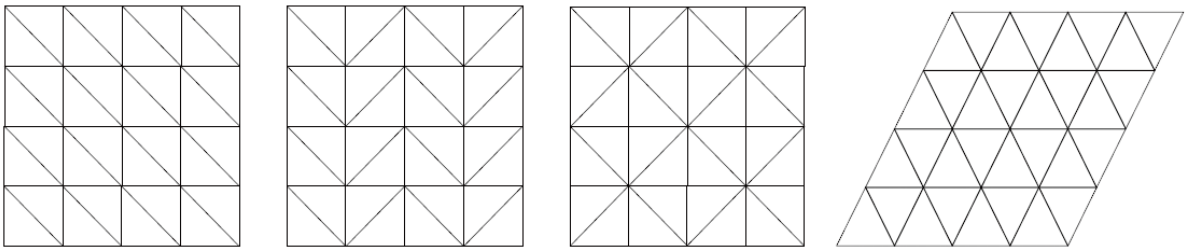

(a) One-directional (b) Arrow (c) Diamond (d) Hexagonal

Figure 2.4. Four types of triangular meshes.

The four types of triangular mesh investigated in this work are one-directional, arrow, diamond, and hexagonal mesh [43], as shown in Figure 2.4. In the first three meshes, each square is divided into two right-angle isosceles triangles. The hexagonal mesh consists of equilateral triangles. For each mesh, the shortest distance between nodes is set to a. Figure 2.5 shows the polar plot of the projection error for one-directional mesh as a function of ϕ_{inc} with the different incident angle θ_{inc} of the plane wave. It is found that the error in the projection of θ-polarization current (curl-free vector) is less than that of ϕ-polarization (divergence-free vector). This is because that the RWG basis functions are curl-free. Meanwhile, as shown in Figure 2.5, the projection error is anisotropic and varies with the direction of propagation. Also, the severity of the anisotropic behavior relates to the element arrangement of the meshes and the polarization of the incident plane wave. Figure 2.5 also

demonstrates that the smaller θ_{inc}, the smaller the projection error. From equation (2.35) or (2.36), we find that the apparent wavelength on the plane of $z=0$ is $\lambda/\sin\theta_{inc}$, which leads to more unknowns per wavelength than the original mesh ($\lambda/a=10$). To verify it, we plot the projection error normalized by $\sin\theta_{inc}$ in Figure 2.6. It shows that the normalized error hardly depends on the incident angle θ_{inc}; therefore, in the following figures, θ_{inc} is close to 90 degrees and the error is normalized.

Figure 2.7 shows the projection error as a function of the incident angle ϕ_{inc} for 4 different meshes with $\lambda/a=10$. It is observed again that the error in the projection of θ-polarization current is less than that of ϕ-polarization. For the one-directional, arrow, and diamond meshes, the projection errors are different for the ϕ-polarization; however, they agree with each other for the θ-polarization. The error in the hexagonal mesh is almost omni-directional and less than the errors in the other three meshes, where the longest edge is $\sqrt{2}a$. The shape of the error curves for the ϕ-polarization is similar to the phase error in the finite element method using triangular nodal elements [43]. Additionally, numerical results of projection errors have been confirmed by analytical results in [42].

In Figure 2.8, the projection error plotted as a function of ϕ_{inc} with three different values of a/λ has the same shape but different magnitude. The smaller the value of a/λ, the smaller the error. Furthermore, it is found that the error is linearly proportional to a/λ. In addition, the projection error for a sphere represented by 1800 flat triangles is demonstrated in Figure 2.9 for both polarizations.

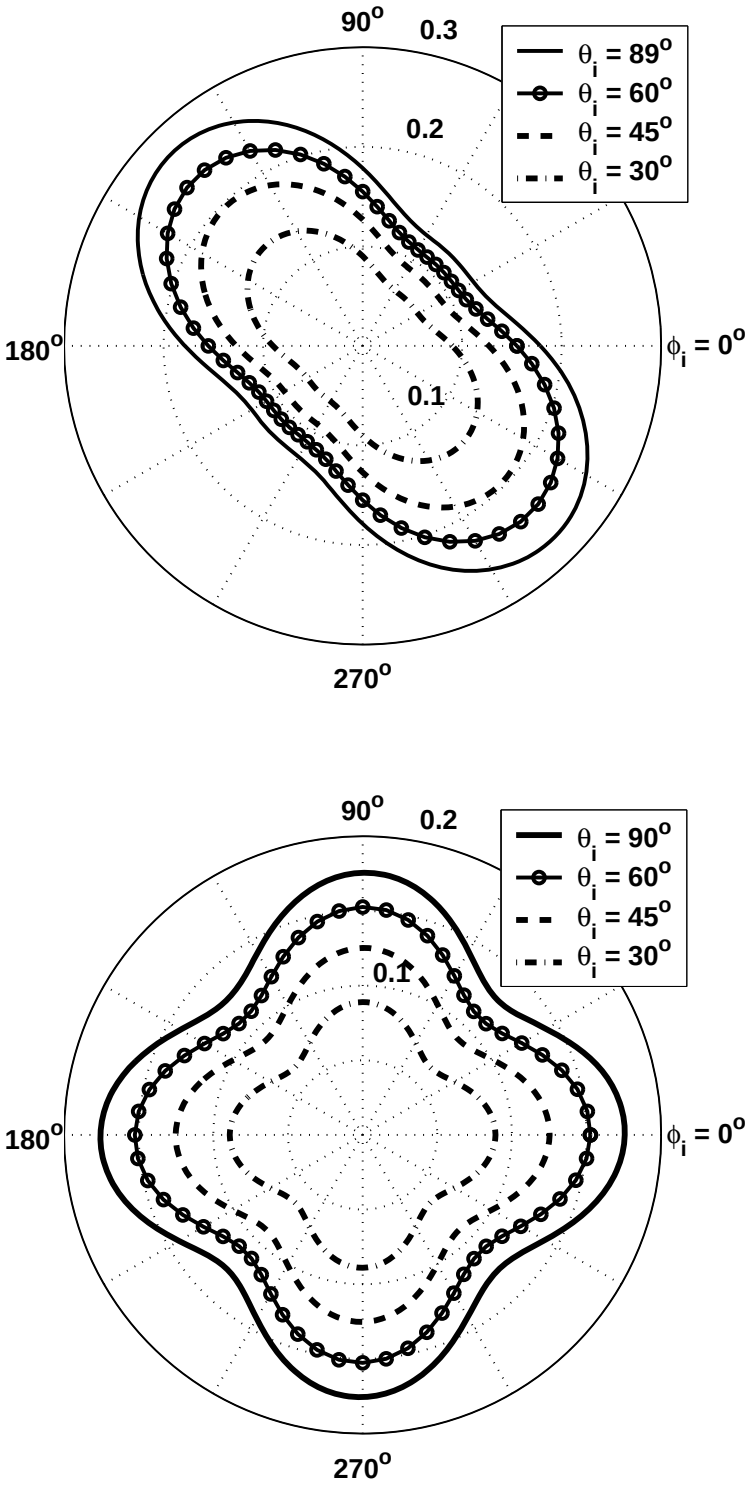

Figure 2.5 Projection error for one-directional mesh as a function of ϕ_{inc} for λ / a = 10, with four incident angles θ_{inc}. Top: ϕ-polarization; Bottom: θ-polarization.

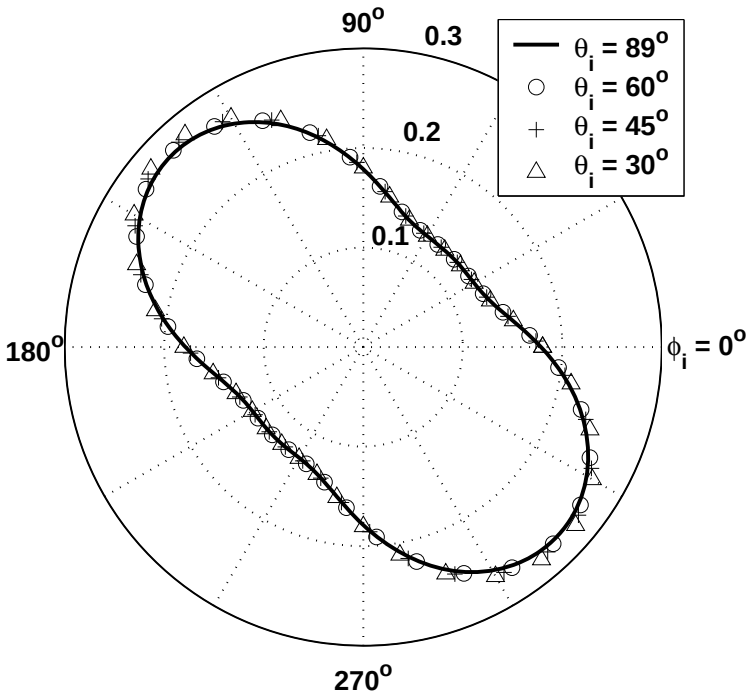

Figure 2.6 Projection error normalized by $\sin\theta_{inc}$ for one-directional mesh as a function of ϕ_{inc} for $\lambda / a = 10$, with four incident angles θ_{inc} and ϕ-polarization.

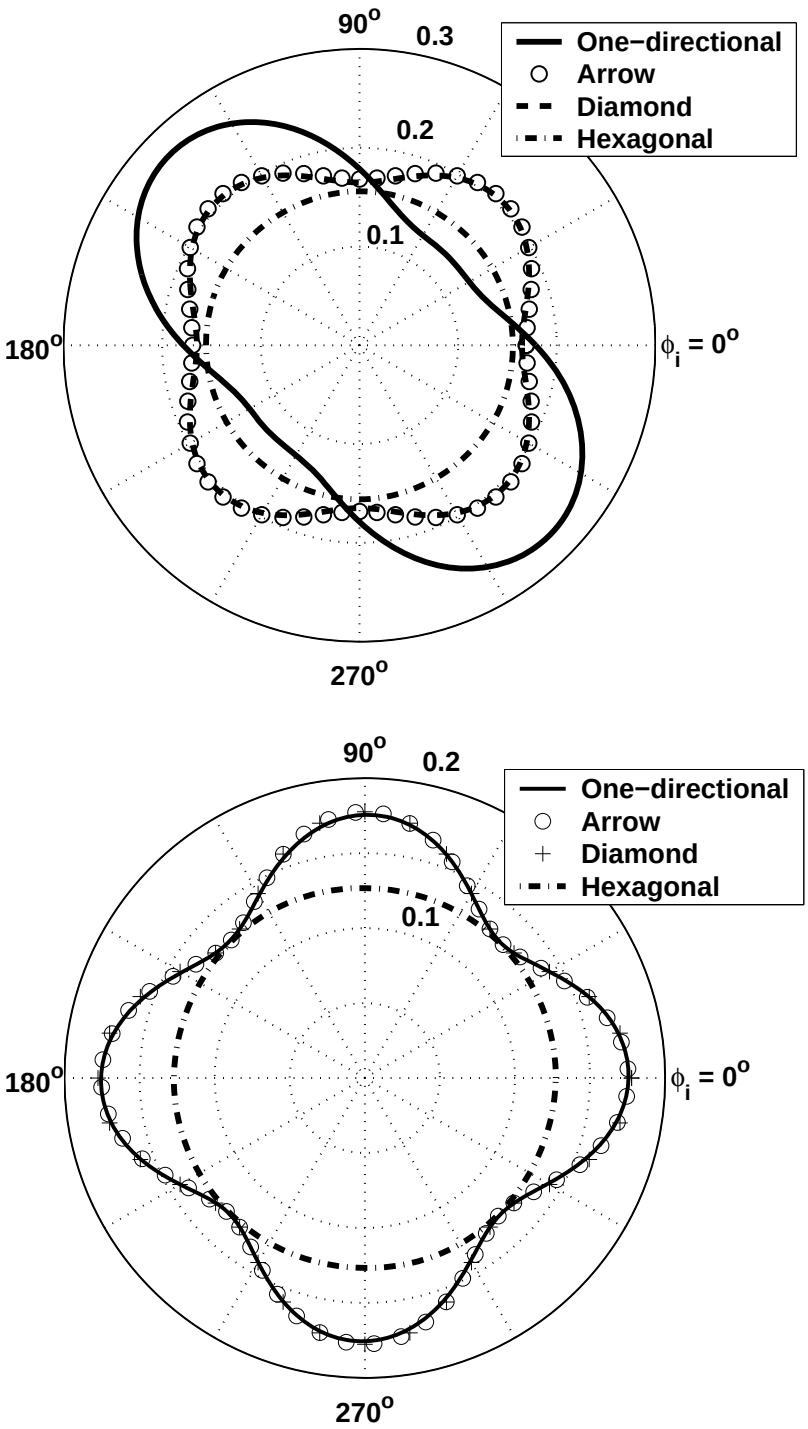

Figure 2.7 Projection error as a function of ϕ_{inc} for λ / a = 10, with four different meshes. Top: ϕ-polarization; Bottom: θ-polarization.

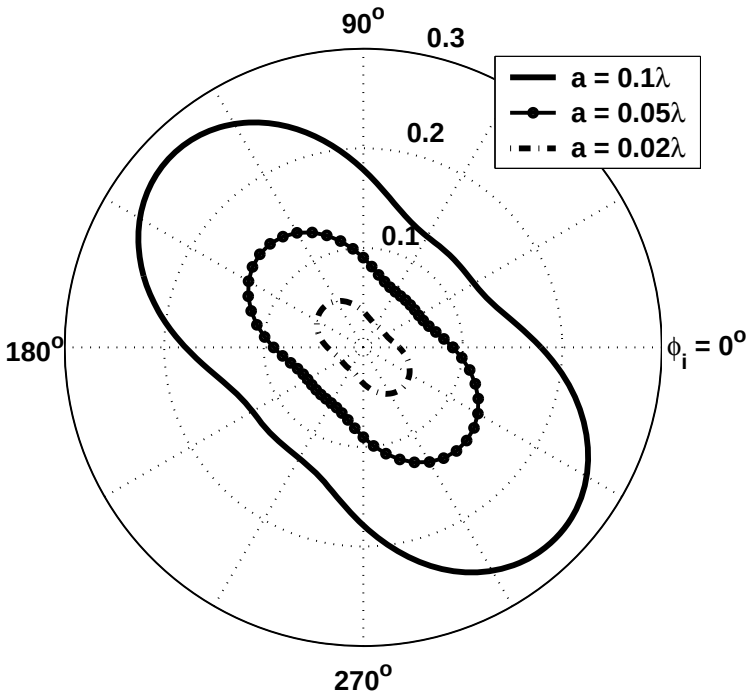

Figure 2.8 Projection error for the one-directional mesh as a function of ϕ_{inc}, with the different values of a/λ and ϕ-polarization.

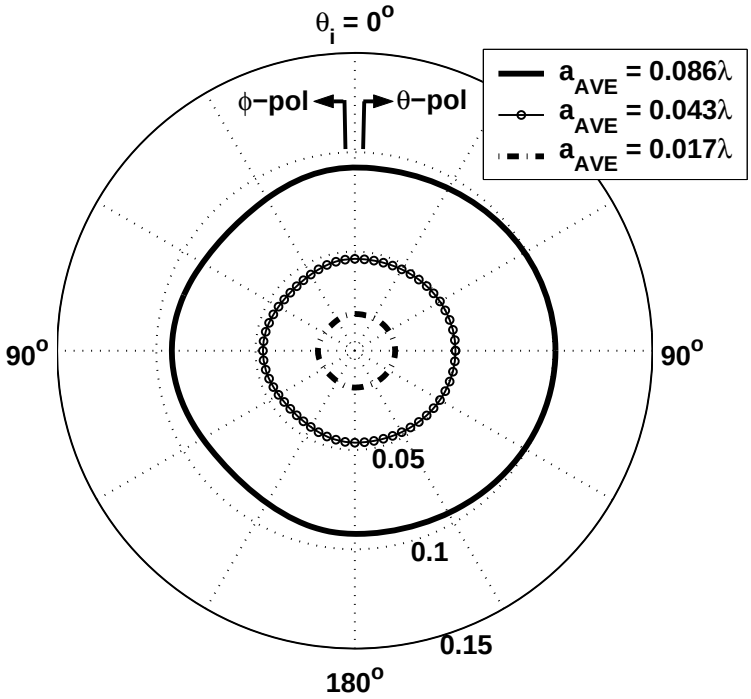

Figure 2.9 Projection error for a sphere as a function of θ_{inc}, with the different values of average edge length. Left: ϕ-polarization; Right: θ-polarization.

CHAPTER 3. FAST MULTIPOLE SOLUTIONS FOR DIFFUSIVE SCALAR PROBLEM

In what follows, we solve the two-dimensional Helmholtz equation with a complex wave number for non-trivial boundary geometry and describe the FMM acceleration procedure of the BIE method and its features [44, 45].

3.1 Diffusion Problem

The boundary integral equation for the Helmholtz equation $\nabla^2 u + k^2 u = 0$ can be written as

$$\frac{1}{2}u(\boldsymbol{\rho}) = \int_S \left[G_k(\boldsymbol{\rho},\boldsymbol{\rho}') \frac{\partial u(\boldsymbol{\rho}')}{\partial n'} - \frac{\partial G_k(\boldsymbol{\rho},\boldsymbol{\rho}')}{\partial n'} u(\boldsymbol{\rho}') \right] dS(\boldsymbol{\rho}') \tag{3.1}$$

where S is the boundary of the interest domain, $\boldsymbol{\rho}, \boldsymbol{\rho}' \in S$ are the source and field points, respectively, and $G_k(\boldsymbol{\rho},\boldsymbol{\rho}')$ is the free-space Green's function for the Helmholtz equation. Here, we simply assume that the source point is on a smooth boundary segment, without resorting to the more general weakly singular formulation [46]. The Green's function $G_k(\boldsymbol{\rho},\boldsymbol{\rho}')$ in two dimensions is given by

$$G_k(\boldsymbol{\rho},\boldsymbol{\rho}') = \frac{i}{4} H_0^{(1)}(k\,|\boldsymbol{\rho}-\boldsymbol{\rho}'|) \tag{3.2}$$

where $H_0^{(1)}$ is the Hankel function of the first kind of order zero.

3.1.1 Dirichlet Boundary Condition

u is given and the integral equation (3.1) is solved for $\frac{\partial u}{\partial n'}$.

$$\int_S G_k(\boldsymbol{\rho},\boldsymbol{\rho}')\frac{\partial u(\boldsymbol{\rho}')}{\partial n'}dS(\boldsymbol{\rho}')=\int_S \frac{\partial G_k(\boldsymbol{\rho},\boldsymbol{\rho}')}{\partial n'}u(\boldsymbol{\rho}')dS(\boldsymbol{\rho}')+\frac{1}{2}u(\boldsymbol{\rho}) \tag{3.3}$$

Now, we illustrate a discretization of the integral equation for the Dirichlet boundary condition by using the method of moments with the pulse functions as basis functions and Dirac delta functions as testing functions. The boundary S is partitioned into N cells and the unknown function $\frac{\partial u}{\partial n'}$ is expanded as

$$\frac{\partial u}{\partial n'}=\sum_{i=1}^{N} x_i b_i(\boldsymbol{\rho}) \tag{3.4}$$

where $b_i(\boldsymbol{\rho})$ is the pulse basis function. Then testing the integral equation by point matching leads to

$$\sum_{i=1}^{N} A_{ji}x_i = y_j \quad j=1,2,...,N \tag{3.5}$$

A_{ji} in the left-hand-side (LHS) has a form of

$$A_{ji}=\int_S G_k(\boldsymbol{\rho}_j,\boldsymbol{\rho}')b_i(\boldsymbol{\rho}')dS(\boldsymbol{\rho}')=\int_{S_i} G_k(\boldsymbol{\rho}_j,\boldsymbol{\rho}')dS(\boldsymbol{\rho}')=\int_{S_i}\frac{i}{4}H_0^{(1)}(k\left|\boldsymbol{\rho}_j-\boldsymbol{\rho}'\right|)dS(\boldsymbol{\rho}') \tag{3.6}$$

The right-hand-side (RHS) can be obtained by evaluating the integral at $\boldsymbol{\rho}_j$.

$$y_j=\int_S \frac{\partial G_k(\boldsymbol{\rho}_j,\boldsymbol{\rho}')}{\partial n'}u(\boldsymbol{\rho}')\,dS(\boldsymbol{\rho}')+\frac{1}{2}u(\boldsymbol{\rho}_j)=\int_S \frac{i}{4}\frac{\partial H_0^{(1)}(k\left|\boldsymbol{\rho}_j-\boldsymbol{\rho}'\right|)}{\partial n'}u(\boldsymbol{\rho}')dS(\boldsymbol{\rho}')+\frac{1}{2}u(\boldsymbol{\rho}_j) \tag{3.7}$$

3.1.2 Neumann Boundary Condition

u is solved from the integral equation for the given $\frac{\partial u}{\partial n'}$,

$$\int_S \frac{\partial G_k(\boldsymbol{\rho},\boldsymbol{\rho}')}{\partial n'} u(\boldsymbol{\rho}') dS(\boldsymbol{\rho}') + \frac{1}{2} u(\boldsymbol{\rho}) = \int_S G_k(\boldsymbol{\rho},\boldsymbol{\rho}') \frac{\partial u(\boldsymbol{\rho}')}{\partial n'} dS(\boldsymbol{\rho}') \tag{3.8}$$

Similarly,

$$A_{ji} = \int_{S_i} \frac{\partial G_k(\boldsymbol{\rho}_j,\boldsymbol{\rho}')}{\partial n'} dS(\boldsymbol{\rho}') + \frac{1}{2}\delta_{ij} = \frac{i}{4}\int_{S_i} \frac{\partial H_0^{(1)}(k|\boldsymbol{\rho}_j - \boldsymbol{\rho}'|)}{\partial n'} dS(\boldsymbol{\rho}') + \frac{1}{2}\delta_{ij} \tag{3.9}$$

And

$$y_j = \int_S G_k(\boldsymbol{\rho}_j,\boldsymbol{\rho}') \frac{\partial u(\boldsymbol{\rho}')}{\partial n'} dS(\boldsymbol{\rho}') = \frac{i}{4}\int_S H_0^{(1)}(k|\boldsymbol{\rho}_j - \boldsymbol{\rho}'|) \frac{\partial u(\boldsymbol{\rho}')}{\partial n'} dS(\boldsymbol{\rho}') \tag{3.10}$$

3.2 Fast Multipole Accelerated BIE Method

The main idea of the fast multipole BIE method is to translate the element-to-element interactions to group-to-group interactions by using multipole expansions and translation [22, 23], where elements have a quad tree structure in two dimensional cases. First, the elements are divided into groups. Then, addition theorem is used to translate the diffusion field of different scattering centers within a group into a single center (aggregation). Hence, the number of scattering centers is reduced. Similarly, for each group, the field scattered by all the other group centers can be first "received" by the group center, and then "redistribute" to the elements belonging to the group (disaggregation). To solve the diffusion problem above using the FMM, the key part is the multipole expansion of the Hankel function. Letting $\boldsymbol{\rho}_j$ and $\boldsymbol{\rho}_i$ be the field point and source point respectively, as shown in Figure 3.1, we have

$$\boldsymbol{\rho}_{ji} = \boldsymbol{\rho}_j - \boldsymbol{\rho}_i = \boldsymbol{\rho}_j - \boldsymbol{\rho}_m + \boldsymbol{\rho}_m - \boldsymbol{\rho}_{m'} + \boldsymbol{\rho}_{m'} - \boldsymbol{\rho}_i = \boldsymbol{\rho}_{jm} + \boldsymbol{\rho}_{mm'} - \boldsymbol{\rho}_{im'} \tag{3.11}$$

where $\boldsymbol{\rho}_m$ and $\boldsymbol{\rho}_{m'}$ are the vectors of the centers of the m-th and m'-th groups, which $\boldsymbol{\rho}_j$ and $\boldsymbol{\rho}_i$ are belong to, respectively.

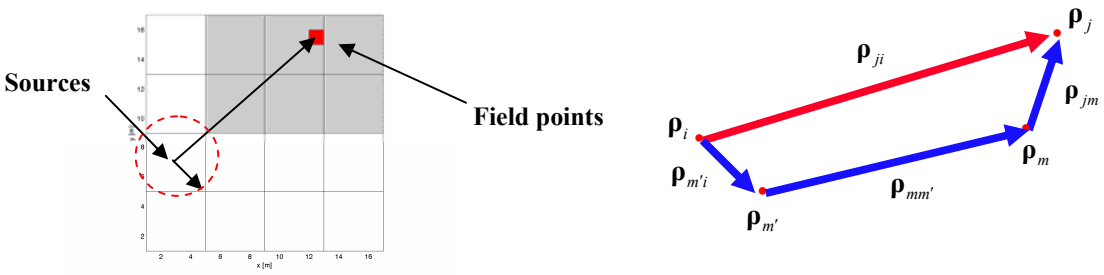

Figure 3.1. A diagram of 2-level FMM algorithm.

The basic principle behind FMM is to decompose the computation of matrix-vector products into two parts: one involving the interaction between nearby sources and the other involving those between well separated ones. That is,

$$AX = A^{near}X + A^{far}X \tag{3.12}$$

As for Dirichlet boundary condition, the zero order of Hankel function can be expressed in the Fourier space by means of the integral representation of the Bessel function [23]:

$$H_0^{(1)}(k\rho_{ji}) = \frac{1}{2\pi}\int_0^{2\pi} d\alpha\ \tilde{\beta}_{jm}(\alpha)\tilde{\alpha}_{mm'}(\alpha)\tilde{\beta}_{m'i}(\alpha) \tag{3.13}$$

where $$\tilde{\alpha}_{mm'}(\alpha) = \sum_{p=-P}^{P} H_p^{(1)}\left(k\rho_{mm'}\right)e^{-ip(\varphi_{mm'}-\alpha-\pi/2)} \tag{3.14}$$

and $$\tilde{\beta}_{jm}(\alpha) = e^{ik\rho_{jm}\cos(\alpha-\phi_{jm})} = e^{i\mathbf{k}\cdot\boldsymbol{\rho}_{jm}}, \qquad \tilde{\beta}_{m'i}(\alpha) = e^{ik\rho_{m'i}\cos(\alpha-\phi_{m'i})} = e^{i\mathbf{k}\cdot\boldsymbol{\rho}_{m'i}} \tag{3.15}$$

Furthermore, the integral can be replaced with Q-point summation:

$$H_0^{(1)}(k\rho_{ji}) = \frac{1}{Q}\sum_{q=1}^{Q} \tilde{\beta}_{jm}(\alpha_q)\tilde{\alpha}(\alpha_q)\tilde{\beta}_{m'i}(\alpha_q) \tag{3.16}$$

When using an iterative method to solve the matrix equations, a matrix-vector multiplication is to be computed in each of the iterations. As a consequence, a matrix vector multiplication involving A can be written as:

$$\begin{aligned}\sum_{i=1}^{N} A_{ji}x_i &= \sum_{m'\in B_m}\sum_{i\in G_{m'}} A_{ji}x_i + \frac{i}{8\pi}\int_0^{2\pi} d\alpha\ \tilde{\beta}_{jm}\sum_{m'\notin B_m}\tilde{\alpha}_{mm'}\sum_{i\in G_{m'}}\tilde{\beta}_{m'i}\Delta_i x_i \quad j\in G_m \\ &= \sum_{m'\in B_m}\sum_{i\in G_{m'}} A_{ji}x_i + \frac{i}{4Q}\sum_{q=1}^{Q}\tilde{\beta}_{jm}(\alpha_q)\sum_{m'\notin B_m}\tilde{\alpha}_{mm'}(\alpha_q)\sum_{i\in G_{m'}}\tilde{\beta}_{m'i}(\alpha_q)\Delta_i x_i \quad j\in G_m\end{aligned} \tag{3.17}$$

where G_m denotes all elements in the m-th group, and B_m denotes all nearby groups of the m-th group (including itself), and Δ_i denotes the i-th node segmental length. The first term in the RHS of equation (3.17) is the contribution from the nearby groups, and the second term is the far interaction calculated by FMM.

As for Neumann boundary condition, we use the fact $\frac{\partial}{\partial n_i} = n_x^i\frac{\partial}{\partial x} + n_y^i\frac{\partial}{\partial y}$, where n_x^i and n_y^i are the x and y components of the unit normal $\mathbf{n}_i$, we can show that

$$\begin{aligned}\frac{\partial H_0^{(1)}(k\rho_{ji})}{\partial n_i} &= \mathbf{n}_i \bullet \nabla^i H_0^{(1)}(k\rho_{ji}) \\ &= \frac{1}{2\pi}\int_0^{2\pi} d\alpha\ \tilde{\beta}_{jm}(\alpha)\tilde{\alpha}_{mm'}(\alpha)\frac{\partial}{\partial n_i}\tilde{\beta}_{m'i}(\alpha) \\ &= \frac{1}{2\pi}\int_0^{2\pi} d\alpha\ \tilde{\beta}_{jm}(\alpha)\tilde{\alpha}_{mm'}(\alpha)[-ik(n_x^i\cos\alpha + n_y^i\sin\alpha)]\tilde{\beta}_{m'i}(\alpha)\end{aligned} \tag{3.18}$$

Similarly, the matrix vector multiplication involving A can be written as:

$$\sum_{i=1}^{N} A_{ji}x_i = \sum_{m'\in B_m}\sum_{i\in G_{m'}} A_{ji}x_i + \frac{i}{8\pi}\int_0^{2\pi} d\alpha\ \tilde{\beta}_{jm}\sum_{m'\notin B_m}\tilde{\alpha}_{mm'}\sum_{i\in G_{m'}}[-ik(n_x^i\cos\alpha + n_y^i\sin\alpha)]\tilde{\beta}_{m'i}\Delta_i x_i \quad j\in G_m$$

$$= \sum_{m'\in B_m}\sum_{i\in G_{m'}} A_{ji}x_i + \frac{k}{4Q}\sum_{q=1}^{Q}\tilde{\beta}_{jm}(\alpha_q)\sum_{m'\notin B_m}\tilde{\alpha}_{mm'}(\alpha_q)\sum_{i\in G_{m'}}(n_x^i\cos\alpha_q + n_y^i\sin\alpha_q)\tilde{\beta}_{m'i}(\alpha_q)\Delta_i x_i \quad j\in G_m \tag{3.19}$$

3.3 Numerical Tests

In the first stage of tests, we proceed to solve the 2D Helmholtz equation using the conventional BIE method with/without the far interactions for both Dirichlet and Neumann boundary conditions and for a complex wave number k of $(1+i)/\delta$. We study the boundary shape with a side of one unit as shown in Figure 3.2, which also shows the distribution of nodes along the boundary. The numbering of boundary nodes starts from the left bottom corner and then goes counterclockwise.

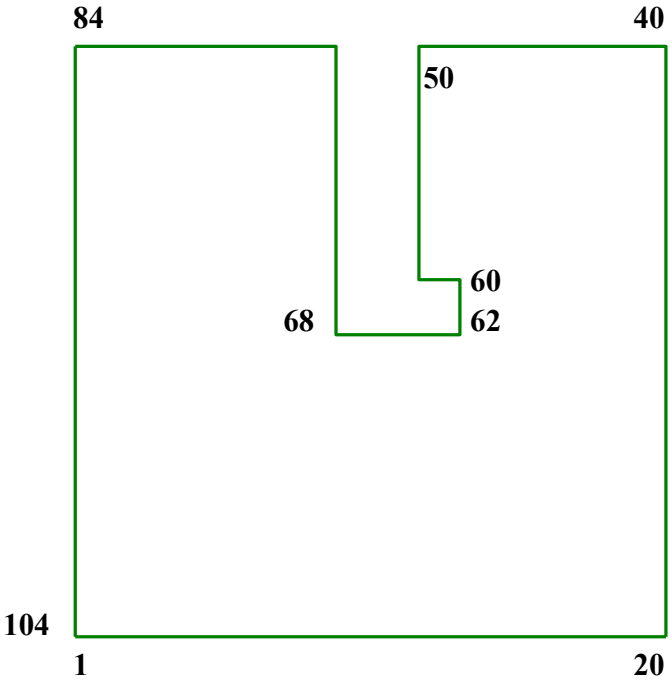

Figure 3.2. Illustration of the boundary shape of a notched square.

For the comparisons shown in Figures 3.3 and 3.4, we test the conventional BIE method solution against the exact solution of the 2D Helmholtz equation with the complex k with the skin depth δ equal to 1. The exact solution has a form of

$$u = \sin\left(\frac{k}{\sqrt{2}}x\right)\exp\left(i\frac{k}{\sqrt{2}}y\right) \tag{3.20}$$

It is shown that the numerical solutions agree well with the exact solutions for both Dirichlet and Neumann boundary conditions, which is a good preparation for the implementation of FMM.

In Figure 3.5, we plot the elapsed CPU time on a personal computer for solving the diffusion problem using the conventional BIE method, both direct solvers and iterative solvers (GMRES and BICG) are used. It is observed that for solving the matrix equation, it requires $O(N^3)$ operations using direct solvers, and $O(N^2)$ operations per iteration if iterative solvers are used, which is the benchmark of our future work.

Dividing all interactions into near and far interactions is one of key steps in FMM-accelerated BIE method. We study the error in the BIE solution without the far interactions, comparing the BIE solution including both near and far interactions. We draw a square to enclose the notched shape properly and then divide it into 10 by 10 groups. In the test, the skin depth δ is equal to 0.25, and we discard the far interactions due to the Hankel function with the complex wave number in the left hand side. Here, we set two parameters, IFAR and d/δ, and use either of them to control the near and far interactions. IFAR is defined as the minimum number of groups between two separate groups which are considered as far neighbors (interactions) in the FMM-accelerated BIE method and d is defined as the maximum Euclidian distance between the centers of two separate groups considered as near

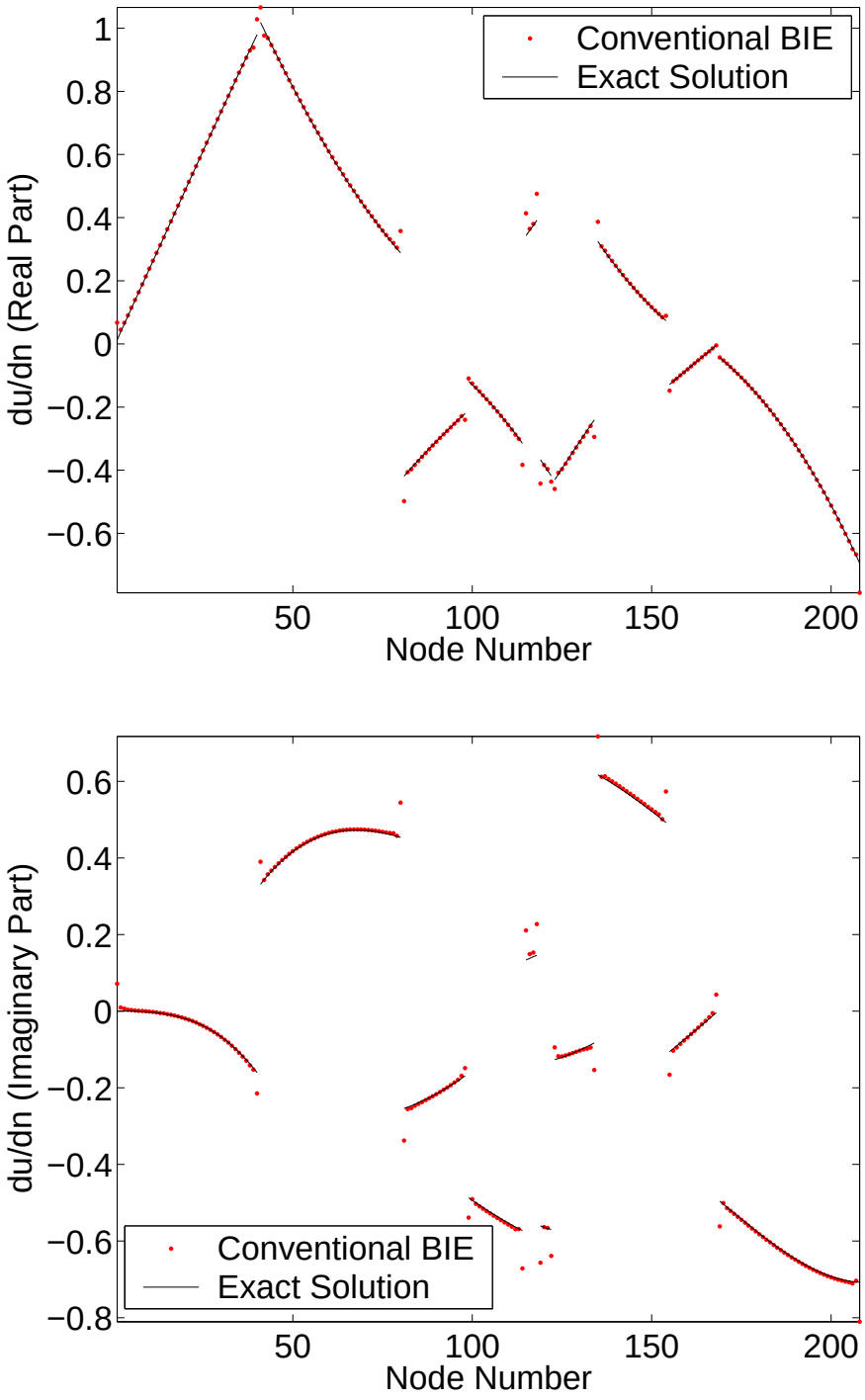

Figure 3.3. Comparison of the conventional BIE method solution with the exact solution for the Dirichlet boundary condition for the notched shape shown in Figure 3.2. Top: Real part of the solution; Bottom: Imaginary part of the solution.

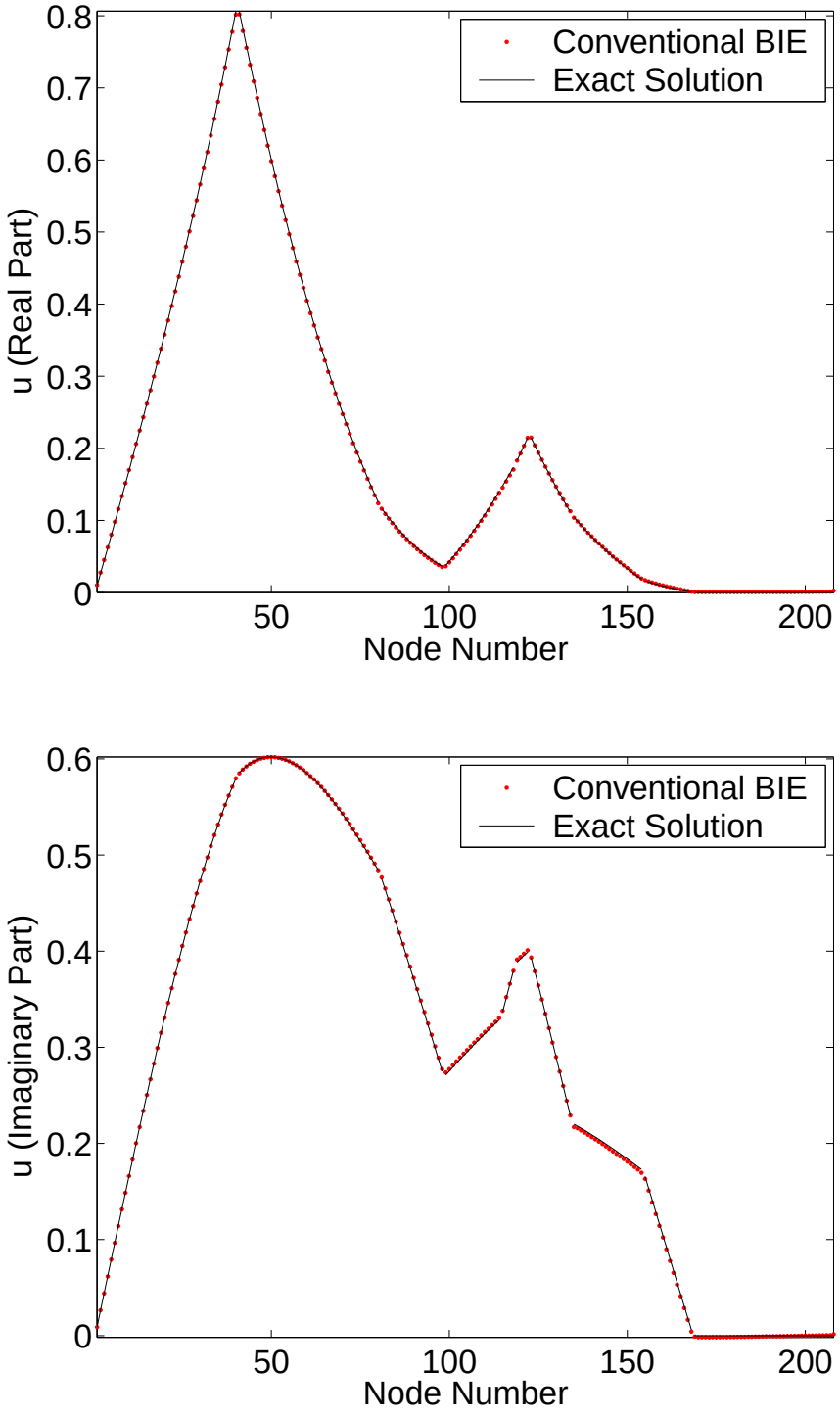

Figure 3.4. Same as Figure 3.3 except testing for the Neumann boundary condition.

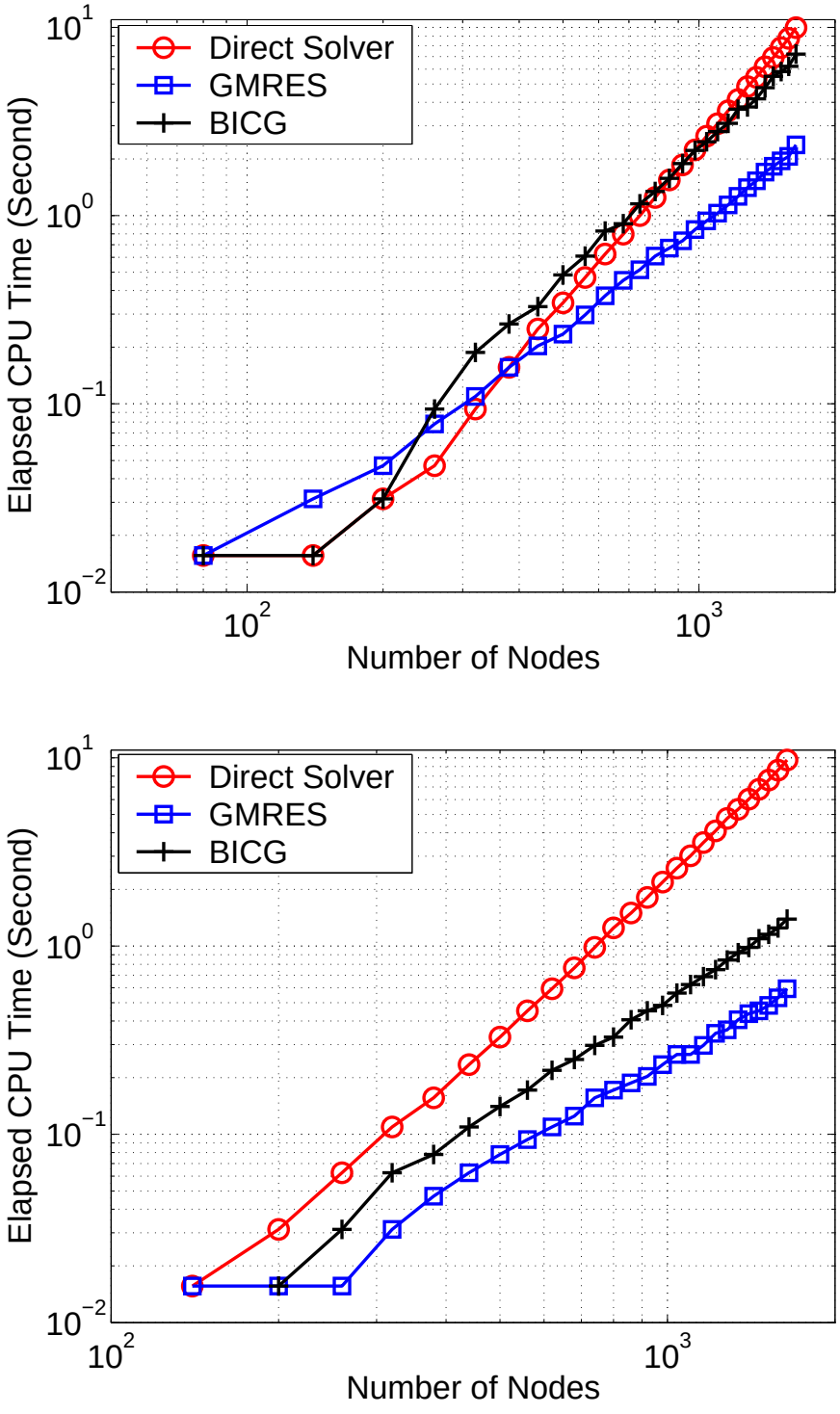

Figure 3.5. Comparison of the elapsed CPU time for solving this diffusion problem using the conventional BIE method for direct solver and iterative solvers (GMRES, BICG). Top: Dirichlet boundary condition; Bottom: Neumann boundary condition.

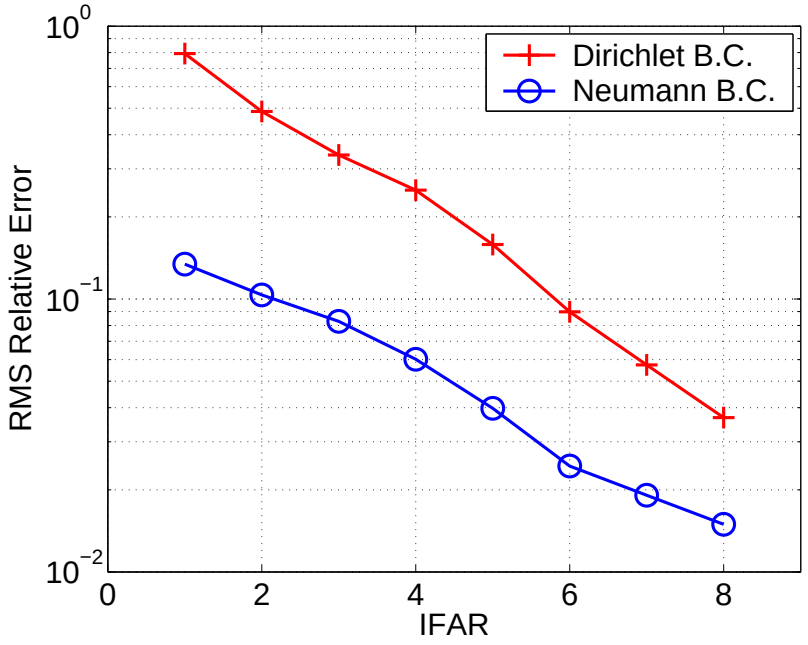

Figure 3.6. Relative RMS error in the BIE solution without the far interactions, comparing the BIE solution including both near and far interactions for Dirichlet and Neumann boundary conditions. IFAR is defined as the minimum number of groups between two separate groups which are considered as far neighbors (interactions).

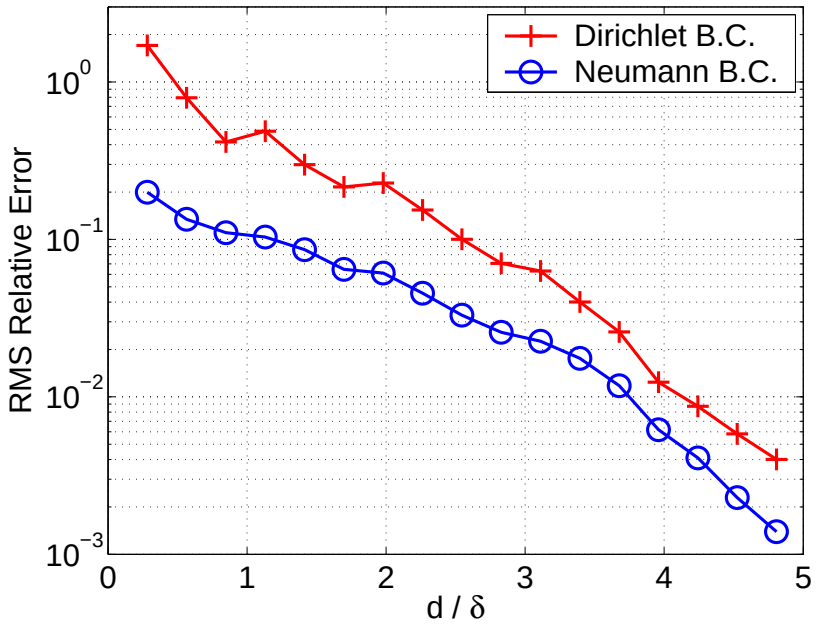

Figure 3.7. Same as Figure 3.6 except the near interaction solution is controlled by the relative distance to skin depth (d / δ).

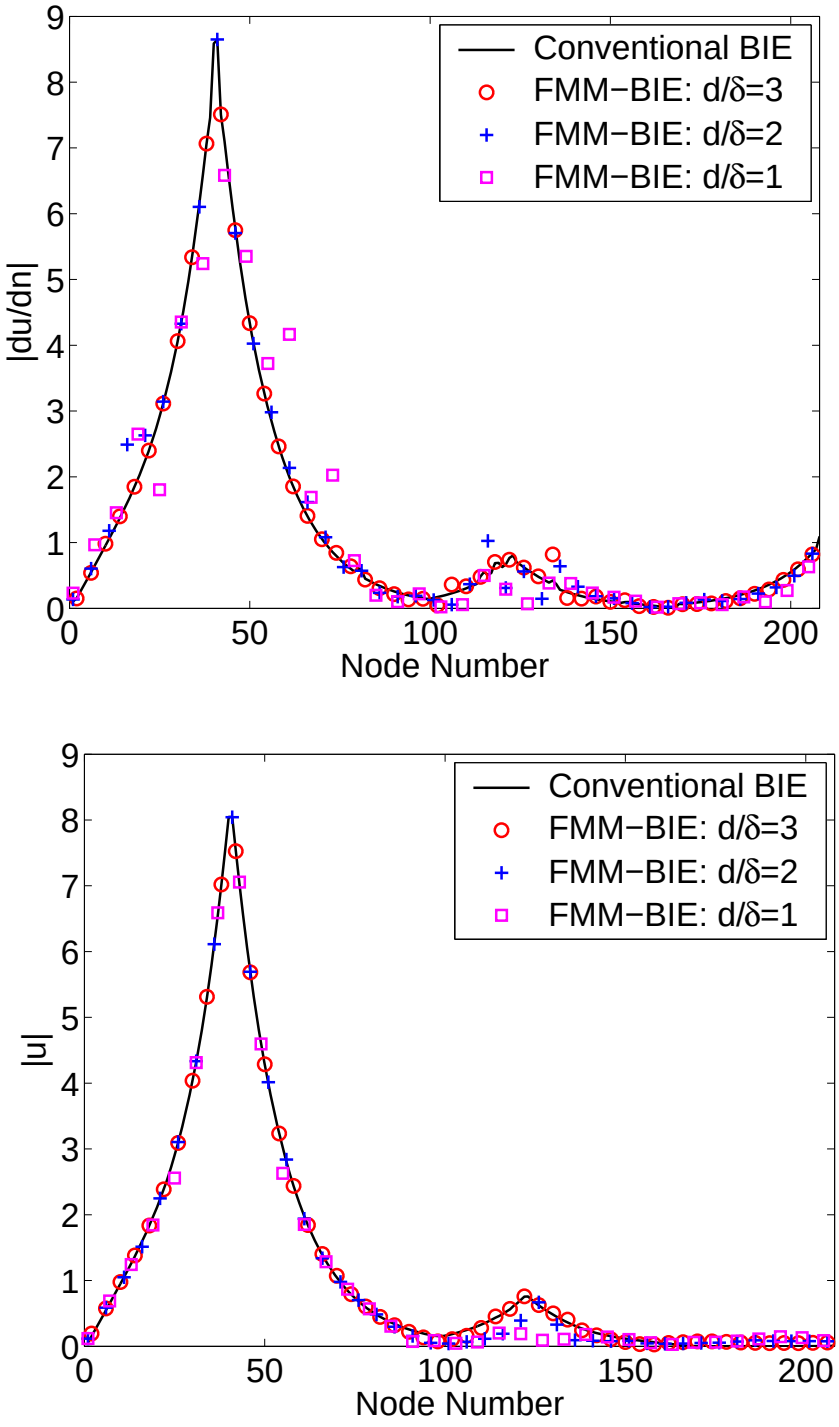

Figure 3.8. Absolute values of the BIE solutions without the far interactions controlled by d/δ, comparing the conventional BIE solution including both near and far interactions. Top: Dirichlet boundary condition; Bottom: Neumann boundary condition.

neighbors and then d/δ is the relative distance to skin depth.

In addition, the RMS relative error is defined using the L^2 norm [40] as

$$\text{Error}_{RMS} = \frac{\|\mathbf{P}_A - \mathbf{P}_B\|}{\|\mathbf{P}_B\|} = \frac{\sqrt{\sum |\mathbf{P}_A - \mathbf{P}_B|^2}}{\sqrt{\sum |\mathbf{P}_B|^2}} \tag{3.21}$$

where $\mathbf{P}_A$ and $\mathbf{P}_B$ are the complex numerical solutions when using the BIE method without far interactions and the conventional BIE method, respectively.

In Figures 3.6 and 3.7, we plot the relative RMS error in the BIE solution without the far interactions, comparing with the BIE solution including both near and far interactions for both Dirichlet and Neumann boundary conditions, and for two different parameters, IFAR and d/δ, respectively. It is observed that the accuracy increases dramatically when we keep more and more near interactions and throw away less and less far interactions. Additionally, as shown in Figure 3.8, the BIE solutions without the far interactions for both boundary conditions appropriately agree with the conventional BIE solution when d exceeds the triple skin depth.

In the second stage of tests, we work with the two-dimensional Helmholtz equation using the conventional BIE method and the two-level FMM BIE method for both Dirichlet and Neumann boundary conditions and for a complex wave number k of $(1+i)/\delta$, where δ is the skin depth. In the numerical test, our geometry of interest is a notched square with an area of $4\delta \times 4\delta$, as also shown in Figure 3.2. The numbering of boundary nodes starts from the left bottom corner and then goes counterclockwise. The total numbers of nodes is 208, 416, 832, 1664, 3328, 6656, 8320 and 10400, respectively. A square is drawn to enclose the notched

shape properly and then divided into m by m groups (m increasing by a factor of $\sqrt{2}$). Moreover, IFAR, a controlling parameter, which is defined as the minimum number of groups between two separate groups considered as far interactions in the FMM-accelerated BIE method, is set to 1. The numerical tests are performed on a PC (Dual Core CPU, 4.0 GB of RAM) running Linux. Stopping criteria for iterative solver GMRES is set to 10^{-5} and restart number for it is 10. Meanwhile, the relative RMS error is defined by equation (3.21), in which $\mathbf{P}_A$ and $\mathbf{P}_B$ are the complex numerical solutions when using the FMM BIE method and the conventional BIE method, respectively.

For the comparisons shown in Tables 3.1 and 3.2, we test the FMM BIE method solution against the conventional BIE method solution of the two-dimensional Helmholtz equation for Dirichlet and Neumann boundary conditions with node number N increasing and then list the elapsed CPU time in seconds and RMS relative errors. As for the conventional BIE method, the total CPU time includes two parts: matrix filling and solving. Since the conventional BIE method generates a dense matrix, it requires $O(N^2)$ operations to compute left hand side (LHS) matrix and another $O(N^3)$ operations to solve the equations using direct solver LUD for both boundary conditions, as shown in Table 3.1. For a fair comparison, the CPU time for solving the full matrix equations using iterative solver GMRES is also recorded, which requires $O(N^2)$ operations per iteration. As for the FMM BIE method, the total CPU time includes three parts: pre-calculation, matrix filling, and solving using iterative solver GMRES. In contrast to the conventional BIE method, the two-level FMM BIE method reduces the operations per iteration and memory requirement to $O(N^{3/2})$, while the solution is still in the same order accuracy, as shown in Table 3.2. Then, in Figure 3.9, we plot the CPU time per iteration using FMM BIE method for solving the diffusion problem with iterative

solver GMRES against the CPU time using the conventional BIE method with direct solver LUD and iterative solver GMRES for Dirichlet boundary condition. After curve fitting of last six points, it is observed that for solving our full matrix equations, it requires $O(N^{3.05})$ operations using direct solver LUD, and $O(N^{2.08})$ operations per iteration if iterative solver GMRES is used; however, it only requires $O(N^{1.43})$ operations per iteration using fast multiple method with GMRES to solve the matrix equations. Moreover, it is a similar case for Neumann boundary condition.

Last but not least, it is demonstrated in Figure 3.10 that the conventional BIE method requires $O(N^{2.01})$ operations to compute left hand side (LHS) matrix for this two-dimensional diffusion problem while the two-level FMM BIE method reduces operation complexity to $O(N^{1.17})$ for Dirichlet boundary condition by applying asymptotic curve fitting.

Table 3.1. Comparison of elapsed CPU time for solving the diffusion problem using the conventional BIE method and FMM BIE method for both Dirichlet and Neumann boundary conditions.

CPU Time (*sec*)	Node Number							
	208	416	832	1664	3328	6656	8320	10400
	m=6	*m*=8	*m*=12	*m*=16	*m*=24	*m*=32	*m*=35	*m*=40
Dirichlet Boundary Condition								
Conv BIE: Matrix Filling	0.22	0.76	2.37	9.51	38.67	154.96	241.98	374.50
Conv BIE: LUD	0.01	0.10	0.51	4.02	32.28	269.39	538.04	1064.09
Conv BIE: Full Matrix GMRES	0.01	0.03	0.11	0.55	2.72	12.67	24.84	41.45
CPU time per iteration	0.00040	0.00094	0.00275	0.01079	0.04387	0.17597	0.30293	0.49345
FMM BIE: Pre-Calculation	0.04	0.09	0.22	0.43	0.98	1.81	2.21	2.24
FMM BIE: Matrix Filling	0.03	0.05	0.09	0.24	0.61	1.74	2.48	3.36
FMM BIE: GMRES	0.01	0.02	0.03	0.06	0.19	0.58	0.88	1.41
CPU time per iteration	0.00040	0.00063	0.00073	0.00120	0.00311	0.00806	0.01128	0.01720
Neumann Boundary Condition								
Conv BIE: Matrix-Fill	0.25	0.82	2.70	10.80	43.77	175.19	274.71	430.55
Conv BIE: LUD	0.01	0.08	0.49	3.81	30.46	258.08	507.10	991.14
Conv BIE: Full Matrix GMRES	0.00	0.01	0.02	0.12	0.47	1.88	3.73	7.05
CPU time per iteration	0.00000	0.00100	0.00250	0.01200	0.04700	0.18800	0.33909	0.64091
FMM BIE: Pre-Calculation	0.04	0.09	0.22	0.43	0.99	1.82	2.14	2.34
FMM BIE: Matrix-Fill	0.03	0.05	0.10	0.27	0.67	1.94	2.78	3.76
FMM BIE: GMRES	0.01	0.01	0.01	0.03	0.05	0.09	0.12	0.18
CPU time per iteration	0.00111	0.00111	0.00125	0.00300	0.00500	0.00900	0.01200	0.01800

Table 3.2. Comparison of relative RMS errors for solving the diffusion problem using the conventional BIE method and FMM BIE method for both Dirichlet and Neumann boundary conditions.

Boundary Condition	Node Number							
	208	416	832	1664	3328	6656	8320	10400
	m=6	m=8	m=12	m=16	m=24	m=32	m=35	m=40
Dirichlet	0.0128	0.0105	0.0097	0.0119	0.0128	0.0130	0.0130	0.0127
Neumann	0.0080	0.0055	0.0050	0.0049	0.0046	0.0044	0.0042	0.0041

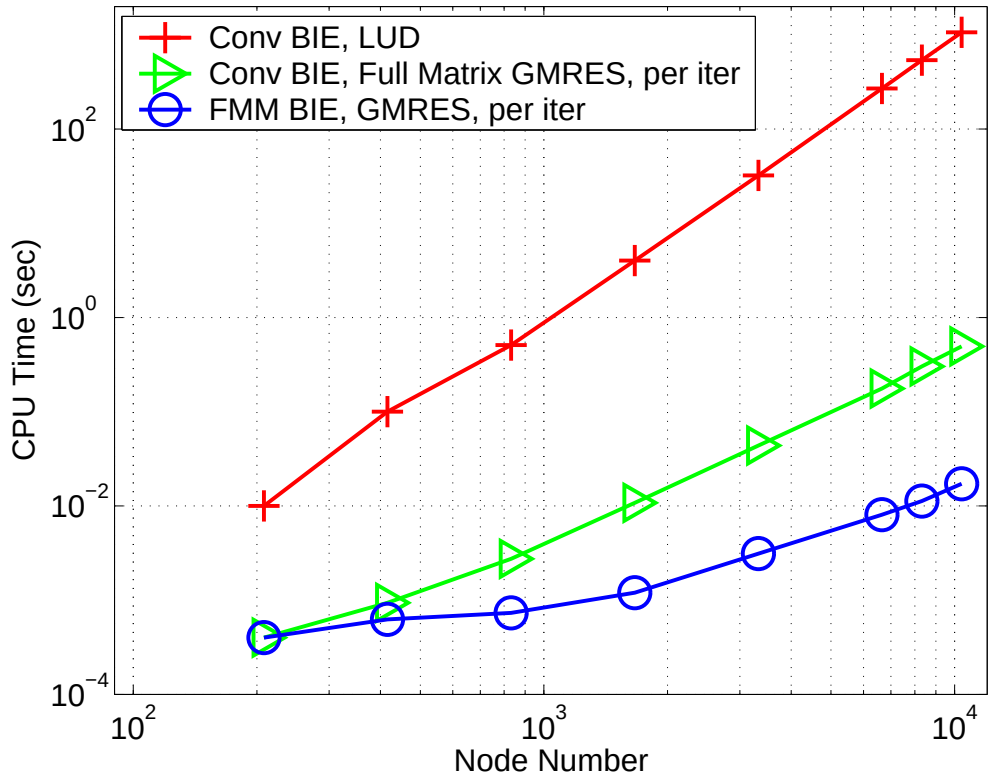

Figure 3.9. Comparison of the CPU time using the conventional BIE method with direct solver LUD or iterative solver GMRES and using FMM BIE method with GMRES to solve the two-dimensional diffusion problem for Dirichlet boundary condition.

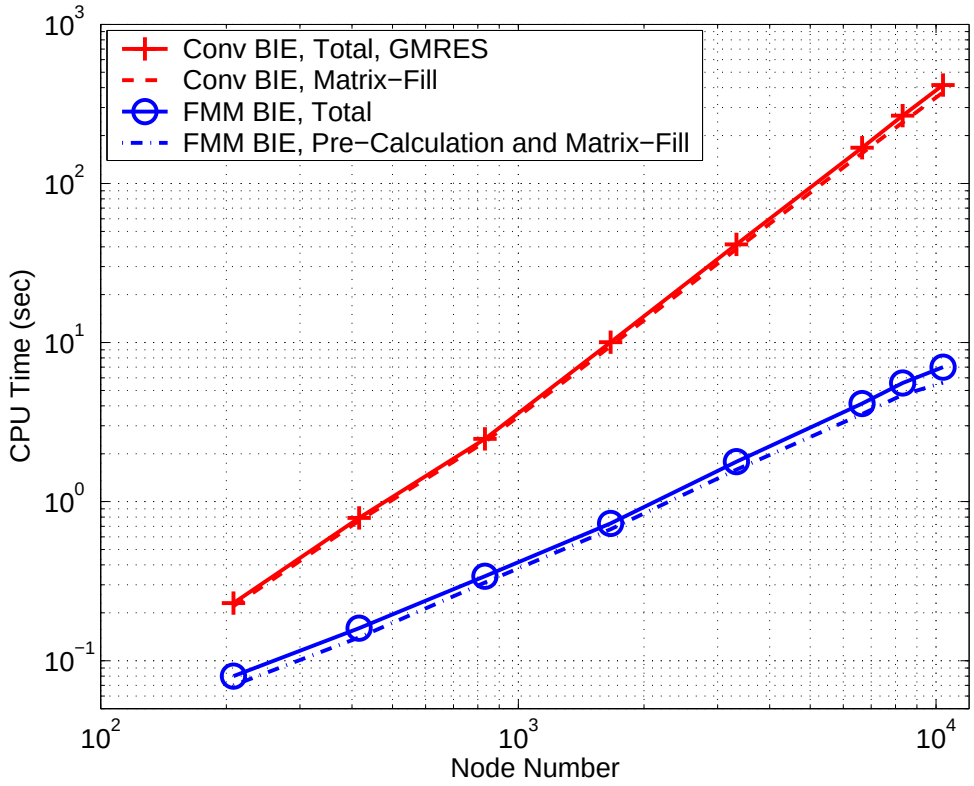

Figure 3.10. Comparison of the total elapsed CPU time using the conventional BIE method and the FMM BIE method with iterative solver GMRES for Dirichlet boundary condition and the CPU time of pre-calculation and matrix filling parts in these two methods.

CHAPTER 4. BOUNDARY ELEMENT METHOD FOR EDDY CURRENT NONDESTRUCTIVE EVALUATION

In what follows, we introduce a boundary integral equation (BIE) method for the eddy current NDE in three dimensions and demonstrate an implementation of the Stratton-Chu formulation [28] for the conductive medium. The problem is formulated by the BIE and discretized into matrix equations by the method of moments (MoM) [27] or the boundary element method (BEM).

4.1 Stratton-Chu Formulation

4.1.1 General Form

We start with Maxwell's equations, which include both electric and magnetic currents. This will help us identify the equivalent surface currents and derive the field equivalence principle.

Taking the curls of both sides of Ampere's and Faraday's laws and using the vector identity $\nabla\times(\nabla\times\mathbf{E})=\nabla(\nabla\bullet\mathbf{E})-\nabla^2\mathbf{E}$, we obtain the following inhomogeneous Helmholtz equations [47] which are duals of each other:

$$\nabla^2\mathbf{E}+k^2\mathbf{E}=-i\omega\mu\mathbf{J}+\frac{1}{\varepsilon}\nabla\rho+\nabla\times\mathbf{J}_m \tag{4.1}$$

$$\nabla^2\mathbf{H}+k^2\mathbf{H}=-i\omega\varepsilon\mathbf{J}_m+\frac{1}{\mu}\nabla\rho_m-\nabla\times\mathbf{J} \tag{4.2}$$

We recall that the Green's function for the Helmholtz equation is:

$$\nabla'^2G+k^2G=-\delta(\mathbf{r},\mathbf{r}'),\quad G(\mathbf{r},\mathbf{r}')=\frac{e^{ik|\mathbf{r}-\mathbf{r}'|}}{4\pi|\mathbf{r}-\mathbf{r}'|} \tag{4.3}$$

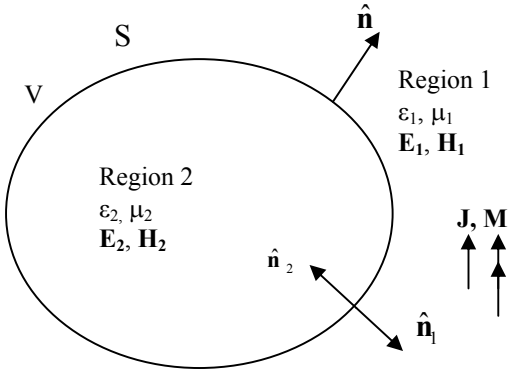

Figure 4.1. Field geometry inside and outside a closed surface *S*, where the outside (Region 1) is free space and the inside (Region 2) is a conductive medium.

where ∇' is the gradient with respect to $\mathbf{r}'$. Applying Green's second identity, we obtain:

$$\int_V \left[G\nabla'^2\mathbf{E} - \mathbf{E}\nabla'^2 G \right] dV' = -\oint_{S+S_\infty} \left[G\frac{\partial \mathbf{E}}{\partial n'} - \mathbf{E}\frac{\partial G}{\partial n'} \right] dS', \quad \frac{\partial}{\partial n'} = \hat{\mathbf{n}} \bullet \nabla' \tag{4.4}$$

where G and $\mathbf{E}$ stand for $G(\mathbf{r},\mathbf{r}')$ and $\mathbf{E}(\mathbf{r}')$ and the integration is over $\mathbf{r}'$. The quantity $\frac{\partial}{\partial n'}$ is the directional derivative along $\hat{\mathbf{n}}$. The negative sign in the right-hand side arises from using a unit vector $\hat{\mathbf{n}}$ that is pointing into the volume V, as shown in Figure 4.1.

The integral over the infinite surface is taken to be zero. This may be justified more rigorously by assuming that $\mathbf{E}$ and $\mathbf{H}$ behave like radiation fields with asymptotic form $r|\mathbf{E}| \to$ const. and $r|\mathbf{E} - \eta\mathbf{H} \times \hat{\mathbf{r}}| \to 0$. Thus, dropping the S_∞ term, and adding and subtracting $k^2 G\mathbf{E}$ in the left-hand side, we obtain:

$$\int_V \left[G(\nabla'^2\mathbf{E} + k^2\mathbf{E}) - \mathbf{E}(\nabla'^2 G + k^2 G) \right] dV' = -\oint_S \left[G\frac{\partial \mathbf{E}}{\partial n'} - \mathbf{E}\frac{\partial G}{\partial n'} \right] dS' \tag{4.5}$$

Using equation (4.3), the second term on the left hand side may be integrated to give $\mathbf{E}(\mathbf{r})$:

$$-\int_V \mathbf{E}(\mathbf{r}')(\nabla'^2 G + k^2 G)dV' = \int_V \mathbf{E}(\mathbf{r}')\delta(\mathbf{r}-\mathbf{r}')dV' = \mathbf{E}(\mathbf{r}) \tag{4.6}$$

where we assume that $\mathbf{r}$ lies in V. This integral is zero if $\mathbf{r}$ lies outside V because then $\mathbf{r}'$ can never be equal to $\mathbf{r}$. For arbitrary $\mathbf{r}$, we may write:

$$\int_V \mathbf{E}(\mathbf{r}')\delta(\mathbf{r}-\mathbf{r}')dV' = \begin{cases} \mathbf{E}(\mathbf{r}), & \text{if } r \in V \\ 0, & \text{if } r \notin V \end{cases} \tag{4.7}$$

Now we can solve equation (4.5) for $\mathbf{E}(\mathbf{r})$. In a similar fashion, or, performing a duality transformation on the expression for $\mathbf{E}(\mathbf{r})$, we also obtain the corresponding magnetic field $\mathbf{H}(\mathbf{r})$. Using equation (4.1) and (4.2), we have:

$$\mathbf{E}(\mathbf{r}) = \int_V \left[i\omega\mu G\mathbf{J} - \frac{1}{\varepsilon} G\nabla'\rho - G\nabla'\times\mathbf{J}_\mathbf{m} \right] dV' + \oint_S \left[\mathbf{E}\frac{\partial G}{\partial n'} - G\frac{\partial \mathbf{E}}{\partial n'} \right] dS' \tag{4.8}$$

$$\mathbf{H}(\mathbf{r}) = \int_V \left[i\omega\varepsilon G\mathbf{J}_m - \frac{1}{\mu} G\nabla'\rho_m - G\nabla'\times\mathbf{J} \right] dV' + \oint_S \left[\mathbf{H}\frac{\partial G}{\partial n'} - G\frac{\partial \mathbf{H}}{\partial n'} \right] dS' \tag{4.9}$$

Because of the presence of the particular surface term, we will refer to these as the Kirchhoff diffraction formulas. Equation (4.8) and (4.9) can be transformed into the so-called Stratton-Chu formulas

$$\begin{aligned} \mathbf{E}(\mathbf{r}) &= \int_V \left[i\omega\mu G\mathbf{J} + \frac{\rho}{\varepsilon}\nabla' G - \mathbf{J}_m \times \nabla' G \right] dV' \\ &\quad + \oint_S \left[i\omega\mu G(\hat{\mathbf{n}}\times\mathbf{H}) + (\hat{\mathbf{n}}\bullet\mathbf{E})\nabla' G + (\hat{\mathbf{n}}\times\mathbf{E})\times\nabla' G \right] dS' \\ &= \mathbf{E}^{inc}(\mathbf{r}) + \oint_S \left[i\omega\mu G(\hat{\mathbf{n}}\times\mathbf{H}) + (\hat{\mathbf{n}}\bullet\mathbf{E})\nabla' G + (\hat{\mathbf{n}}\times\mathbf{E})\times\nabla' G \right] dS' \end{aligned} \tag{4.10}$$

$$\begin{aligned}\mathbf{H}(\mathbf{r}) &= \int_V \left[i\omega\varepsilon G\mathbf{J}_m + \frac{\rho_m}{\mu}\nabla' G + \mathbf{J}\times\nabla' G \right] dV' \\ &\quad + \oint_S \left[-i\omega\varepsilon G(\hat{\mathbf{n}}\times\mathbf{E}) + (\hat{\mathbf{n}}\bullet\mathbf{H})\nabla' G + (\hat{\mathbf{n}}\times\mathbf{H})\times\nabla' G \right] dS' \\ &= \mathbf{H}^{inc}(\mathbf{r}) + \oint_S \left[-i\omega\varepsilon G(\hat{\mathbf{n}}\times\mathbf{E}) + (\hat{\mathbf{n}}\bullet\mathbf{H})\nabla' G + (\hat{\mathbf{n}}\times\mathbf{H})\times\nabla' G \right] dS'\end{aligned} \tag{4.11}$$

4.1.2 Low Frequency and High Conductivity Approximation

We start with the general version of the Stratton-Chu formulas that are also shown in equation (4.10) and (4.11), which explicitly contains the normal components of the surface fields.

$$\mathbf{E}(\mathbf{r}) = \mathbf{E}^{inc}(\mathbf{r}) + \oint_S \left[i\omega\mu G(\mathbf{r},\mathbf{r}')(\hat{\mathbf{n}}\times\mathbf{H}(\mathbf{r}')) + (\hat{\mathbf{n}}\bullet\mathbf{E}(\mathbf{r}'))\nabla' G(\mathbf{r},\mathbf{r}') + (\hat{\mathbf{n}}\times\mathbf{E}(\mathbf{r}'))\times\nabla' G(\mathbf{r},\mathbf{r}') \right] dS' \tag{4.12}$$

$$\mathbf{H}(\mathbf{r}) = \mathbf{H}^{inc}(\mathbf{r}) + \oint_S \left[-i\omega\varepsilon G(\mathbf{r},\mathbf{r}')(\hat{\mathbf{n}}\times\mathbf{E}(\mathbf{r}')) + (\hat{\mathbf{n}}\bullet\mathbf{H}(\mathbf{r}'))\nabla' G(\mathbf{r},\mathbf{r}') + (\hat{\mathbf{n}}\times\mathbf{H}(\mathbf{r}'))\times\nabla' G(\mathbf{r},\mathbf{r}') \right] dS' \tag{4.13}$$

where S is the boundary of the interest domain, $\mathbf{r},\mathbf{r}' \in S$ are the source and field points, respectively, and $G_j(\mathbf{r},\mathbf{r}') = e^{ik_j|\mathbf{r}-\mathbf{r}'|}/(4\pi|\mathbf{r}-\mathbf{r}'|)$, $k_j^2 = \omega^2\mu_j\varepsilon_j$, $j = 1,2$, $\hat{\mathbf{n}}$ is the unit normal direction pointing towards solution domain. These formulas provide stable solutions at low frequencies as they remain valid even in the static limit.

Then, formulas can be derived for the region 1 of free space and the region 2 with high conductivity, as shown in Figure 4.1, when the angular frequency ω approaches to zero.

For the region 1, since $\hat{\mathbf{n}}_1 = \hat{\mathbf{n}}$ and $\nabla' G_1(\mathbf{r},\mathbf{r}') = -\nabla G_1(\mathbf{r},\mathbf{r}')$, Equation (4.13) can be written as:

$$\mathbf{H}_1(\mathbf{r}) \approx \mathbf{H}^{inc}(\mathbf{r}) + \int_S \left[-\frac{1}{\mu_1}\nabla G_1(\mathbf{r},\mathbf{r}')(\hat{\mathbf{n}}\bullet\mathbf{B}(\mathbf{r}')) + \nabla G_1(\mathbf{r},\mathbf{r}')\times(\hat{\mathbf{n}}\times\mathbf{H}(\mathbf{r}')) \right] dS' \tag{4.14}$$

For the region 2, since $\hat{\mathbf{n}}_2 = -\hat{\mathbf{n}}$ and $\nabla' G_2(\mathbf{r},\mathbf{r}') = -\nabla G_2(\mathbf{r},\mathbf{r}')$, Equations (4.12) and (4.13) can be written as:

$$\begin{aligned}\mathbf{E}_2(\mathbf{r}) &= \int_S \left[-i\omega\mu_2 G_2(\mathbf{r},\mathbf{r}')(\hat{\mathbf{n}}\times\mathbf{H}(\mathbf{r}')) + \nabla G_2(\mathbf{r},\mathbf{r}'))(\hat{\mathbf{n}}\bullet\mathbf{E}(\mathbf{r}')) + (-\nabla G_2(\mathbf{r},\mathbf{r}'))\times(\hat{\mathbf{n}}\times\mathbf{E}(\mathbf{r}'))\right] dS' \\ &\approx -\int_S \left[i\omega\mu_2 G_2(\mathbf{r},\mathbf{r}')(\hat{\mathbf{n}}\times\mathbf{H}(\mathbf{r}')) + \nabla G_2(\mathbf{r},\mathbf{r}')\times(\hat{\mathbf{n}}\times\mathbf{E}(\mathbf{r}'))\right] dS'\end{aligned} \tag{4.15}$$

$$\mathbf{H}_2(\mathbf{r}) = \int_S \left[i\omega\varepsilon_2 G_2(\mathbf{r},\mathbf{r}')(\hat{\mathbf{n}}\times\mathbf{E}(\mathbf{r}')) + \frac{1}{\mu_2}\nabla G_2(\mathbf{r},\mathbf{r}')(\hat{\mathbf{n}}\bullet\mathbf{B}(\mathbf{r}')) - \nabla G_2(\mathbf{r},\mathbf{r}')\times(\hat{\mathbf{n}}\times\mathbf{H}(\mathbf{r}'))\right] dS' \tag{4.16}$$

where $\varepsilon_2 = \varepsilon_0\varepsilon_{r2} + i\sigma/\omega \approx i\sigma/\omega$ and $\hat{\mathbf{n}}\bullet\mathbf{E}_2 = \hat{\mathbf{n}}\bullet(\varepsilon_1\mathbf{E}_1/\varepsilon_2) << 1$, because of high conductivity and low frequency. The approximation also means that in the normal range of frequencies of eddy current testing, displacement currents in metal test pieces are negligible compared with conduction currents.

At the interface between region 1 and region 2, $\hat{\mathbf{n}}\bullet\mathbf{B}_1 = \hat{\mathbf{n}}\bullet\mathbf{B}_2 \Leftrightarrow \hat{\mathbf{n}}\bullet\mu_1\mathbf{H}_1 = \hat{\mathbf{n}}\bullet\mu_2\mathbf{H}_2$. If the region 1 is defined as free space, the Green function can be simplified as a static case:

$$G_1(\mathbf{r},\mathbf{r}') = e^{i\sqrt{k_0^2 + i\omega\mu_0\sigma}|\mathbf{r}-\mathbf{r}'|}\Big/(4\pi|\mathbf{r}-\mathbf{r}'|) = e^{ik_0|\mathbf{r}-\mathbf{r}'|}\Big/(4\pi|\mathbf{r}-\mathbf{r}'|) \approx 1/(4\pi|\mathbf{r}-\mathbf{r}'|) \tag{4.17}$$

4.1.3 Integral Equation Normalization

To make the equations more compact, we introduce equivalent surface currents $\bar{\mathbf{J}}_S(\mathbf{r}) = \hat{\mathbf{n}}\times\bar{\mathbf{H}}(\mathbf{r})$, $\mathbf{M}_S(\mathbf{r}) = \mathbf{E}(\mathbf{r})\times\hat{\mathbf{n}}$, with $\bar{\mathbf{H}}(\mathbf{r}) = \eta_1\mathbf{H}(\mathbf{r}) = \sqrt{\mu_1/\varepsilon_1}\,\mathbf{H}(\mathbf{r})$. Additionally, Equations (4.14) and (4.16) are multiplied by $\eta_1 = \sqrt{\mu_1/\varepsilon_1}$ to balance the MoM matrix; therefore, the three chosen Stratton-Chu equations can be written as:

$$\eta_1\mathbf{H}_1(\mathbf{r}) \approx \eta_1\mathbf{H}^{inc}(\mathbf{r}) + \int_S \left[-\frac{1}{\sqrt{\mu_1\varepsilon_1}}\nabla G_1(\mathbf{r},\mathbf{r}')(\hat{\mathbf{n}}\bullet\mathbf{B}(\mathbf{r}')) + \nabla G_1(\mathbf{r},\mathbf{r}')\times\bar{\mathbf{J}}_S(\mathbf{r}')\right] dS' \tag{4.18}$$

$$\mathbf{E}_2(\mathbf{r}) \approx -\int_S \left[i\frac{k_2\eta_2}{\eta_1} G_2(\mathbf{r},\mathbf{r}')(\bar{\mathbf{J}}_S(\mathbf{r}')) - \nabla G_2(\mathbf{r},\mathbf{r}')\times \mathbf{M}_S(\mathbf{r}') \right] dS' \tag{4.19}$$

$$\eta_1\mathbf{H}_2(\mathbf{r}) = \int_S \left[-i\frac{k_1\varepsilon_2}{\varepsilon_1} G_2(\mathbf{r},\mathbf{r}')\mathbf{M}_S(\mathbf{r}') + \frac{\eta_1}{\mu_2}\nabla G_2(\mathbf{r},\mathbf{r}')(\hat{\mathbf{n}}\bullet\mathbf{B}(\mathbf{r}')) - \nabla G_2(\mathbf{r},\mathbf{r}')\times \bar{\mathbf{J}}_S(\mathbf{r}') \right] dS' \tag{4.20}$$

Letting the observation point $\mathbf{r}$ approach surface S and then taking the cross product of equation (4.18) and (4.19) and the dot product of equation (4.20) with $\hat{\mathbf{n}}$ yields:

$$\frac{1}{2}\bar{\mathbf{J}}_S(\mathbf{r}) + \hat{\mathbf{n}}\times\mathbf{R}_1(\tilde{B}_n) - \hat{\mathbf{n}}\times\mathbf{K}_1(\bar{\mathbf{J}}_S) \approx \hat{\mathbf{n}}\times\eta_1\mathbf{H}^{inc}(\mathbf{r}) \tag{4.21}$$

$$\frac{1}{2}\mathbf{M}_S(\mathbf{r}) - ik_1\frac{\mu_2}{\mu_1}\hat{\mathbf{n}}\times\mathbf{L}_2(\bar{\mathbf{J}}_S) + \hat{\mathbf{n}}\times\mathbf{K}_2(\mathbf{M}_S) \approx 0 \tag{4.22}$$

$$\frac{1}{2}\tilde{B}_n + ik_1\frac{\varepsilon_2\mu_2}{\varepsilon_1\mu_1}\hat{\mathbf{n}}\bullet\mathbf{L}_2(\mathbf{M}_S) + \frac{\mu_2}{\mu_1}\hat{\mathbf{n}}\bullet\mathbf{K}_2(\bar{\mathbf{J}}_S) - \hat{\mathbf{n}}\bullet\mathbf{R}_2(\tilde{B}_n) = 0 \tag{4.23}$$

where $\tilde{B}_n$ is defined as $\tilde{B}_n = \hat{\mathbf{n}}\bullet\mathbf{B}(\mathbf{r})\big/\sqrt{\mu_1\varepsilon_1}$ and the operators $\mathbf{L}$, $\mathbf{K}$, and $\mathbf{R}$ are defined as follows:

$$\mathbf{L}_j(\mathbf{X}) = \int_S \left[G_j(\mathbf{r},\mathbf{r}')\mathbf{X}(\mathbf{r}') \right] dS' \tag{4.24}$$

$$\mathbf{K}_j(\mathbf{X}) = P.V.\int_S \nabla G_j(\mathbf{r},\mathbf{r}')\times\mathbf{X}(\mathbf{r}')dS' \tag{4.25}$$

$$\mathbf{R}_j(\mathbf{X}) = P.V.\int_S \nabla G_j(\mathbf{r},\mathbf{r}')(\hat{\mathbf{n}}'\bullet\mathbf{X}(\mathbf{r}'))dS' = P.V.\int_S \nabla G_j(\mathbf{r},\mathbf{r}')X_n(\mathbf{r}')dS' \tag{4.26}$$

4.2 MoM Implementation

Firstly, using RWG basis of $\mathbf{\Lambda}_n(\mathbf{r})$, which is curl-free and divergence-conforming, the induced currents are expanded as:

$$\bar{\mathbf{J}}_S(\mathbf{r}) = \sum_{n=1}^{N_e} a_n\mathbf{\Lambda}_n(\mathbf{r}), \quad \mathbf{M}_S(\mathbf{r}) = \sum_{n=1}^{N_e} c_n\mathbf{\Lambda}_n(\mathbf{r}) \tag{4.27}$$

where N_e is the total edge number. The structure of RWG basis function has been discussed in section 2.4 and is similar to a roof-top basis function and its value comes from the fact that it eliminates line charges at edges. Using pulse basis $b_n(\mathbf{r})$ for triangular mesh T_n, the normal component of magnetic field is expanded as:

$$\tilde{B}_n = \hat{\mathbf{n}} \bullet \mathbf{B}(\mathbf{r}) \Big/ \sqrt{\mu_1 \varepsilon_1} = B_n \Big/ \sqrt{\mu_1 \varepsilon_1} = \sum_{n=1}^{N_p} d_n b_n(\mathbf{r}) \tag{4.28}$$

where $b_n(\mathbf{r}) = \begin{cases} 1 & \mathbf{r} \in T_n \\ 0 & \text{otherwise} \end{cases}$ and N_p is the total patch number.

Secondly, using Galerkin's method, equations (4.21) and (4.22) can be tested with $\mathbf{\Lambda}_m(\mathbf{r})$ and equation (4.23) tested with $b_m(\mathbf{r})$. Then, discretized matrix equations are formed by means of numerical integration rule, $\frac{1}{T}\int_T dS\, f(\mathbf{r}) = \sum_{g=1}^{N_g} W_g f(\mathbf{r}_g)$, in which N_g is the total number of integral points in the patch.

Finally, the discretized MoM matrix of the Stratton-Chu formulas reads

$$\begin{bmatrix} \frac{1}{2}\mathbf{T} - \mathbf{K}_1^{\times} & 0 & \mathbf{R}_1^{\times} \\ -ik_1 \frac{\mu_2}{\mu_1}\mathbf{L}_2^{\times} & \frac{1}{2}\mathbf{T} + \mathbf{K}_2^{\times} & 0 \\ \frac{\mu_2}{\mu_1}\mathbf{K}_2^{n} & ik_1 \frac{\varepsilon_2 \mu_2}{\varepsilon_1 \mu_1}\mathbf{L}_2^{n} & \frac{1}{2}\mathbf{D} - \mathbf{R}_2^{n} \end{bmatrix} \begin{bmatrix} \mathbf{a} \\ \mathbf{c} \\ \mathbf{d} \end{bmatrix} = \begin{bmatrix} \mathbf{V}^I \\ 0 \\ 0 \end{bmatrix}$$

If further rescaling the discretized MoM matrix with a setting of $\mathbf{c}' \equiv \mathbf{c} / k_1$, it gives

$$\begin{bmatrix} \frac{1}{2}\mathbf{T}-\mathbf{K}_1^{\times} & 0 & \mathbf{R}_1^{\times} \\ -i\frac{\mu_2}{\mu_1}\mathbf{L}_2^{\times} & \frac{1}{2}\mathbf{T}+\mathbf{K}_2^{\times} & 0 \\ \frac{\mu_2}{\mu_1}\mathbf{K}_2^{n} & ik_2^2\mathbf{L}_2^{n} & \frac{1}{2}\mathbf{D}-\mathbf{R}_2^{n} \end{bmatrix} \begin{bmatrix} \mathbf{a} \\ \mathbf{c}' \\ \mathbf{d} \end{bmatrix} = \begin{bmatrix} \mathbf{V}^I \\ 0 \\ 0 \end{bmatrix}$$

where the subscript $j=1,2$ stand for medium 1 or medium 2, and the superscript $\times$ and n denote the cross or dot products with normal component $\hat{\mathbf{n}}$.

Furthermore, the expanding terms in the MoM matrix are detailed in the form as follows:

$$T_{mn} = \int_{S_m} dS\ \mathbf{\Lambda}_m(\mathbf{r})\bullet\mathbf{\Lambda}_n(\mathbf{r}) = \frac{l_m}{2S_m^+}\int_{S_m^+} dS\ \boldsymbol{\rho}_m^+\bullet\mathbf{\Lambda}_n(\mathbf{r}) + \frac{l_m}{2S_m^-}\int_{S_m^-} dS\ \boldsymbol{\rho}_m^-\bullet\mathbf{\Lambda}_n(\mathbf{r})$$
$$= I_0(m^+,n) + I_0(m^-,n)$$

$$\text{with}\quad I_0(m^+,n) = \begin{cases} \frac{l_m l_n}{4S_n^+}\sum_{g=1}^{N_g} W_g(S_m^+)(\mathbf{r}_{g/m}^+ - \mathbf{r}_{m3})\bullet(\mathbf{r}_{g/m}^+ - \mathbf{r}_{n3}), & \mathbf{r}_{g/m}^+ \in S_n^+ \\ \frac{l_m l_n}{4S_n^-}\sum_{g=1}^{N_g} W_g(S_m^+)(\mathbf{r}_{g/m}^+ - \mathbf{r}_{m3})\bullet(-\mathbf{r}_{g/m}^+ + \mathbf{r}_{n4}), & \mathbf{r}_{g/m}^+ \in S_n^- \\ 0 & \mathbf{r}_{g/m}^+ \notin S_n \end{cases}$$

$$I_0(m^-,n) = \begin{cases} \frac{l_m l_n}{4S_n^+}\sum_{g=1}^{N_g} W_g(S_m^-)(\mathbf{r}_{m4} - \mathbf{r}_{g/m}^-)\bullet(\mathbf{r}_{g/m}^- - \mathbf{r}_{n3}), & \mathbf{r}_{g/m}^- \in S_n^+ \\ \frac{l_m l_n}{4S_n^-}\sum_{g=1}^{N_g} W_g(S_m^-)(\mathbf{r}_{m4} - \mathbf{r}_{g/m}^-)\bullet(-\mathbf{r}_{g/m}^- + \mathbf{r}_{n4}), & \mathbf{r}_{g/m}^- \in S_n^- \\ 0 & \mathbf{r}_{g/m}^- \notin S_n \end{cases}$$

$$D_{mn} = \int_{T_m} dS\ b_m(\mathbf{r})b_n(\mathbf{r}) = \delta_{mn}\int_{T_m} dS = \delta_{mn}T_m$$

$$K^{\times}_{jmn} = \int_{S_m} dS \left[\boldsymbol{\Lambda}_m(\mathbf{r})\times\hat{\mathbf{n}}\right]\bullet\int_{S_n}\nabla G_j(\mathbf{r},\mathbf{r}')\times\boldsymbol{\Lambda}_n(\mathbf{r}')dS'$$
$$= \sum_{p=1}^{2}\sum_{g=1}^{N_g} W_g(S_m^p)S_m^p\left[\boldsymbol{\Lambda}_m(\mathbf{r}_{g/m})\times\hat{\mathbf{n}}\right]\bullet\sum_{q=1}^{2}\sum_{g=1}^{N_g} W_g(S_n^q)S_n^q\nabla G_j(\mathbf{r}_{g/m},\mathbf{r}'_{g/n})\times\boldsymbol{\Lambda}_n(\mathbf{r}'_{g/n})$$

$$K^{n}_{jmn} = \int_{T_m} dS\, b_m(\mathbf{r})\,\hat{\mathbf{n}}\bullet\int_{S_n}\nabla G_j(\mathbf{r},\mathbf{r}')\times\boldsymbol{\Lambda}_n(\mathbf{r}')dS'$$
$$= T_m\sum_{g=1}^{N_g} W_g(T_m)\,\hat{\mathbf{n}}\bullet\sum_{q=1}^{2}\sum_{g=1}^{N_g} W_g(S_n^q)S_n^q\nabla G_j(\mathbf{r}_{g/m},\mathbf{r}'_{g/n})\times\boldsymbol{\Lambda}_n(\mathbf{r}'_{g/n}) \qquad \mathbf{r}_{g/m}\in T_m$$

$$L^{\times}_{jmn} = \int_{S_m} dS \left[\boldsymbol{\Lambda}_m(\mathbf{r})\times\hat{\mathbf{n}}\right]\bullet\int_{S_n} G_j(\mathbf{r},\mathbf{r}')\boldsymbol{\Lambda}_n(\mathbf{r}')dS'$$
$$= \sum_{p=1}^{2}\sum_{g=1}^{N_g} W_g(S_m^p)S_m^p\left[\boldsymbol{\Lambda}_m(\mathbf{r}_{g/m})\times\hat{\mathbf{n}}\right]\bullet\sum_{q=1}^{2}\sum_{g=1}^{N_g} W_g(S_n^q)S_n^q G_j(\mathbf{r}_{g/m},\mathbf{r}'_{g/n})\boldsymbol{\Lambda}_n(\mathbf{r}'_{g/n})$$

$$L^{n}_{jmn} = \int_{T_m} dS\, b_m(\mathbf{r})\,\hat{\mathbf{n}}\bullet\int_{S_n} G_j(\mathbf{r},\mathbf{r}')\boldsymbol{\Lambda}_n(\mathbf{r}')dS'$$
$$= T_m\sum_{g=1}^{N_g} W_g(T_m)\,\hat{\mathbf{n}}\bullet\sum_{q=1}^{2}\sum_{g=1}^{N_g} W_g(S_n^q)S_n^q G_j(\mathbf{r}_{g/m},\mathbf{r}'_{g/n})\boldsymbol{\Lambda}_n(\mathbf{r}'_{g/n}) \qquad \mathbf{r}_{g/m}\in T_m$$

$$R^{\times}_{jmn} = \int_{S_m} dS \left[\boldsymbol{\Lambda}_m(\mathbf{r})\times\hat{\mathbf{n}}\right]\bullet\int_{T_n}\nabla G_j(\mathbf{r},\mathbf{r}')b_n(\mathbf{r}')dS'$$
$$= \sum_{p=1}^{2}\sum_{g=1}^{N_g} W_g(S_m^p)S_m^p\left[\boldsymbol{\Lambda}_m(\mathbf{r}_{g/m})\times\hat{\mathbf{n}}\right]\bullet T_n\sum_{g=1}^{N_g} W_g(T_n)\nabla G_j(\mathbf{r}_{g/m},\mathbf{r}'_{g/n}) \qquad \mathbf{r}'_{g/n}\in T_n$$

$$R^{n}_{jmn} = \int_{T_m} dS\, b_m(\mathbf{r})\,\hat{\mathbf{n}}\bullet\int_{T_n}\nabla G_j(\mathbf{r},\mathbf{r}')b_n(\mathbf{r}')dS'$$
$$= T_m\sum_{g=1}^{N_g} W_g(T_m)\,\hat{\mathbf{n}}\bullet T_n\sum_{g=1}^{N_g} W_g(T_n)\nabla G_j(\mathbf{r}_{g/m},\mathbf{r}'_{g/n}) \qquad \mathbf{r}_{g/m}\in T_m,\quad \mathbf{r}'_{g/n}\in T_n$$

$$V^{I}_{m} = \eta_1\int_{S_m} dS\ \boldsymbol{\Lambda}_m(\mathbf{r})\bullet\left[\hat{\mathbf{n}}\times\mathbf{H}^{inc}(\mathbf{r})\right]$$
$$= \eta_1\frac{l_m}{2}\sum_{p=1}^{2}\sum_{g=1}^{N_g} W_g(S_m^p)\left\{\boldsymbol{\rho}_m^{\pm}\bullet\left[\hat{\mathbf{n}}\times\mathbf{H}^{inc}(\mathbf{r}_g)\right]\right\}$$

To calculate the expanding terms containing the Green's function G_j or ∇G_j in the MoM matrix, that is, $K^{\times}_{jmn}$, K^{n}_{jmn}, $L^{\times}_{jmn}$, L^{n}_{jmn}, $R^{\times}_{jmn}$, and R^{n}_{jmn}, we need to apply

singularity or near singularity extractions, if the field point is right on or close to the source patch. The singular integration procedure is elaborated by Graglia [48], and we use the same procedure to remove singularity in the expanding terms.

CHAPTER 5. NUBERICAL STUDY FOR THREE DIMENSIONAL EDDY CURRENT NONDESTRUCTIVE EVALUATION

In what follows, we present numerical results for the eddy current NDE in three dimensions after the implementation of the Stratton-Chu formulation for the conductive medium [49]. These numerical results include near field distribution and impedance change. Additionally, we introduce Auld's impedance formulas for the calculation of impedance variation.

5.1 Near Field Distribution

The traditional approach to probe The three-dimensional Stratton-Chu formulas for the conductive medium are solved numerically by means of the BIE method. Firstly, as an illustration of the method, a conducting sphere model is chosen as an example of the eddy current problem. The sphere with a radius of 1 meter is represented by 3200 flat triangles and 4800 edges, and the average edge length is around 0.097 meter. The scattered electric and magnetic fields are calculated using the following equations:

$$\mathbf{E} = \frac{i}{4\pi\omega\varepsilon}\iint_S \left[(\mathbf{J}_s \cdot \nabla)\nabla + k_1^2 \mathbf{J}_s + i\varepsilon\omega \mathbf{M}_s \times \nabla \right] \frac{e^{ik_1|\mathbf{r}-\mathbf{r}'|}}{|\mathbf{r}-\mathbf{r}'|} ds' \tag{5.1}$$

$$\mathbf{H} = \frac{i}{4\pi\omega\mu}\iint_S \left[(\mathbf{M}_s \cdot \nabla)\nabla + k_1^2 \mathbf{M}_s - i\mu\omega \mathbf{J}_s \times \nabla \right] \frac{e^{ik_i|\mathbf{r}-\mathbf{r}'|}}{|\mathbf{r}-\mathbf{r}'|} ds' \tag{5.2}$$

For a plane wave incident from the direction of $(\theta_i = 0, \varphi_i = 0)$ and polarized in the horizontal or vertical direction [41], the computation results of scattered electric fields are shown in Figure 5.1, as the observation surface is 0.1 meter outside the sphere surface. In this

case, the working frequency is 3 MHz and the conductivity of the sphere is 5×10^7 S/m. The computation results agree well with the Mie series solution [50] at plane wave incidence.

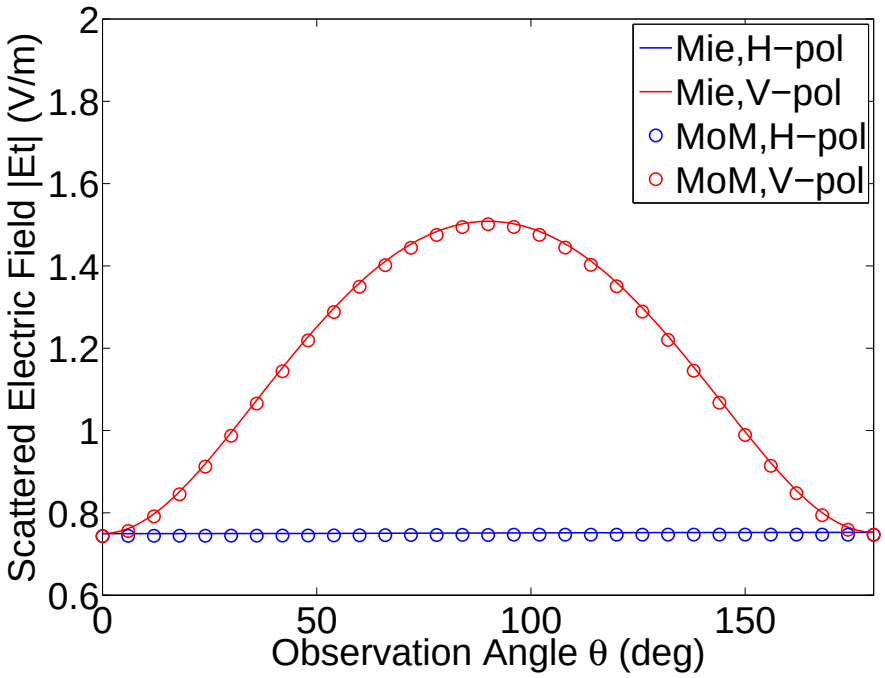

Figure 5.1. Comparison of scattered electric fields calculated by BIE method and those from Mie series solution for a conducting sphere with plane wave incidence. H-pol: horizontal polarization; V-pol: vertical polarization.

To simulate air core coils in the probe field modeling, a small electric current loop is put at the z-axis, with the coordinate of (0.0, 0.0, 1.2 meter) and its loop surface parallel to the x-y plane. The electric current loop can be treated as a magnetic dipole with a moment of $M = SI_0$:

$$I_m l = -i\omega\mu_0 M = -i\pi a^2 \omega\mu_0 I_0$$

The computation results of scattered electric and magnetic fields are shown in Figure 5.2, as the observation surface is 0.1 meter outside the sphere surface, with the frequency of 3

MHz and the sphere conductivity of 5×10^3 S/m. The solution of scattered electric and magnetic fields reasonably agree with the Mie series solution with localized magnetic dipole incidence.

Next, a cube model with the conductivity of 5×10^3 S/m is set as another example of the eddy current problem. The cube with a side length of 1 meter is represented by 1200 flat triangles and 1800 edges, and the average edge length is around 0.11 meter. The center of the cube is at the origin (0.0, 0.0, 0.0) and the magnetic dipole is put above the top surface of the cube at $z = 0.7$ meter plane, as shown in Figure 5.3.

Figure 5.4 shows the snapshots of total time-harmonic electric field pattern at a 2 meter by 2 meter square in $z = 0.6$ meter plane, as the magnetic dipole at a excitation frequency of 3 MHz moves towards a corner of the cube, as shown in Figure 5.3, which stands for a top surface scanning for the cube with a lift-off distance of 0.2 meter. We present the vector plot of the in-phase components (denoted as $t = 0$) and the quadrature components ($t = T/4$, where T is the period of the incident wave) separately. Each arrow in the figure is drawn from the point at which the electric field is evaluated, with length proportional to the magnitude of the vector at that point. These computation results have reasonable physical meanings for the primary eddy current field produced by sinusoidal excitation of a small induction coil in the cube model.

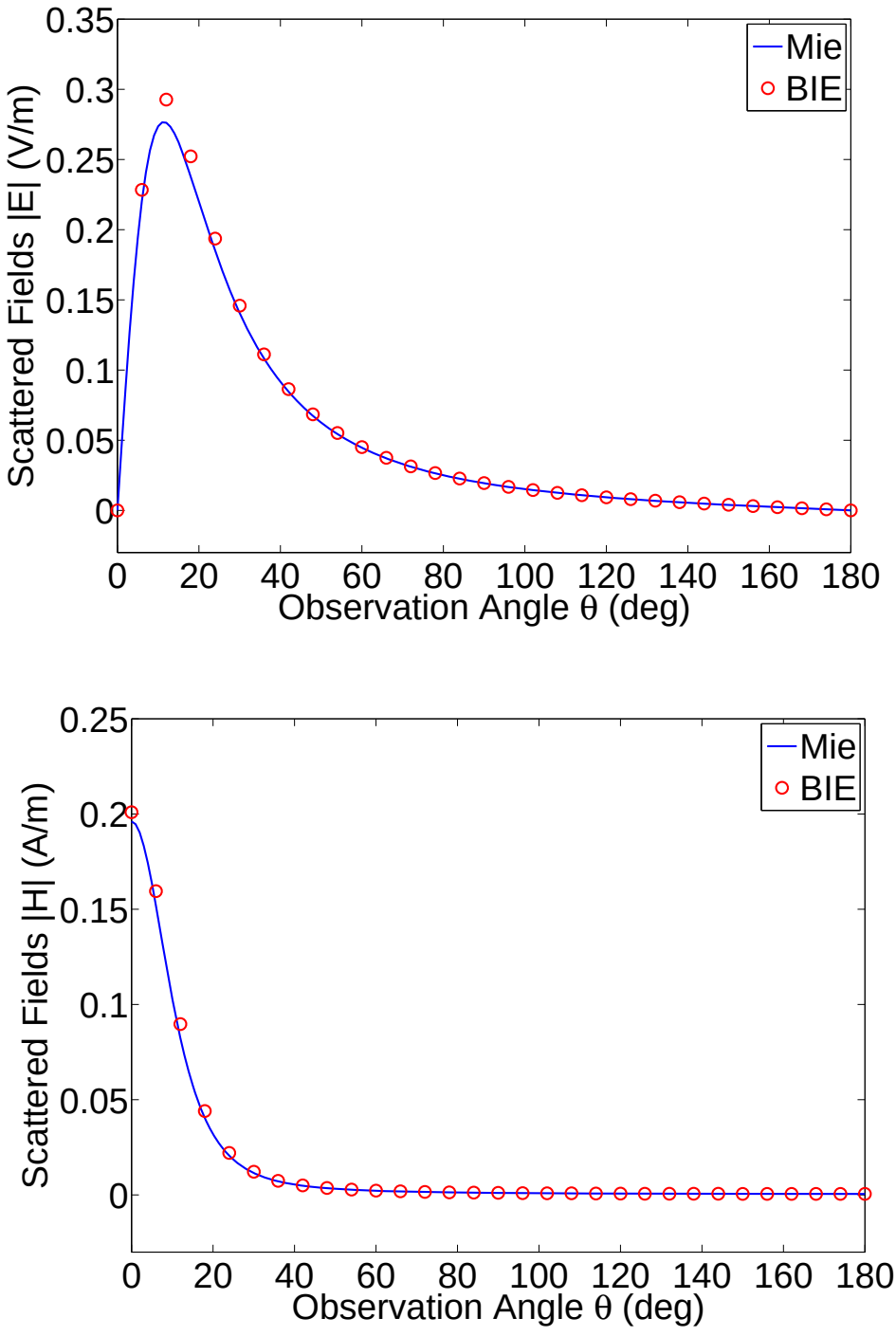

Figure 5.2. Comparison of scattered electric and magnetic fields calculated by BIE method and those from Mie series solution for a conducting sphere with localized magnetic dipole incidence.

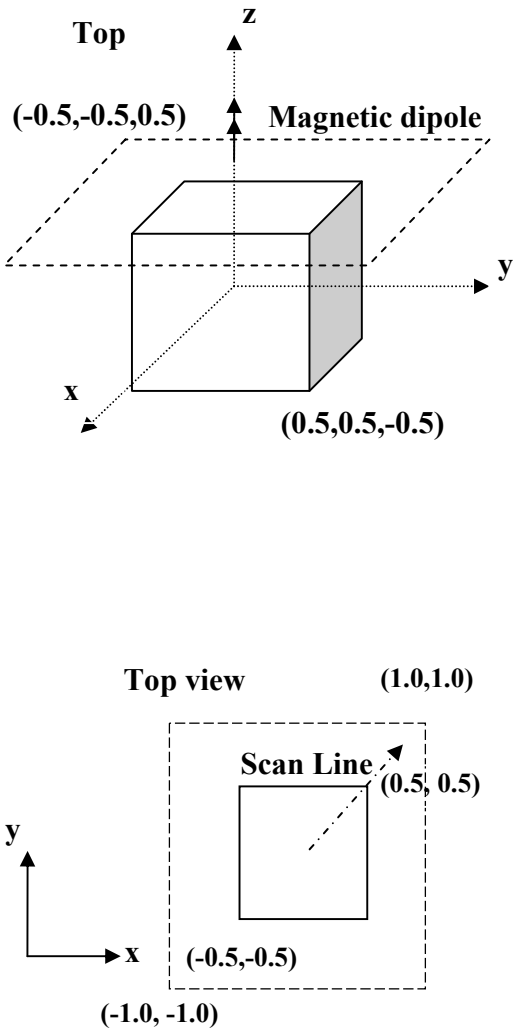

Figure 5.3. A conducting cube model and its top surface scanning diagram.

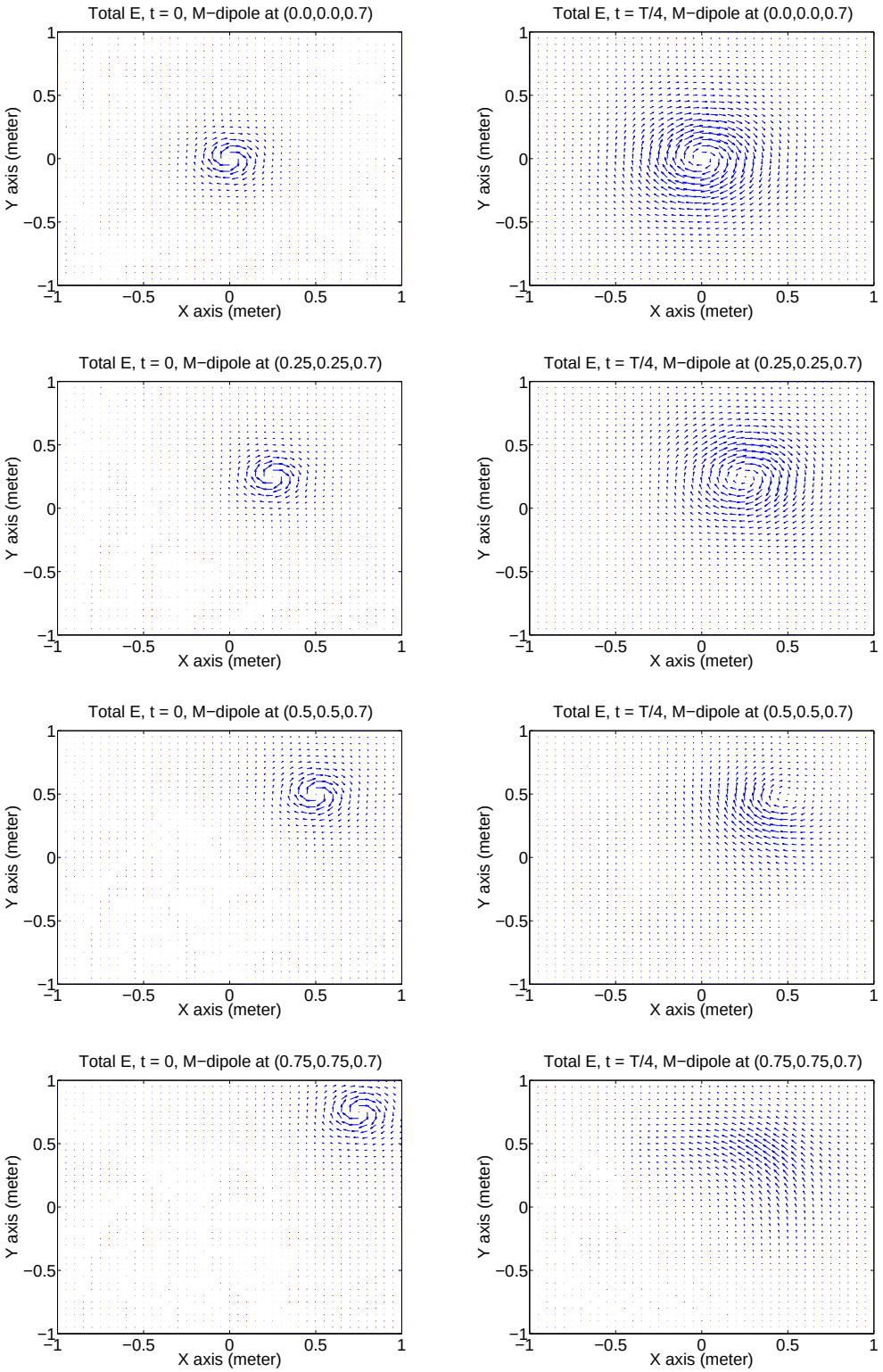

Figure 5.4. Snapshots of total time-harmonic electric field pattern at a 2 meter by 2 meter square in z=0.6 meter plane, as the magnetic dipole moves towards a corner of the cube. The labels $t = 0$ and $t = T/4$ stand for the in-phase and quadrature components, respectively.

5.2 Impedance Change

5.2.1 Auld's Impedance Formulas

The traditional approach to probe modeling used an equivalent circuit model to provide a description of probe performance qualitatively [1]. Later, Burrows developed a quantitative equivalent circuit model, for defects that consist of small ellipsoidal inclusions and voids [6]. His approach was to generate the probe modeling based on the concepts of microwave circuit theory, specifically, use of the electromagnetic field reciprocity relation to establish a circuit reciprocity relation for two-port probes. After that, researchers continued working on the quantitative probe modeling, generalized Burrows's work and defined the electromagnetic boundary value problems that must be solved to evaluate impedance change ΔZ. In 1999, Auld and Moulder summarized all the advancements in EC modeling by then and presented a comprehensive review in [51], which includes the derivation of impedance formulas as follows:

In surface integral form,

$$\Delta Z = Z - Z_0 = \frac{1}{I^2}\int_S dS\ \hat{\mathbf{n}}\bullet\left[\mathbf{E}\times\mathbf{H}' - \mathbf{E}'\times\mathbf{H}\right] \tag{5.3}$$

In volume integral form,

$$\Delta Z = Z - Z_0 = \frac{-1}{I^2}\int_V dV\left[\Delta\sigma\left(\mathbf{E}\bullet\mathbf{E}'\right) + i\omega\Delta\mu\left(\mathbf{H}\bullet\mathbf{H}'\right)\right] \tag{5.4}$$

where Z is the impedance of the coil in the presence of the flawed conductor and Z_0 is the coil impedance in the presence of a similar but unflawed conductor. As shown in Figure 5.5, $\mathbf{E}$ and $\mathbf{H}$ are the probe fields excited in the unflawed conductor by the probe terminal current I, and $\mathbf{E}'$ and $\mathbf{H}'$ are the probe fields excited in the presence of a defect by the same probe

terminal current; V is the volume of defect and S is any surface enclosing the defect; $\hat{\mathbf{n}}$ is an inward pointing unit vector normal to the surface S; $\Delta\sigma$ and $\Delta\mu$ are the difference of conductivity and permeability between the flawed and the unflawed states of the test piece. The surface integral form of Auld's Formula can be conveniently transformed into volume integral form by using the divergence theorem and Maxwell's equations [51].

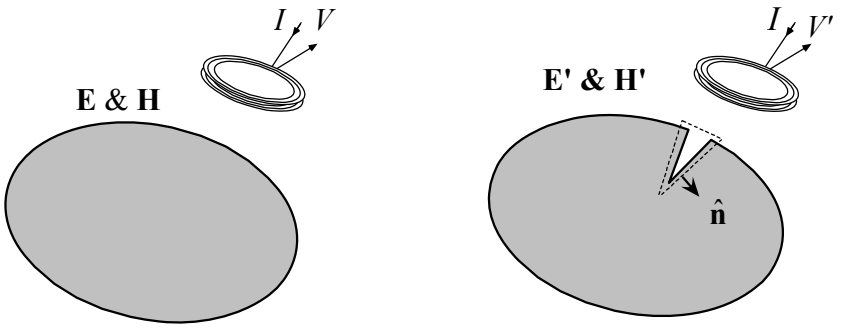

Figure 5.5. Geometry of general absolute probe interacted with unflawed and flawed conductors. Left: unflawed conductor; Right: flawed conductor.

In our research, we focus on the surface integral equations for homogenous conductive medium with a closed surface in eddy current NDE. The integral surface S is any surface enclosing the unflawed conductor or flawed conductor. The impedance change in the presence of conductor (unflawed or flawed) is directly calculated corresponding to the isolated probe coil. The impedance variation due to a defect is the difference between the impedance changes of unflawed and flawed cases. As a result, we simplify the Auld's formula in surface integral form, if only equivalent surface currents $\mathbf{J}_s$ and $\mathbf{M}_s$ exist in the conductor,

$$\begin{aligned}\Delta Z &= \frac{1}{I^2}\int_S dS\ \hat{\mathbf{n}}\bullet\left[\mathbf{E}^{inc}\times\mathbf{H}-\mathbf{E}\times\mathbf{H}^{inc}\right] = \frac{1}{I^2}\iiint_V\left[\mathbf{H}^{inc}\bullet\mathbf{M}-\mathbf{E}^{inc}\bullet\mathbf{J}\right]dV \\ &= \frac{1}{I^2}\int_S dS\ \hat{\mathbf{n}}\bullet\left[\mathbf{H}^{inc}\bullet\mathbf{M}_s-\mathbf{E}^{inc}\bullet\mathbf{J}_s\right]\end{aligned} \tag{5.5}$$

where $\mathbf{E}^{inc}$ and $\mathbf{M}^{inc}$ are the incident probe fields and **E** and **H** are the probe fields excited in the unflawed or flawed conductors. Also, V is the volume of the testing conductor and S is any surface enclosing the conductor.

5.2.2 Coil above a Sphere

In this section, we investigate impedance change in a single-turn coil situated above a conducting sphere numerically, which has been compared to an analytical solution [52], to verify our numerical codes based on the three-dimensional Stratton-Chu formulas. Firstly, as an illustration, a conducting sphere model is also chosen as an example of the eddy current problem. We consider a single-turn circular coil of radius r_c whose axis goes through the centre of a sphere of radius ρ_1 and conductivity σ, where h stands for the lift-off distance and ρ_c stands for the distance between origin of the sphere and the edge of the coil, as shown in Figure 5.6. The sphere is represented numerically by 3200 flat triangles and 4800 edges.

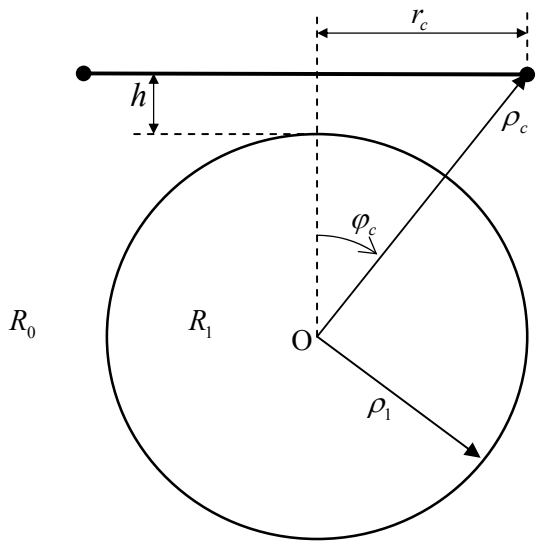

Figure 5.6. Cross-section for a single-turn coil of a radius of r_c above a sphere of radius ρ_1.

As presented by Antimirov *et al.* in [52], the change in impedance of this case has an analytical form:

$$Z^{ind} = \pi\omega\mu_0(\rho_1^2 / r_c)\sin^2(\varphi_c)Z\,,$$

where

$$Z = -i\sum_{n=1}^{\infty}\frac{1}{n(n+1)}\left(\frac{\rho_1}{\rho_c}\right)^{2n-1}\left[P_n^{(1)}(\cos\varphi_c)\right]^2 \left\{\frac{(2n+1)\mu_1 J_{n+1/2}(k\rho_1)}{[\mu_1(n+1)-0.5]J_{n+1/2}(k\rho_1)+(k\rho_1)J'_{n+1/2}(k\rho_1)}-1\right\} \tag{5.6}$$

And it is known that $k=\sqrt{i\omega\sigma\mu_0\mu_1}=\frac{1+i}{\delta}$ and $\beta=r_c\sqrt{\omega\sigma\mu_0\mu_1}=\frac{\sqrt{2}r_c}{\delta}$.

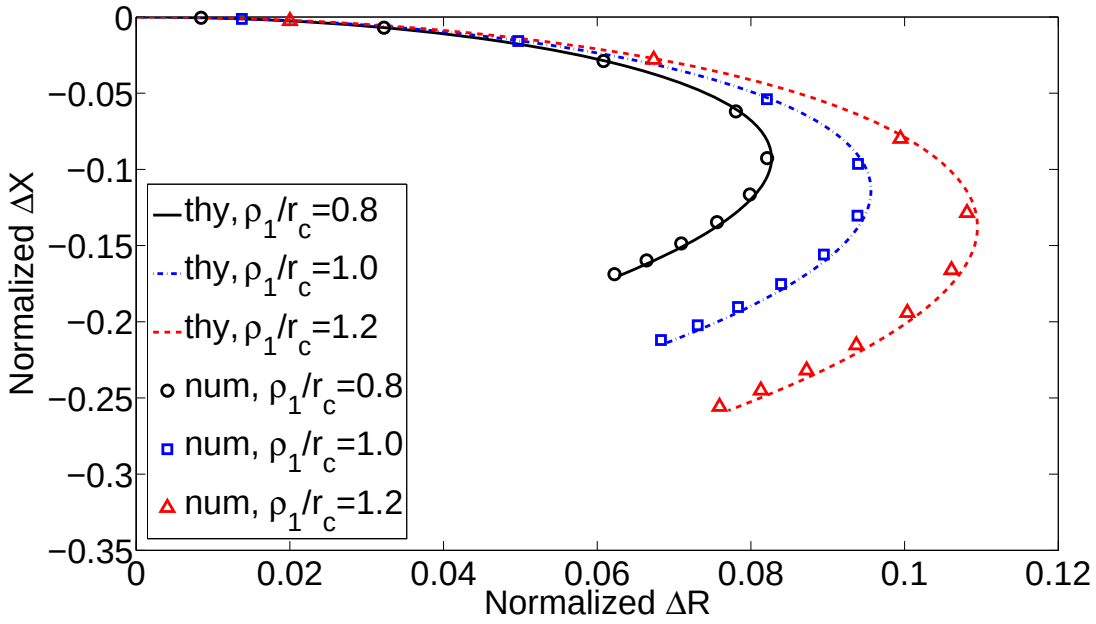

Figure 5.7. Comparison of theoretical and numerical results in impedance change against β for three values of ρ_1 / r_c with $h / r_c = 0.1$ and $\mu_1 = 1$.

The normalized impedance change, $Z = R - iX$, is computed analytically for different values of β, ρ_1 / r_c, h / r_c. Meanwhile, the numerical results are computed using our codes for the same setting, with incident electric and magnetic fields by a single-turn coil represented in [53].

Then, the two groups of results are presented together in Figures 5.7 and 5.8 for comparison. The points on the curves in the figures correspond to $\beta = 1,...,10$, where the lowest point on each curve corresponds to $\beta = 10$. It is easily concluded that the numerical results agree well with analytical results and our numerical codes based on the three-dimensional Stratton-Chu formulas succeed in this case.

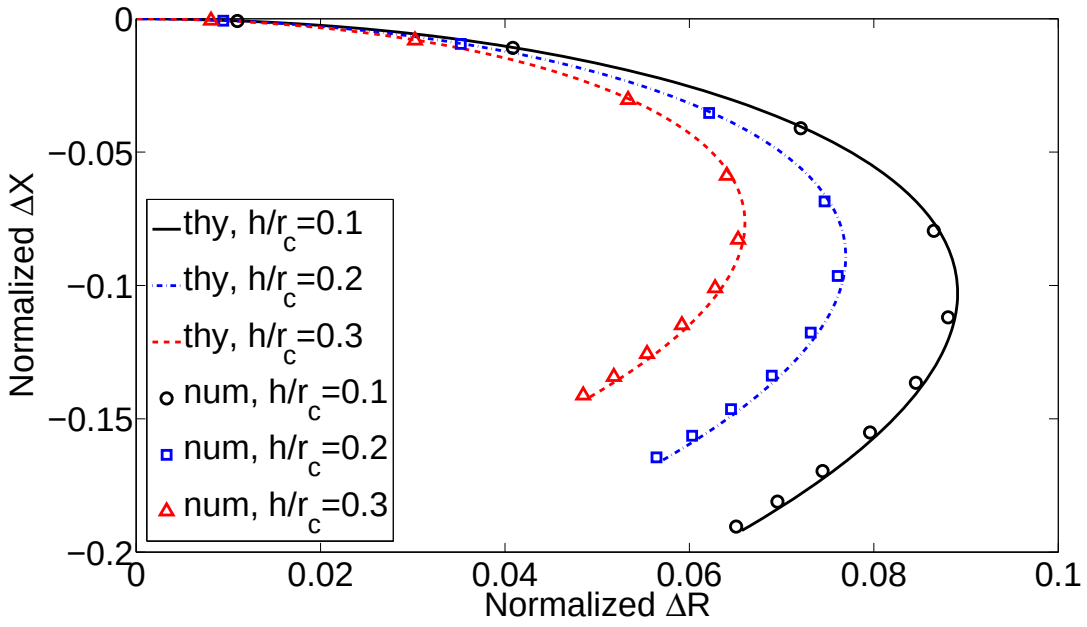

Figure 5.8. Comparison of theoretical and numerical results in impedance change against β for three values of h / r_c with $\rho_1 / r_c = 0.9$ and $\mu_1 = 1$.

5.2.3 Coil above a Wedge

Included in this section is the numerical output of impedance change for a finite cross-section coil interacted with a right-angled conductive wedge, which is compared to analytical results and experimental results in [54, 55]. Before that, in what follows, the incident electric and magnetic fields from a coil with finite cross-section is elaborated in details.

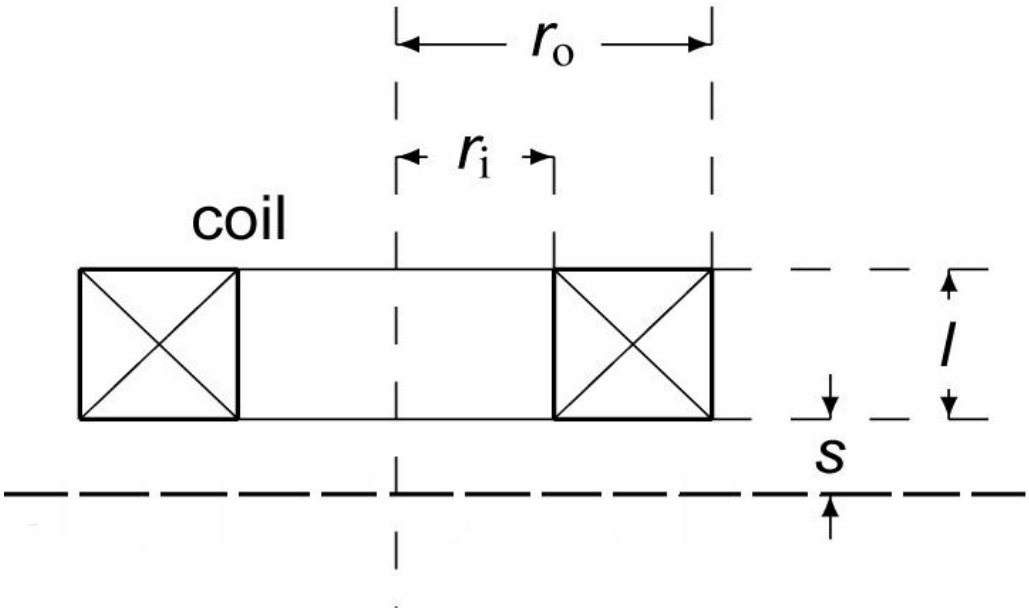

Figure 5.9. Cross-section diagram through the axis of a circular, air-cored, eddy-current coil, positioned horizontally.

For an n-turn coil with rectangular cross-section and parameters as shown in Figure 5.9, the electric field has a form [54]

$$\mathbf{E}^n(\rho,z) = \int_{\substack{\text{coil cross}\\ \text{section}}} \mathbf{E}(\rho,z,a_s,h_s)\,dS = \int_{r_i}^{r_o}\int_{s}^{s+l} \mathbf{E}(\rho,z,a_s,h_s)\,da_s dh_s \tag{5.7}$$

where $\mathbf{E}(\rho, z, a_s, h_s)$ is the electric field produced by the equivalent current density $\mathbf{J}_s$ in the coil under quasi-static condition and the subscript 's' refers to this as being the source current density. a_s and h_s are, then, continuous variables in the radial and vertical directions, respectively.

As an example of applying the process of linear superposition consider the electric field in the region above the coil. This corresponds to region 1 in the case of the circular current loop treated in [54]. Taking the result for $E_\phi^1(\rho, z)$ in the case of the δ-function coil, removing the term related to conductive half plane and inserting that into equation (5.7) gives

$$\mathbf{E} = \hat{\phi}\, E_\phi^n = \begin{cases} \hat{\phi}\,\dfrac{1}{2} i\omega\mu_0 I_s \displaystyle\int_0^\infty \int_{r_i}^{r_o} \int_s^{s+l} a_s J_1(\kappa a_s) J_1(\kappa\rho) e^{\kappa(h_s - z)}\, d\kappa da_s dh_s & z \geq s+l \\ \hat{\phi}\,\dfrac{1}{2} i\omega\mu_0 I_s \displaystyle\int_0^\infty \int_{r_i}^{r_o} a_s J_1(\kappa a_s) J_1(\kappa\rho) \frac{1}{\kappa}\left(1 - e^{-\kappa l}\right) d\kappa da_s & s \leq z < s+l \\ \hat{\phi}\,\dfrac{1}{2} i\omega\mu_0 I_s \displaystyle\int_0^\infty \int_{r_i}^{r_o} \int_s^{s+l} a_s J_1(\kappa a_s) J_1(\kappa\rho) e^{-\kappa(h_s - z)}\, d\kappa da_s dh_s & z < s \end{cases}$$

$$= \begin{cases} \hat{\phi}\,\dfrac{1}{2} i\omega\mu_0 I_s \displaystyle\int_0^\infty \int_{r_i}^{r_o} a_s J_1(\kappa a_s) J_1(\kappa\rho) \frac{e^{-\kappa(z-s-l)}}{\kappa}\left(1 - e^{-\kappa l}\right) d\kappa da_s & z \geq s+l \\ \hat{\phi}\,\dfrac{1}{2} i\omega\mu_0 I_s \displaystyle\int_0^\infty \int_{r_i}^{r_o} a_s J_1(\kappa a_s) J_1(\kappa\rho) \frac{1}{\kappa}\left(1 - e^{-\kappa l}\right) d\kappa da_s & s \leq z < s+l \\ \hat{\phi}\,\dfrac{1}{2} i\omega\mu_0 I_s \displaystyle\int_0^\infty \int_{r_i}^{r_o} a_s J_1(\kappa a_s) J_1(\kappa\rho) \frac{e^{-\kappa(s-z)}}{\kappa}\left(1 - e^{-\kappa l}\right) d\kappa da_s & z < s \end{cases} \tag{5.8}$$

Assuming that the current in each loop has the same phase and amplitude and the current density is $I_s = nI / \left[l(r_o - r_i)\right]$. Collecting together terms in equation (5.8) that depend on a_s and h_s and then integrating over these variables, gives

$$E_\phi^n = \begin{cases} i\dfrac{\omega\mu_0 In}{2l(r_o-r_i)}\displaystyle\int_0^\infty J_1(\kappa\rho)\chi\left(\kappa r_i,\kappa r_o\right)\frac{e^{-\kappa(z-s-l)}}{\kappa^3}\left(1-e^{-\kappa l}\right)d\kappa & z \ge s+l \\ i\dfrac{\omega\mu_0 In}{2l(r_o-r_i)}\displaystyle\int_0^\infty J_1(\kappa\rho)\chi\left(\kappa r_i,\kappa r_o\right)\frac{1}{\kappa^3}\left(1-e^{-\kappa l}\right)d\kappa & s \le z < s+l \\ i\dfrac{\omega\mu_0 In}{2l(r_o-r_i)}\displaystyle\int_0^\infty J_1(\kappa\rho)\chi\left(\kappa r_i,\kappa r_o\right)\frac{e^{-\kappa(s-z)}}{\kappa^3}\left(1-e^{-\kappa l}\right)d\kappa & z < s \end{cases} \tag{5.9}$$

where $\chi\left(\kappa r_i,\kappa r_o\right)=\displaystyle\int_{\kappa r_i}^{\kappa r_o} xJ_1(x)dx$, which can be expressed in terms of standard functions. For computation purposes, $\chi\left(a_1,a_2\right)$ can be expressed in terms of Struve and Bessel functions [56]. More specifically, it is defined that

$$\begin{aligned}\chi\left(a_1,a_2\right) &= \int_{a_1}^{a_2} rJ_1(r)dr = \int_0^{a_2} rJ_1(r)dr - \int_0^{a_1} rJ_1(r)dr \\ &= \pi^{\frac{1}{2}}\Gamma\left(\frac{3}{2}\right)\left\{a_2\left[J_1(a_2)\mathrm{H}_0(a_2)-\mathrm{H}_1(a_2)J_0(a_2)\right]-a_1\left[J_1(a_1)\mathrm{H}_0(a_1)-\mathrm{H}_1(a_1)J_0(a_1)\right]\right\}\end{aligned}$$

where $J_{i=0,1}$ and $\mathrm{H}_{i=0,1}$ are the zero[th]- and first-order Bessel and Struve functions.

Then, the magnetic field for an *n*-turn coil with rectangular cross-section can be easily derived in the following lines.

Since $\nabla\times\mathbf{E}=i\omega\mu\mathbf{H}$ and $\nabla\times\hat{\phi}E_\phi=-\hat{\rho}\dfrac{\partial E_\phi}{\partial z}+\hat{z}\dfrac{1}{\rho}\dfrac{\partial(\rho E_\phi)}{\partial\rho}$, it is derived that

$$H_\rho = \frac{i}{\omega\mu_0}\frac{\partial E_\phi}{\partial z}$$

$$H_z = \frac{-i}{\omega\mu_0}\frac{1}{\rho}\frac{\partial(\rho E_\phi)}{\partial\rho}$$

For $H_\rho = \dfrac{i}{\omega\mu_0}\dfrac{\partial E_\phi}{\partial z}$, it gives

$$H_\rho = \begin{cases} \dfrac{nI}{2l(r_o-r_i)}\displaystyle\int_0^\infty J_1(\kappa\rho)\chi\left(\kappa r_i,\kappa r_o\right)\frac{e^{-\kappa(z-s-l)}}{\kappa^2}\left(1-e^{-\kappa l}\right)d\kappa & z \ge s+l \\ 0 & s \le z < s+l \\ -\dfrac{nI}{2l(r_o-r_i)}\displaystyle\int_0^\infty J_1(\kappa\rho)\chi\left(\kappa r_i,\kappa r_o\right)\frac{e^{-\kappa(s-z)}}{\kappa^2}\left(1-e^{-\kappa l}\right)d\kappa & z < s \end{cases} \tag{5.10}$$

For $H_z = \dfrac{-i}{\omega\mu_0}\dfrac{1}{\rho}\dfrac{\partial(\rho E_\phi)}{\partial\rho}$,

Since $\dfrac{d}{dx}\left[J_1(\alpha x)\right] = \alpha J_0(\alpha x) - \dfrac{1}{x}J_1(\alpha x)$, it yields

$$\begin{aligned} \frac{d}{d\rho}\left[\rho J_1(\kappa\rho)\right] &= J_1(\kappa\rho) + \rho\frac{d}{d\rho}\left[J_1(\kappa\rho)\right] \\ &= J_1(\kappa\rho) + \rho\left[\kappa J_0(\kappa\rho) - \frac{1}{\rho}J_1(\kappa\rho)\right] \\ &= \kappa\rho J_0(\kappa\rho) \end{aligned}$$

Then, it is derived that

$$H_z = \begin{cases} \dfrac{nI}{2l(r_o-r_i)}\displaystyle\int_0^\infty J_0(\kappa\rho)\chi\left(\kappa r_i,\kappa r_o\right)\frac{e^{-\kappa(z-s-l)}}{\kappa^2}\left(1-e^{-\kappa l}\right)d\kappa & z \ge s+l \\ \dfrac{nI}{2l(r_o-r_i)}\displaystyle\int_0^\infty J_0(\kappa\rho)\chi\left(\kappa r_i,\kappa r_o\right)\frac{1}{\kappa^2}\left(1-e^{-\kappa l}\right)d\kappa & s \le z < s+l \\ \dfrac{nI}{2l(r_o-r_i)}\displaystyle\int_0^\infty J_0(\kappa\rho)\chi\left(\kappa r_i,\kappa r_o\right)\frac{e^{-\kappa(s-z)}}{\kappa^2}\left(1-e^{-\kappa l}\right)d\kappa & z < s \end{cases} \tag{5.11}$$

After implementation of localized source from finite cross-section coil, we move to test our numerical codes based on the three-dimensional Stratton-Chu formulas. Firstly, we calculate the impedance change due to a half-space conductor that is truncated as a top surface

of conductive block B1 or B2 regarding to coil C5 or C27 testing. The numerical results are obtained based on the coil parameters in Table 5.1 and conductive block parameters in Table 5.2, and then compared to one experiment and two theoretical results, as shown in Table 5.3. The nominal edge size of mesh for coil C5 operated at 850 Hz is 3.21 mm, and that for coil C27 operated at 20 kHz is 2.14 mm. The numerical results agree with experimental and theoretical results well, and the slight difference comes from the half-plane truncation and mesh density.

Secondly, we calculate the impedance change in the case of a quarter-space. The experimental data for coil impedance variations in the presence of a conductive quarter consists of two measurement sets provided by Burke & Ibrahim [55] and the theoretical data provided by Bowler [54]. The first set is for coil C5 operated at 850 Hz and the second is for coil C27 operated at 20 kHz. As for the first set, the meshes generated for block B1 surface include total 6 facets and coil scan line moves right above the top facet, as demonstrated in Figure 5.10. Meanwhile, in order to reduce computation complexity and increase mesh density, we generate meshes for quarter-space surface of blocks represented by 2 facets, as also shown in Figure 5.10. Additionally, the block dimension is represented by a, b, and c as length, width, and depth, respectively. Impedance change measurements are recorded as a function of position with 2 mm intervals, while the coils moving across the edges of thick aluminum alloy blocks. In addition, the coil position referred in Figures 5.11-5.15 is the distance between the coil's axis position and the edge, and the value is zero if the coil center is directly above the edge. Resistance and reactance changes due to the block edge effect have been plotted in Figure 5.11, where curves have been made showing cubic or rectangular blocks with different edge sizes and mesh density. At the operating frequency of 850 Hz, the skin depth δ_1 is equal to 3.418

mm. With the nominal edge size approaching to the skin depth, the signal variation becomes larger. It is observed that signal variation from the edge of rectangular block (a=70 mm, b=70 mm, c=40 mm) is still a good approximation for the first measurement set at 850 Hz, since the truncation is beyond $10\delta_1$ from the coil position. To simplify the block geometry and achieve higher mesh density, we calculate the resistance and reactance changes due to quarter-space edge effect of rectangular block represented by 2 facets and compare the results with those of 6-facet rectangular block model, as shown in Figure 5.12. It is demonstrated that the 2-facet geometry model of the rectangular block is a good approximation for the total block surface, since the truncation of two quarter-space surface facets is large enough that the induced electric and magnetic currents on the other four facets are negligible. Then, comparison of resistance and reactance variation with coil axis position relative to the edge of the conductor B1 for coil C5 excited at 850 Hz has been shown in Figure 5.13, where numerical results are calculated using 2-facet quarter-space mesh with a truncation area (a=70 mm, b=70 mm, c=40 mm) and the nominal edge size of 2.85 mm. As for the second set, coil C27 is operated at 20 kHz and the skin depth δ_2 is equal to 0.762 mm. Similarly, 2-facet meshes for quarter-space surface of blocks haven been generated as geometry inputs to impedance change calculation. Resistance and reactance changes due to the block edge effect have been plotted in Figure 5.14, where curves have been made showing cubic or rectangular blocks with different edge sizes and mesh density. Then, numerical results of resistance and reactance variation of edge effect of the conductor B2 for coil C27 excited at 850 Hz have been compared with experimental and theoretical results, as shown in Figure 5.15, where numerical results are calculated using 2-facet quarter-space mesh with a truncation area (a=50 mm, b=50 mm, c=30 mm) and the nominal edge size of 1.90 mm. In general, the comparisons cover

cases where the skin depth is both small (0.762 mm at 20 kHz) and relatively large (3.418 mm at 850 Hz). The agreement between numerical results and those from theory and experiment is quite good in both cases, which demonstrates the capability that our numerical codes can simulate impedance change for arbitrary shape conductive objects interacted with coils in NDE applications.

Table 5.1. Coil parameters. [54]

parameter	Coil C5	Coil C27
r_i (mm)	9.33	7.04
r_o (mm)	18.04	12.4
s (mm)	3.32	3.43
l (mm)	10.05	5.04
n	1910	556

Table 5.2. Conductive block parameters. [54]

parameter	Block B1	Block B2
ρ ($\mu\Omega$ cm)	3.92	4.58
thickness (mm)	140	65

Table 5.3. Coil impedance change (Ω) due to half-space.

	Coil C5 at 850 Hz	Coil C27 at 20 kHz
Experiment	22.00 - j70.5	12.650 - j125.1
Dodd & Deeds [4]	22.20 - j70.49	12.801 - j125.288
Bowler [54]	22.25 - j70.45	12.801 - j125.329
Numerical result	22.095 – j70.012	12.705 – j124.380

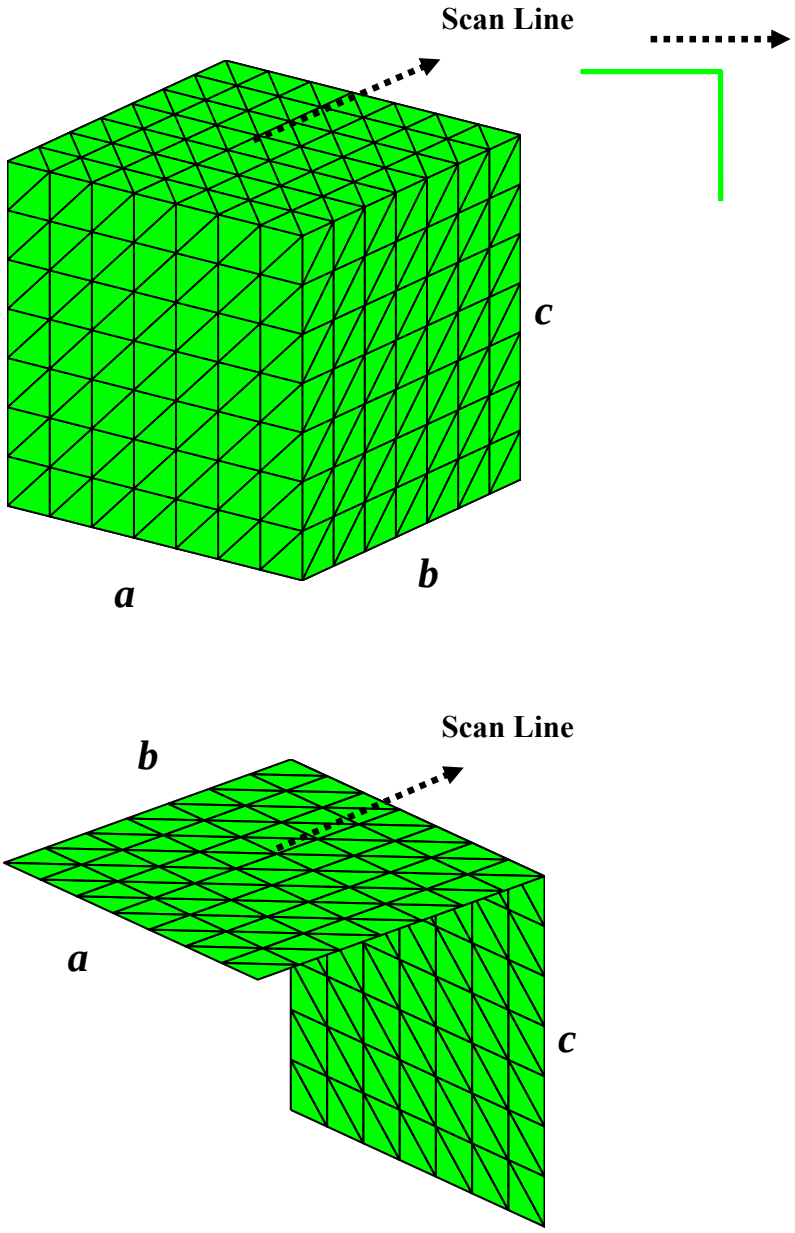

Figure 5.10. Illustration of block surface meshed by triangular patches and scanned by coil. Top: 6-facet mesh: Bottom: 2-facet mesh.

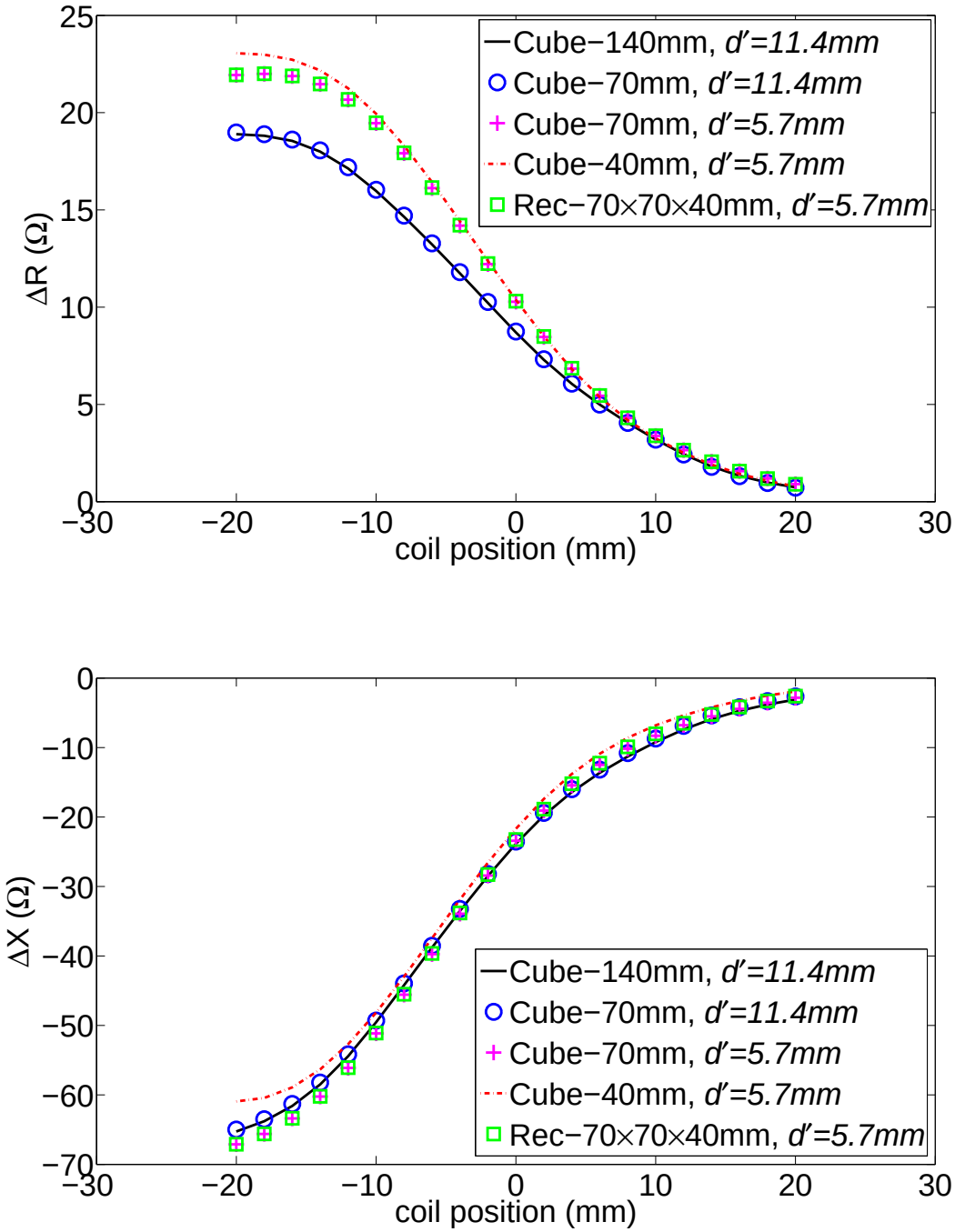

Figure 5.11. Comparison of numerical results of impedance change with coil axis position relative to the edge of the conductor B1 for coil C5 excited at 850 Hz using 6-facet meshes with different block sizes and mesh density, where *d'* is the nominal edge size of mesh. Top: resistance variation; Bottom: reactance variation.

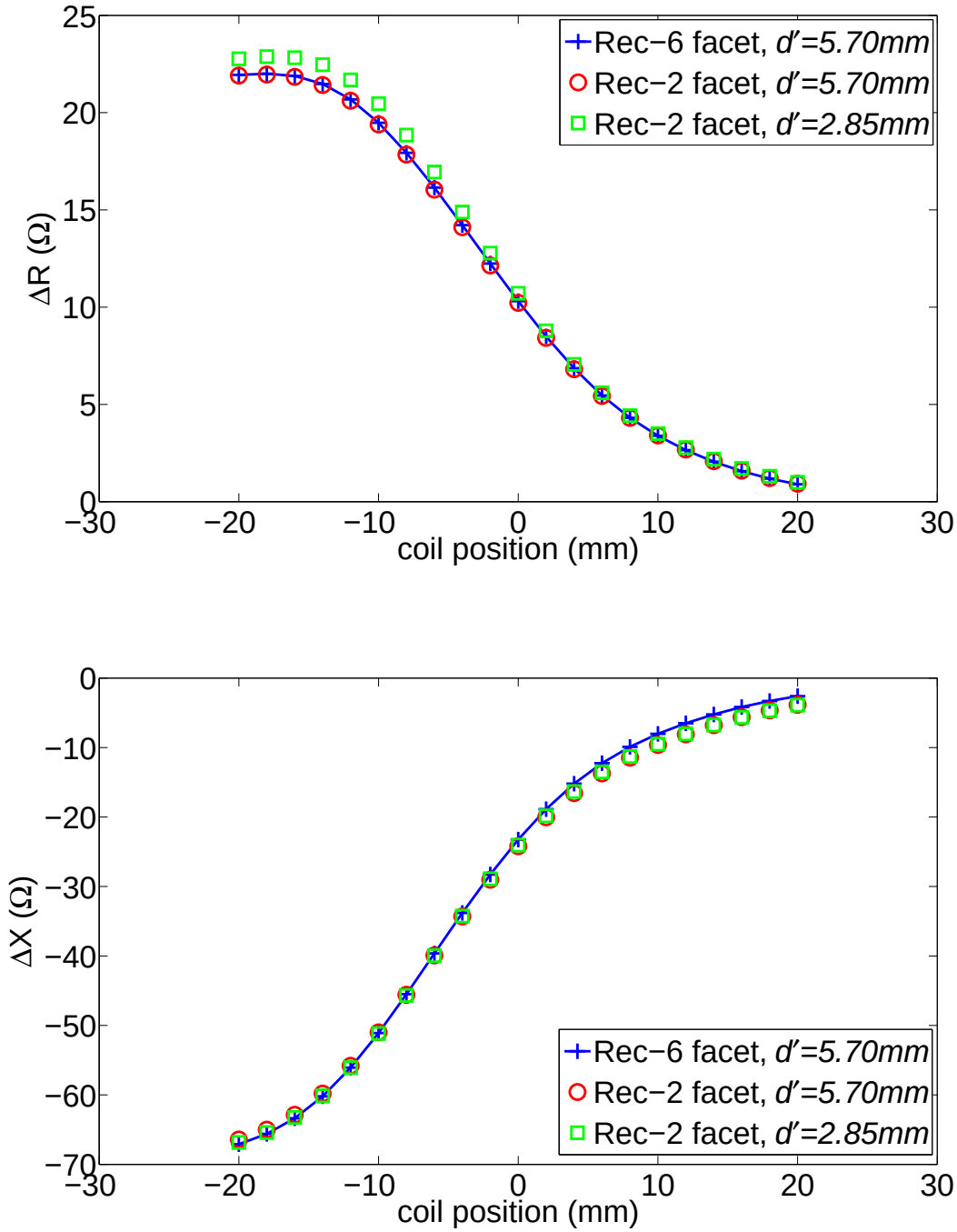

Figure 5.12. Comparison of numerical results of impedance change with coil axis position relative to the edge of the conductor B1 for coil C5 excited at 850 Hz using 6-facet and 2-facet meshes of a rectangular block (a=70 mm, b=70 mm, c=40 mm) with different mesh density, where d' is the nominal edge size of mesh. Top: resistance variation; Bottom: reactance variation.

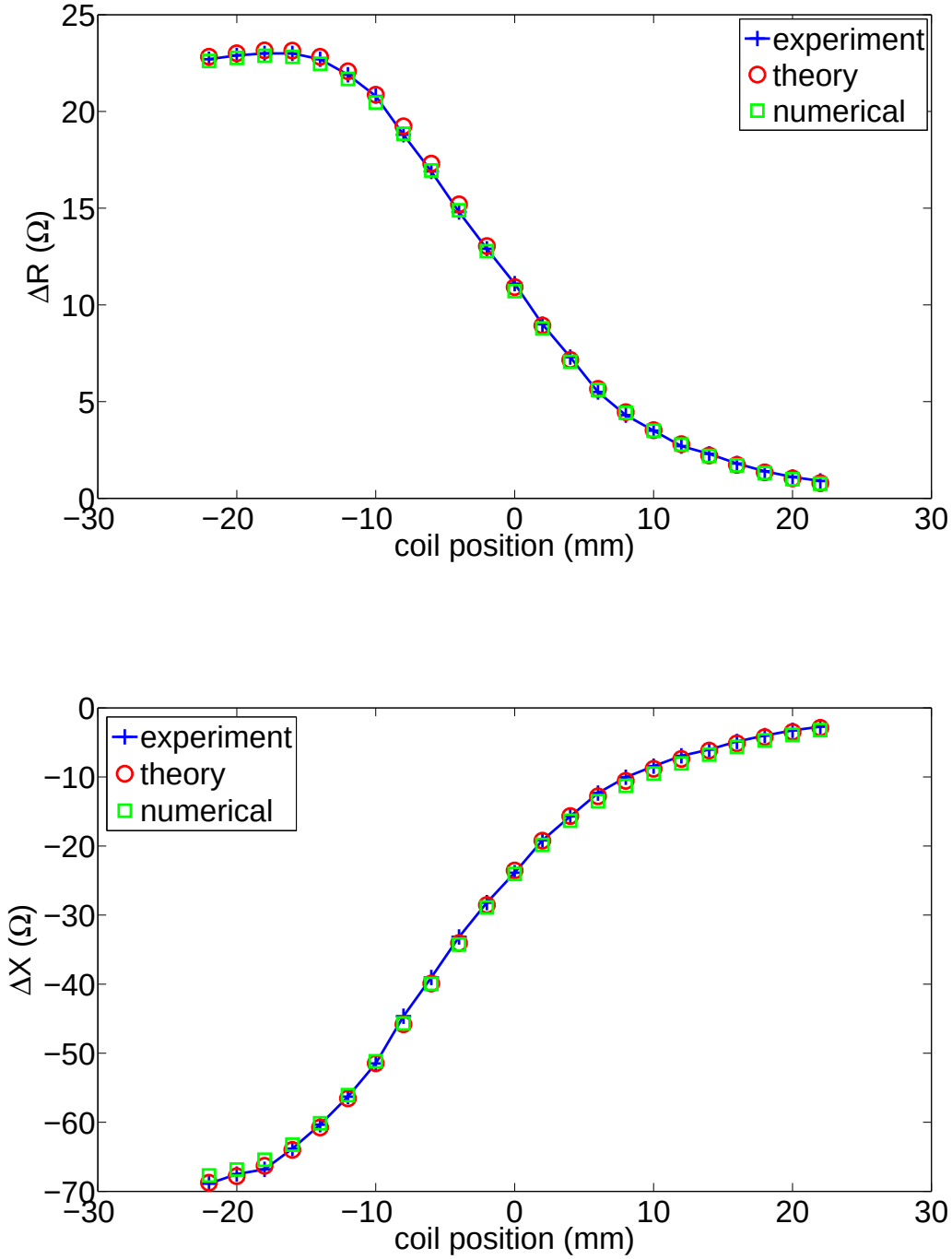

Figure 5.13. Comparison of impedance change with coil axis position relative to the edge of the conductor B1 for coil C5 excited at 850 Hz, where numerical results are calculated using 2-facet quarter-space mesh with a truncation area (a=70 mm, b=70 mm, c=40 mm) and the nominal edge size of 2.85 mm. Top: resistance variation; Bottom: reactance variation.

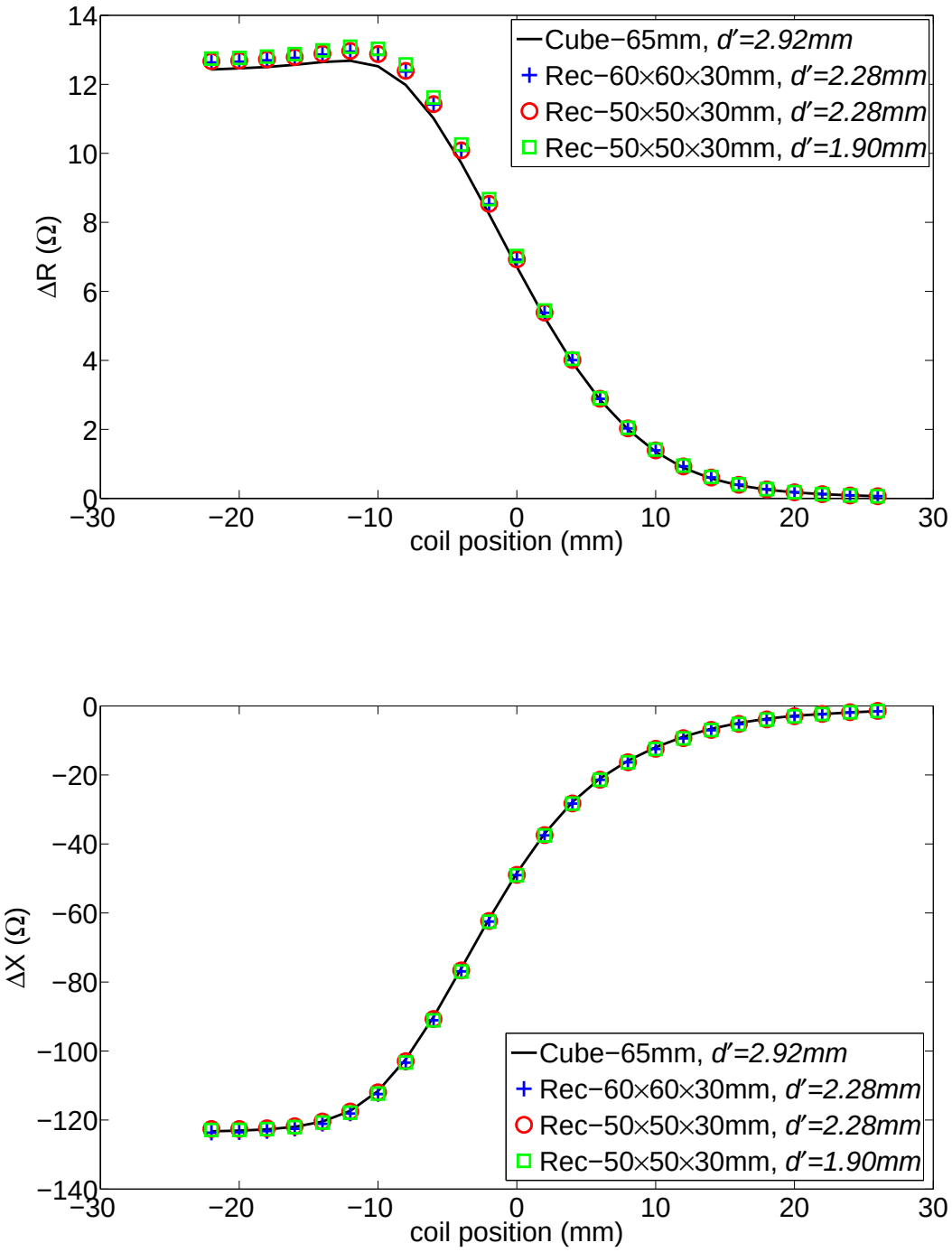

Figure 5.14. Comparison of impedance change with coil axis position relative to the edge of the conductor B2 for coil C27 excited at 20 kHz using 2-facet meshes with different block sizes and mesh density. Top: resistance variation; Bottom: reactance variation.

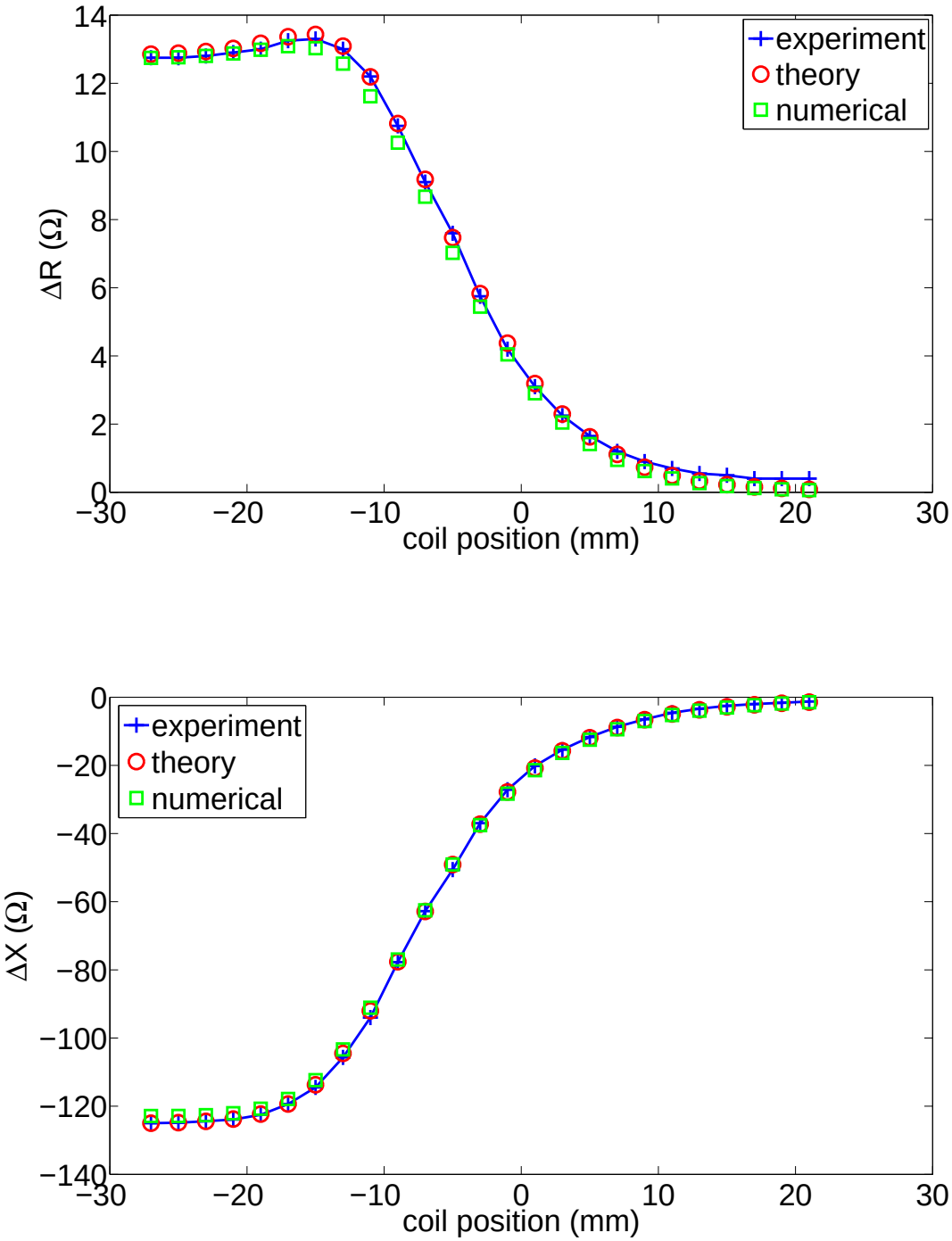

Figure 5.15. Comparison of impedance change with coil axis position relative to the edge of the conductor B2 for coil C27 excited at 20 kHz, where numerical results are calculated using 2-facet quarter-space mesh with a truncation area (a=50 mm, b=50 mm, c=30 mm) and the nominal edge size of 1.90 mm. Top: resistance variation; Bottom: reactance variation.

5.2.4 Coil above a Rectangular Slot in a Thick Plate

In this section, we calculate impedance change for a cylindrical coil due to a rectangular surface slot in a conductive thick plate, and the numerical results have been compared to the benchmark experimental measurements made by Burke [57]. The incident electric and magnetic fields from a coil with finite cross-section are calculated in the same way as that in the previous section.

After implementation of localized source from finite cross-section coil, we move to calculate the impedance change using our numerical codes based on the three-dimensional Stratton-Chu formulas. The two cases for the calculation of impedance change are the same test specimen interacted with two coils of operating frequencies at 900 Hz and 7 kHz, respectively, and the cases have the common feature of being based on practical eddy-current testing techniques, and of utilizing simple geometries. The experimental data for coil impedance variations consists of two measurement sets provided in [57], and the experimental arrangement is shown schematically in Figure 5.16. Here, a circular air-cored coil is scanned, parallel to the x-axis, along the length of a rectangular slot in an aluminum alloy plate. The first set is for a smaller coil A operated at 900 Hz and the second is for a larger coil B operated at 7 kHz. The resistance and reactance changes are measured as a function of coil-center position. The parameters of experiments, which include the coil parameters, the test specimen and the defect parameters, are listed in Table 5.4 and Table 5.5 for the two measurements respectively. The skin depth at 900 Hz is around 3.04 mm, while the skin depth at 7 kHz is reduced to 1.09 mm, which makes this problem differ from the first by nearing the thin-skin limit [58]. In the thin-skin regime, the skin depth is substantially smaller than the depth and length of the crack. It is estimated that accurate predictions can be made

with the restricted boundary conditions provided the crack depth and length are greater than approximately three skin depths.

To generate the geometry mesh, we truncate the top surface of the aluminum alloy plate into a square with a side of $2a_1 + 20\delta_i$ ($i = 1$ for the first set; $i = 2$ for the second set), as shown in Figure 5.17. Then, the truncation square and the within slot have been meshed into 3200 flat triangles and 4800 edges, and the nominal edge size of mesh in the first set is 2.25 mm and that in the second set is 1.65 mm. Meanwhile, the truncation square has also been meshed independently for calculating impedance change for the case that a cylindrical coil interacts with a conductive thick plate, as a reference to impedance variation due to the slot, which is similar to the impedance change calculation due to a half-space conductor in section 5.2.3. Moreover, impedance change measurements are recorded as a function of position with 0.5 mm interval in the first measurement set and 1 mm in the second, while the coils moving right above the rectangular slot in the thick aluminum alloy plane. In addition, the coil position referred to in Figures 5.18-5.19 is the distance between the coil's axis position and the center of the slot in x-axis, and the value is zero if the coil center is directly above the center of the slot. The comparisons cover cases where the skin depth is both small (1.09 mm at 7 kHz) and relatively large (3.04 mm at 900 Hz). As shown in Figures 5.18-5.19, reactance variations are dominant in impedance change in both measurements and the coil positions of the peak in the reactance variation curves provide an indication of the coil radius since the diameters of coil A and coil B are somewhat larger than the crack length of 12.60 mm. Specifically, at the coil position of zero, the coil axis passes through the center of the slot and, because the mean diameter of the coil is greater that the slot length, the eddy current circulates around the defect without interacting strongly. With the coil scanning through the slot, the

greatest interaction is observed when the coil is displaced from the center by roughly one mean coil radius. Moreover, the impedance change is symmetrical about coil position of zero, and a complete plot, including negative values of coil position, shows two peaks separated by a distance approximately equal to the mean coil diameter. The agreement between numerical results and those from experiment is fairly good in both cases, which provide more evidence that our numerical codes can practically simulate impedance change for arbitrary shape conductive objects with surface defects interacted with coils in NDE applications.

Table 5.4. Coil parameters. [58]

parameter	Coil A	Coil B
Inner radius a_2 (mm)	6.15	9.34
Outer radius a_1 (mm)	12.4	18.4
Lift-off l (mm)	0.88	2.03
Length b (mm)	6.15	9.0
Number of turns n	3790	408
Operating Frequency (Hz)	900	7000

Table 5.5. Test specimen parameters. [58]

parameter	Plate with a rectangular slot
Conductivity σ (S/m)	3.06×10^7
Thickness (mm)	12.22
Slot Length $2c$ (mm)	12.60
Slot Depth h (mm)	5.00
Slot Width w (mm)	0.28

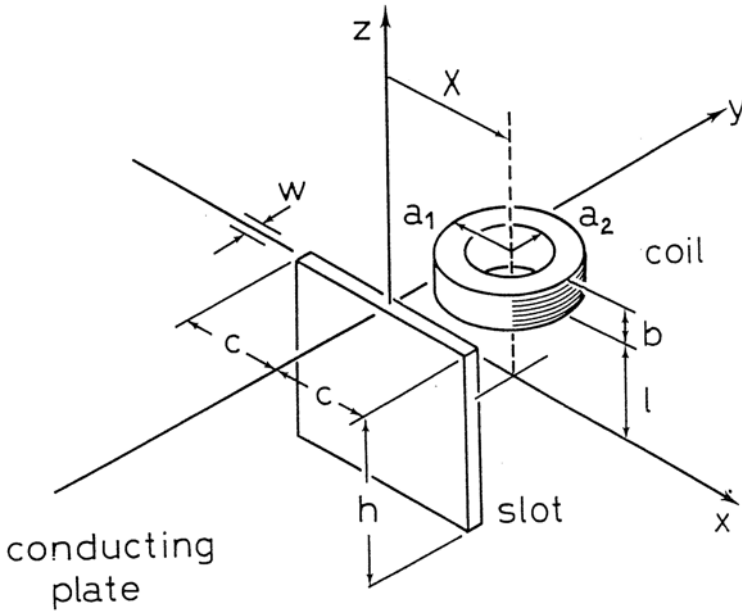

Figure 5.16. Schematic configuration for the measurement of impedance change due to a surface breaking slot [58].

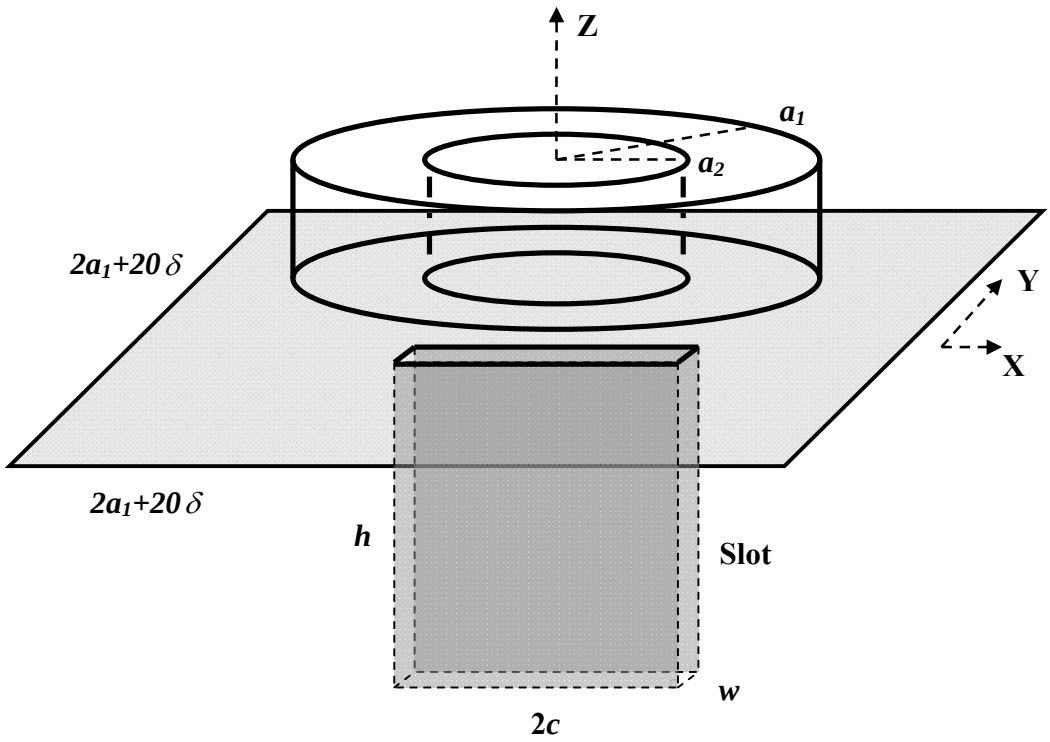

Figure 5.17. Geometry model of coil above a rectangular slot in a thick plate. The top surface of the plate is truncated into a square.

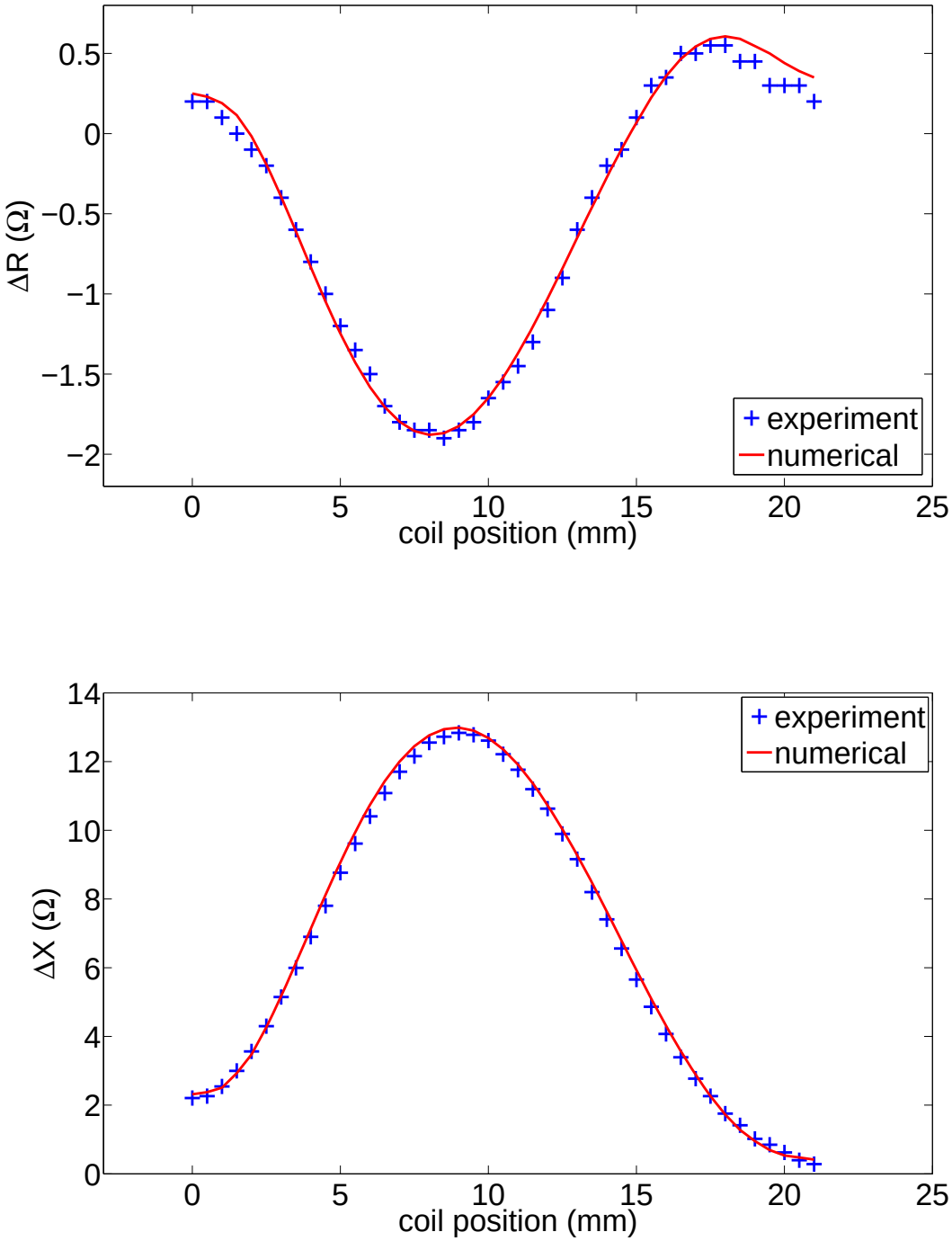

Figure 5.18. Comparison of impedance change with coil axis position relative to the center of the rectangular slot for coil A excited at 900 Hz. Top: resistance variation; Bottom: reactance variation.

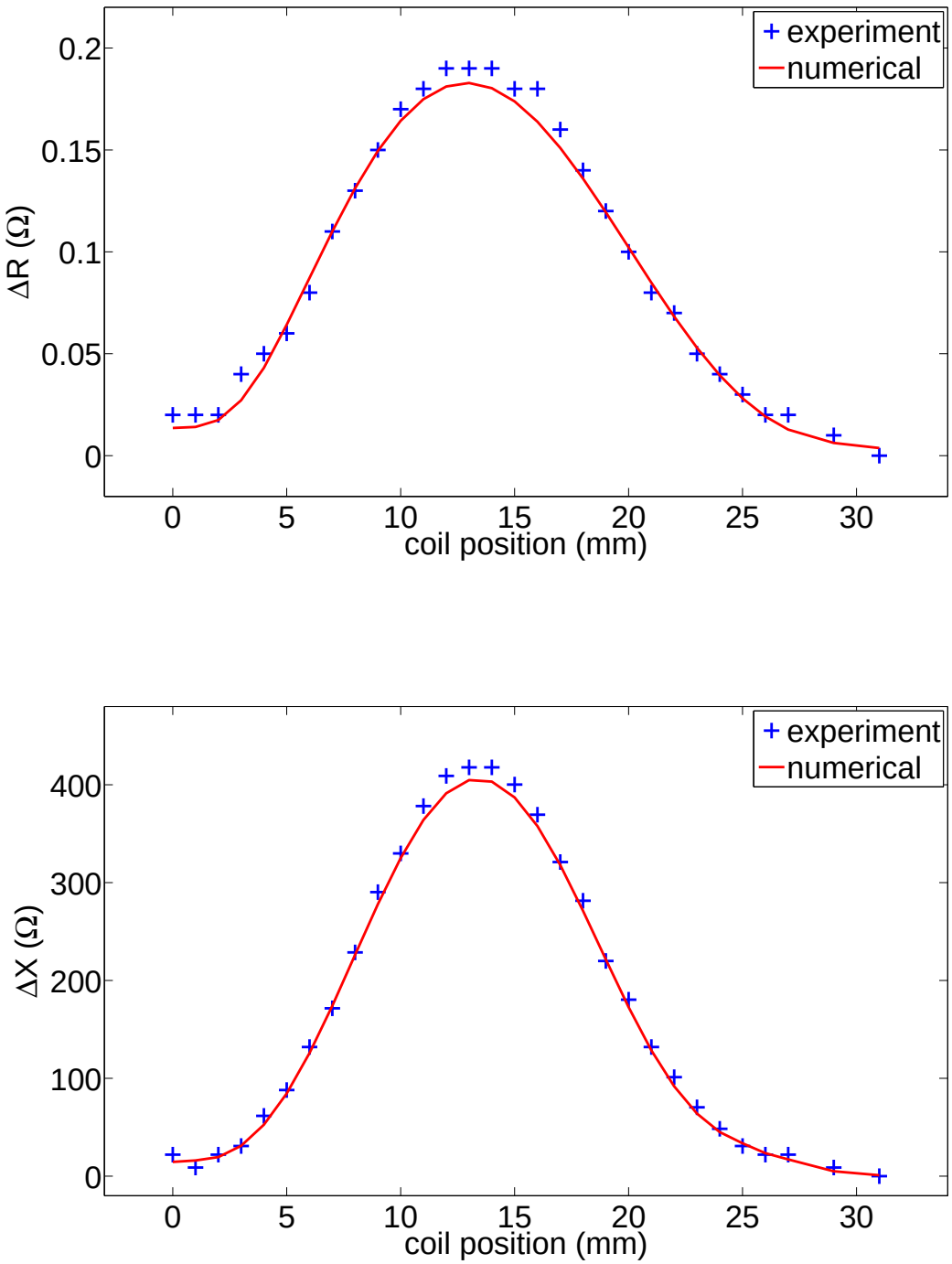

Figure 5.19. Comparison of impedance change with coil axis position relative to the center of the rectangular slot for coil B excited at 7 kHz. Top: resistance variation; Bottom: reactance variation.

CHAPTER 6. SUMMERY AND FUTURE WORK

In this dissertation, we introduce the FMM acceleration procedure of the BIE method, which is a promising technique, but yet to be applied to real-world three-dimensional eddy-current problems. As a prototype problem, we choose a two-dimensional Helmholtz equation with a complex wave number for a domain of a non-trivial boundary. We have verified explicitly that the conventional BIE method requires $O(N^2)$ operations to compute the system of equations and another $O(N^3)$ operations to solve the system using direct solvers or another $O(N^2)$ operations using iterative solvers, with N being the number of unknowns; in contrast, the BIE method accelerated by the two-level FMM can reduce the operations and memory requirement to $O(N^{3/2})$, while keeping the same order of accuracy.

Furthermore, we demonstrate a boundary integral equation method for modeling the eddy current inspection in three dimensions. The problem is formulated by the BIE and discretized into matrix equations by MoM or BEM. In the implementation of the Stratton-Chu formula for the conductive medium, the induced electric and magnetic surface currents are expanded in terms of RWG vector basis function, while the normal component of magnetic field is expanded in terms of the pulse basis function. Also, the low frequency approximation is applied in the external medium. Computational tests are presented to demonstrate the accuracy and capability of the three-dimensional BIE method with a complex wave number for both sphere and cube models described by a number of triangular patches for the simulation of eddy current inspection processes. The agreement between numerical results and those from theory and/or experiments is good in both cases of a single-turn coil above a sphere and a finite cross-section above a wedge or a rectangular slot in a thick plate,

which also give us confidence that our numerical codes can successfully simulate impedance change for arbitrary shape conductive objects interacted with coils in NDE application.

As for the follow-up work of this study, it is suggested that one would apply the BIE method to solve more practical eddy current NDE problems in three dimensions, such as adding dense crack mesh in the numerical model, etc. Also, it is worth continuing work on the three-dimensional BIE method accelerated by the FMM, which enhances the capability and adaptability of solving large-scale electromagnetic wave propagation and eddy-current problems.

BIBLIOGRAPHY

[1] H.L. Libby, *Introduction to Electromagnetic Nondestructive Test Methods*, Wiley, New York, NY (1971).

[2] B.A. Auld, *Eddy-Current Characterization of Materials and Structures*, ASTM STP 722, edited by G. Birnbaum and G. Free, Philadelphia, PA (1981).

[3] V.H. Rumsey, "Reaction concept in electromagnetic theory," *Phys. Rev.*, vol. **94**, pp. 1483-1491 (1954).

[4] C.V. Dodd and W.E. Deeds, "Analytical solutions to eddy-current probe-coil problems," *J. Appl. Phys.*, vol. **39**, pp. 2829-2838 (1968).

[5] R.E. Beissner and M.J. Sablik, "Theory of eddy currents induced by a non-symmetric coil above a conducting half-space," *J. Appl. Phys.*, vol. **56**, pp. 448-454 (1984).

[6] M. Burrows, *Ph.D. dissertation*, University of Michigan, University Microfilms, Ann Arbor, Michigan (1964).

[7] R. Palanisamy and W. Lord, "Finite element modeling of electromagnetic NDT phenomena," *IEEE Trans. Magn.,* vol. **15**, pp. 1479-1481 (1979).

[8] R.E. Beissner, "Boundary element model of eddy current flaw detection in three dimensions," *J. Appl. Phys.*, vol. **60**, pp. 352-356 (1986).

[9] H. Tsuboi and T. Misaki, "Three-Dimensional analysis of eddy current distributions by the boundary element method using vector variables," *IEEE Trans. Magn.,* vol. **23**, pp. 3044-3046 (1987).

[10] V. Rokhlin, "Rapid solution of integral equations of classical potential theory," *J. Comput. Phys.,* vol. **60**, no. 2, pp. 187-207 (1985).

[11] L. Greengard and V. Rokhlin, "A fast algorithm for particle simulations," *J. Comput. Phys.,* vol. **73**, pp. 325-348 (1987).

[12] J. Carrier, L. Greengard, and V. Rokhlin, "A fast adaptive multipole algorithm for particle simulations," *SIAM J. Sci. Stat. Comput.*, vol. **9**, pp. 669-686 (1988).

[13] J. Ambrosiano, L. Greengard, and V. Rokhlin, "The fast multipole method for gridless particle simulation," *Comput. Phys. Commun.*, vol. **48**, pp. 117-125 (1988).

[14] V. Rokhlin, "Rapid solution of integral equations of scattering theory in two dimensions," *J. Comput. Phys.,* vol. **86**, pp. 414-439 (1990).

[15] N. Engheta, W.D. Murphy, V. Rokhlin, and M.S. Vassiliou, "The fast multipole method (FMM) for electromagnetic scattering problems," *IEEE Trans. Antennas Propagat.*, vol. **40**, pp. 634-641 (1992).

[16] L.R. Hamilton, M.A. Stalzer, R.S. Turley, J.L. Visher, and S.M. Wandzura, "Scattering computation using the fast multipole method," *IEEE APS Int. Symp. Dig.*, Ann Arbor, MI, pp. 852-855 (1993).

[17] C.C. Lu and W.C. Chew, "Fast algorithm for solving hybrid integral equations," *Proc. Inst. Elect. Eng.*, vol. **140**, pt. H, no. 6, pp. 455-460 (1993).

[18] R. Coifman, V. Rokhlin, and S. Wandzura, "The fast multipole method for the wave equation: A pedestrian prescription," *IEEE Antennas Propagat. Mag.,* vol. **35**, no. 3, pp. 7-12 (1993).

[19] R.L. Wagner and W.C. Chew, "A ray-propagation fast multipole algorithm," *Microwave Opt. Technol. Lett.*, vol. **7**, no. 10, pp. 435-438 (1994).

[20] J.M. Song and W.C. Chew, "Fast multipole method solution using parametric geometry," *Microwave Opt. Technol. Lett.*, vol. **7**, no. 16, pp. 760-765 (1994).

[21] J.M. Song and W.C. Chew, "Multilevel fast multipole algorithm for combined field integral equation of electromagnetic scattering," *Microwave Opt. Technol. Lett.*, vol. **10**, no. 1, pp. 14-19 (1995).

[22] J.M. Song, C.C. Lu, and W.C. Chew, "MLFMA for electromagnetic scattering by large complex objects," *IEEE Trans. Antennas Propagat.*, vol.**45**, no.10, pp. 1488-1493 (1997).

[23] W.C. Chew, J. Jin, E. Michielssen, and J. Song, Eds., *Fast and Efficient Algorithms in Computational Electromagnetics,* Artech House, Norwood, MA (2001).

[24] E. Darve, "The fast multipole method: numerical implementation," *J. Comput. Phys.,* vol. **160**, pp. 195-240 (2000).

[25] N. Nishimura, "Fast multipole accelerated boundary integral equation methods," *Appl. Mech. Rev.,* vol. **55**, no. 4, pp. 299-324 (2002).

[26] G. Rubinacci, A. Tamburrino, S. Ventre, and F. Villone, "A fast 3-D multipole method for eddy-current computation," *IEEE Trans. Magn.,* vol. **40**, no. 2, pp. 1290-1293 (2004).

[27] R.F. Harrington, *Field Computation by Moment Methods,* Macmillan, New York (1965).

[28] J.A. Stratton, *Electromagnetic Theory*, McGraw-Hill, New York, NY (1941).

[29] S.M. Rao, D.R. Wilton, and A.W. Glisson, "Electromagnetic scattering by surfaces of arbitrary shape," *IEEE Trans. Antennas Propagat.*, vol **30**, pp. 409-418 (1982).

[30] E.L. Fredholm, "Sur une classe d'equations fonctionnelles," *Acta Mathematic*, vol. **27,** pp. 365-390 (1903).

[31] C. Müller, *Foundations of the Mathematical Theory of Electromagnetic Waves,* Springer-Verlag, Berlin (1969).

[32] R.F. Harrington, "Boundary integral formulations for homogeneous materials bodies," *J. Electromagnetic Waves and Applications*, vol. **3**, no. 1, pp. 1-15 (1989).

[33] A.J. Poggio and E.K. Miller, "Integral equation solutions of three-dimensional scattering problem," Chapter 4 of R. Mittra (ed.) *Computer Techniques for Electromagnetics*, Pergamon Press, Oxford (1973).

[34] Y. Chang and R.F. Harrington, "A Surface formulation for characteristic modes of material bodies," *IEEE Trans. Antennas Propagat.*, vol. **27**, pp. 785-789 (1977).

[35] T.K. Wu and L.L. Tsai, "Scattering from arbitrarily-shaped lossy dielectric bodies of revolution," *Radio Science*, vol. **12**, pp. 709-718 (1977).

[36] J.R. Mautz and R.F. Harrington, "Electromagnetic scattering from a homogenous body of revolution," *A.E.U.*, vol. **33**, pp. 71-80 (1979).

[37] G.C. Hsiao and R.E. Kleinman, "Mathematical foundations for error estimation in numerical solution of integral equations in electromagnetics," *IEEE Trans. Antennas Propagat.*, vol. **45**, no. 3, pp. 316-328 (1997).

[38] T.W. Lloyd, J.M. Song, and M. Yang, "Numerical study of surface integral formulations for low-contrast objects," *IEEE Antennas Wireless Propagation Lett.,* vol. **4**, pp. 482-485 (2005).

[39] A.W. Glisson and D.R. Wilton, "Simple and efficient numerical methods for problems of electromagnetic radiation and scattering from surfaces," *IEEE Trans. Antennas Propagat.*, vol. **28**, no.5, pp. 593-603 (1980).

[40] K.F. Warnick and W.C. Chew, "Error Analysis of the Moment Method," *IEEE Antennas Propagat. Mag.*, vol. **46**, no. 6, pp. 38-53 (2004).

[41] M. Yang and J. M. Song, "Error in projection of plane waves using the RWG basis functions," *IEEE AP-S International Symposium*, Albuquerque, NM, pp. 2873-2876, (2006).

[42] F.G. Hu, J.M. Song, and M. Yang, "Error in projection of plane waves using various basis functions," *IEEE Antennas Propagat. Mag.*, vol. **51**, no. 2, pp. 86-98, (2009).

[43] G.S. Warren and W.R. Scott, "Numerical dispersion of higher order nodal elements in the finite element method," *IEEE Trans. Antennas Propagat.*, vol. **44**, no. 3, pp. 317-320 (1996).

[44] M. Yang, Z. Chen, N. Nakagawa, and J. M. Song, "A fast multipole boundary integral equation method for two-dimensional diffusion problems," *Review of Progress in Quantitative NDE*, Portland, OR, Proceedings vol. **26**, pp. 294-301 (2006).

[45] M. Yang, J.M. Song, and N. Nakagawa, "Fast multipole solutions for diffusive scalar problems," *Review of Progress in Quantitative NDE*, Golden, CO, Proceedings vol. **27A**, pp. 305-312 (2007).

[46] N. Nakagawa, "A weakly singular formulation of boundary integral equations and field computation near boundaries," *J. Comput. Phys.,* vol. **122**, pp. 143-149 (1995).

[47] C.A. Balanis, *Advanced Engineering Electromagnetics,* John Wiley and Sons, Hoboken, NJ (1989).

[48] R.D. Graglia, "On the numerical integration of the linear shape functions times the 3-D Green's function or its gradient on a plane triangle," *IEEE Trans. Antennas Propagat.*, vol. **41**, no. 10, pp. 1448-1455 (1993).

[49] M. Yang, J.M. Song, and N. Nakagawa, "Solution of boundary integral equations for eddy current flaw detection in three dimensions," *Review of Progress in Quantitative NDE*, Chicago, IL, Proceedings vol. **28**, pp. 303-310 (2008).

[50] R.F. Harrington, *Time Harmonic Electromagnetic Fields*, McGraw-Hill, New York, NY (1961).

[51] B.A. Auld and J.C Moulder, "Review of advances in quantitative eddy current nondestructive evaluation," *J. Nondestructive Evaluation,* vol. **18**, no. 1 pp. 3-36 (1999).

[52] M.Y. Antimirov, A.A. Kolyshkin, and R. Vaillancourt, *Mathematical Models for Eddy Current Testing*, Les, Canada (1997).

[53] N. Bowler and J.R. Bowler, *Eddy Current Nondestructive Evaluation*, EE 558X Class Notes, Ames, IA (2007).

[54] T.P. Theodoulidis and J.R. Bowler, "Eddy current coil interaction with a right-angled conductive wedge," *Proc. Roy. Soc. Ser A*, vol. **461**, pp. 3123-3139 (2005).

[55] S.K. Burke and M. Ibrahim, *3D edge effect in eddy-current NDE: experimental data for a cylindrical air-cored coil and an Al alloy quarter space*, DSTO, Melbourne (2004).

[56] I.S. Gradshteyn and I.M. Ryzhik, *Tables of integrals, series and products, 5th ed.*, Academic Press, New York (1980).

[57] S.K. Burke, "A benchmark problem for computation of ΔZ in eddy-current nondestructive evaluation (NDE)," *J. Nondestructive Evaluation,* vol. **7**, pp. 35-41 (1988).

[58] H. Harfield and J.R. Bowler, "Theory of thin-skin eddy-current interaction with surface cracks," *J. Appl. Phys.*, vol. **82**, pp. 4590-4603 (1997).

ACKNOWLEDGEMENTS

I would like to express my gratitude to those who helped me with various aspects of conducting research and the writing of this dissertation.

First of all, I would like to thank my major professor, Dr. Jiming Song and my committee member, Dr. Norio Nakagawa, for their guidance, patience, and support throughout my Ph.D. study. Their instructions, insights, and motivation always help me to proceed to the destiny. I have learned so much from their preciseness in every detail of academic research.

I would also like to thank my other committee members for their valuable comments and suggestions to my research work: Dr. William Q. Meeker, Dr. John R. Bowler, Dr. Mani Mina, and Dr. Ronald A. Roberts. In addition, I would like to thank Dr. John R. Bowler for providing his data in this dissertation.

Finally, I sincerely thank my parents and my wife, who have supported me all these years. Their unconditional love and warm encouragement have often renewed my hopes for the future. Moreover, I would like to thank all my friends for their care and help in my life at Iowa State University.